INTEGRATING DETECTORS AND THEIR APPLICATION TO INFRARED ASTRONOMY

Mark Christopher Bird

Presented for the Degree of Doctor of Philosophy

University of Edinburgh

April 1988

This thesis has been composed by
myself and consists entirely of
my own work, except where noted
in the text.

April 1988

TABLE OF CONTENTS

Acknowledgements

Firstly, special thanks to Gordon Adam for his assistance in the laboratory with the electronics and the long-fought struggle to reduce the detector noise.

For their help and comments during the array testing phase, I would like to thank Tim Chuter, John Harris, Ian Sheffield and Dr Malcolm Stewart.

Frank Holmes gave an interesting and very useful course in the workshop (especially on the merits of chucks left in rapidly rotating drills), for which I am grateful. I also thank the workshop staff for their assistance.

During the course of my work I had useful discussions with Dr Tom Geballe, Dr Matt Mountain, Dr Alan Tokunaga and my supervisor, Dr Richard Wade.

I acknowledge my fellow students, and in particular thank Crispin Keable, Mark McCaughrean and Alan Moorhouse for their help.

Liz Gibson provided a welcome diversion from the monotony of work, as well as unlimited access to the treats of a well-stocked stationary cupboard.

Finally, I would especially like to thank my office-companion over the three years, John Rayner, for injecting a much-appreciated sense of humour into the proceedings.

Abstract

The work contained in this thesis is concerned with the performance of infrared integrating detector arrays, within the context of astronomical spectroscopy.

A linear array of thirty-two InSb photodiodes is investigated. It is found to exhibit good capacitance and dark current uniformity across the array. By applying the principle of charge conservation to the multiplexed readout arrangement of this device, the signal response of the detector to different levels of illumination is derived. It is found from this, and confirmed experimentally, that the device has a highly linear radiation response over a range of reverse biases.

The interaction between dark current and photo-current is studied, primarily by the application of a simple model. The results indicate that the effective signal gain of a detector can vary in the situation where dark current dominates the discharge processes, since in this instance accurate dark current subtraction becomes difficult.

The predictions of the model are compared with experiments performed on two integrating arrays; one under study in the laboratory, and the other installed in the low background environment of a cooled grating spectrometer. Finally, suggestions are presented of ways of avoiding this problem, the simplest of which involves utilizing, where possible, low dark current detector materials.

The importance of achieving good dark current uniformity with arrays is stressed, since this will improve the ability to flat-field faint object spectra.

To illustrate the importance of these devices, infrared spectra obtained with array detectors, covering a range of astronomical objects, are presented and discussed.

CHAPTER ONE

INTRODUCTION AND AIM OF PRESENT WORK

The first two-dimensional silicon Charge Coupled Devices (CCDs) were built in the early 1970's, and quickly found applications in optical astronomy. Over the last few years there have been rapid developments in similar detector arrays for the infrared region, and we are now at the stage where these arrays are being introduced in instruments on ground-based telescopes.

Detector arrays, containing large numbers of light-sensitive elements, are designed to record the distribution of incident light and store it at the detector for a programmeable integration (or stare) time, and for this reason are commonly referred to as integrating arrays. It is this property which potentially allows very high sensitivities to be achieved.

At the Royal Observatory of Edinburgh (ROE), interest in these arrays has evolved from experience gained working with single element detectors in the infrared, used mainly in photometers, and CCDs used in visible cameras, to the stage where an infrared camera, built around a 58x62 InSb array, was recently commissioned for use on the United Kingdom Infrared Telescope (UKIRT).

Currently there is a project in progress to design and construct a 1-5 micron grating spectrometer (CGS4) which will include arrays such as the one above, as well as devices becoming available ie. a 128x128 HgCdTe array with a wavelength cut-off of 2.5 microns. The spectrometer will operate in a 'long-slit' mode, where the wavelength is dispersed in one dimension and field of view along the slit in the other. The wavelength resolution, $\lambda/\Delta\lambda$ will be in the range ~500 to a few $x10^4$.

The work presented here arose from the need to understand the behaviour of infrared arrays and how they could best perform in a spectroscopic environment, given that such parameters as the

temperature, bias, stare time and optical configuration, etc., can be controlled at the detector.

The subject of integrating detectors is reviewed in chapter two, which describes several forms of these devices and considers the important aspects of their operation.

The major part of the work (chapters three to six) involved studying a linear infrared array, in the hope of deriving results which could be applied to integrating arrays in general, concerning such aspects as the response linearity, noise behaviour and dark current processes.

In particular, since a spectrometer will be exposed to a range of background flux levels, the interaction between detected illumination and internally generated dark current was studied. The aim being to discover the array conditions which would allow reliable flux calibration.

Finally, since the emphasis was on detector applications within spectroscopy, the final chapter presents the results of some observations made with arrays, in order to give a taste of the broad subject of infrared astronomical spectroscopy.

CHAPTER TWO

INTEGRATING DETECTORS

Introduction

This chapter provides a brief review of semiconductor detectors for the infrared (IR) region, concentrating on a class of detectors which are beginning to find applications in astronomy; integrating detectors.

Broadly, this semiconductor device works by converting incident radiation into mobile charges, which are subsequently stored, at or close to, the detector, either in a potential well or across the plates of a capacitor.

The advantage of integrating detectors is that, once initialized, they can then be isolated for an integration period, after which time a signal voltage is measured. This, in principle, allows a large number of detectors to be arranged in one or two dimensional arrays. Various readout schemes enable the detectors to be densely packed (thus minimizing the area, or dead space, not responsive to radiation), and multiplexed onto a single output line, so that the output from each detector is processed in the same circuit.

Before describing the operation of these devices, it is useful to consider what properties are desirable for astronomical applications. Infrared astronomy generally involves observing faint sources against large background fluxes, so that the signal contrast is low. This is certainly true for wavelengths greater than 2.5 microns, where radiation from the telescope tends to dominate. Also, at some wavelengths the background spectrum is highly structured and may be prone to spatial and temporal fluctuations, so that it is necessary to chop between the source and sky. In cases where chopping is not necessary, accurate background subtraction is still required. Bearing these considerations in

mind, the following factors are of importance;

(i) Detector sensitivity. In integrating detectors this will depend on the minimum readout noise, which may be a function of the detector capacitance, its temperature, or possibly the noise of the preamplifier. If the dominant noise source is the shot-noise of the background (in which case the detector's performance is background limited, referred to as Background Limited Infrared Performance or BLIP), then it is the detector responsivity, as well as the background level itself, which determines the sensitivity. The sensitivity is normally represented by the noise equivalent power (NEP), which is the incident radiant power required to give an output voltage signal to noise ratio of unity. The noise, which will be frequency dependent, is represented by the rms noise voltage and is normalized to unit bandwidth. The units of NEP are $WHz^{-1/2}$. For a traditional detector the noise bandwidth would be determined by the frequency response of the external circuit. Where the signal is integrated for a time t_i, the electrical bandwidth is given by $\Delta f=1/2t_i$ (Boyd,1983).

(ii) Detector efficiency. This quantity is normally described in terms of the quantum efficiency, qe; the proportion of incident photons producing a detectable event, such as an electron-hole pair. A high value of qe, in combination with a high throughput instrument are essential for achieving high sensitivity on the sky.

An alternative way of representing efficiency is by the responsivity, R, which is the ratio of output signal (voltage or current) to input power, and is useful for direct comparison of signal levels with noise voltages. The current responsivity is

$$R = I_s/P_{in} = (q\lambda/hc).\ (qe.G)$$

$q = 1.602\times10^{-19}$ Coulombs

G is the photoconductive gain (the number of charges passing through the detector per photogenerated charge).

(iii) Dynamic range (ratio of maximimum and minimum signals present). This is a particularly important aspect of integrating detectors, since in order to accumulate enough signal charges to achieve BLIP, the ratio of storage capacity to the readout noise should be maximized. This ratio represents the potential dynamic range (a measure of information content), which, in practice, will be reduced by shot-noise and excess noise in the detector. Once maximized, however, it will enable a large proportion of the pixels to be background noise limited, when there is a brightness distribution across the array.

The storage capacity is also important since it will influence the largest background flux which can be observed, given constraints on the readout rate.

(iv) Stability. In situations where the background is low, the sensitivity can be improved by increasing the 'on-chip' integration time, t_i, until BLIP is reached, and the maximum t_i will depend on either the stability of the background itself or that of the detector and its associated electronics. Integrations lasting several minutes are feasible (optical CCDs often integrate charge for periods of ten minutes or more). Temperature stability of the array is desirable in order to minimize dark current and gain variations.

(v) Response linearity. If there is not a linear relation between input flux and output signal, and this effect is not properly calibrated, noise may be added to the derived signal.

(vi) Detector uniformity. Offset and gain variations across the detector array are a problem in imaging and spectroscopic applications, since the intrinsic spectral and brightness distribution of an object is altered. In order to make each detector's response identical, a uniform brightness input (flat-field) is required, which can be used to correct detector differences. This process is not perfect, so that more noise may be added to the signal. Also, non-linear responses may complicate the

issue. The errors introduced will be smaller for a more uniform array, which also has the advantage that a meaningful output can be observed at the same time that the observations are being made.

Semiconductor detectors, as opposed to thermal and photoemissive detectors, have been developed because they offer high quantum efficiency, the potential for high sensitivity, and can be constructed in units containing high densities of detector elements.

The rest of this chapter will review a range of integrating devices, dealing with such aspects as the detection process, dark current behaviour, readout mechanisms and associated sources of noise. The discusion will be restricted to those devices which are now being applied to, or are likely to find future applications in, infrared astronomy.

2.1 The Photoconductor

PbSe (1-6μm) and PbS (1-3μm) photoconductors were amongst the first semiconductors used in infrared astronomy, with longer wavelengths covered by the Ge:Ga (gallium doped germanium) bolometer.

The photoconductor represents the simplest form of semiconductor detector. An incident photon is absorbed, producing a mobile charge which increases the conductivity of the sample. If a constant bias is applied, the current variation can be monitored as a voltage change across a load resistor in series with the detector.

In a pure (intrinsic) semiconductor, the absorbed photon must have enough energy to excite an electron to the conduction band. This leads to two mobile carriers (the electron, and a hole in the valence band), which are oppositely charged, move in opposite directions under the influence of an external electric field, and therefore both add to the net current. The long wavelength cut-off is given by

$$\lambda_c = hc / E_g = 1.24 / E_g(eV) \quad \text{microns}$$

where E_g is the bandgap energy. The short wavelength response is

usually determined by the absorption properties of the semiconductor or layers deposited on it, such as anti-reflection coatings and metal contacts.

The detector becomes extrinsic when impurities are introduced. The impurity atoms lie at energies within the bandgap and can be ionized by photons to supply electrons to the conduction band (donors) or holes to the valence band (acceptors). This method is used to increase λ_c. Since the doping concentration is not as large as that of the intrinsic semiconductor, the absorption coefficient is smaller, leading to lower qe's.

Table 2.1 presents the properties of a selection of semiconductors used in the optical and infrared region (responsivity curves for some of these materials can be found in Wolf, 1985, Sclar, 1983 and The Infrared Handbook, 1978, Wolfe and Zissis, Office of Naval Research).

For an intrinsic detector, where either the electron or hole mobility dominates, and for an extrinsic detector with only one current carrier, it is easy to derive the radiation response. If the illumination level is $\Phi(\lambda)$ photons per second, then the steady state number of charges generated is $N=\Phi(\lambda).qe(\lambda).\tau$, where τ is the carrier lifetime before recombination. The current will depend on the time taken for charges to cross the sample, t (the ratio of length between ohmic contacts, L, and drift velocity, v, which depends on the applied bias, V);

$$I = qN/t = q.\Phi(\lambda).qe(\lambda).(\tau/t) = q.\Phi(\lambda).qe(\lambda).(\tau\mu V/L^2)$$

μ is the carrier mobility.

$G=\tau/t$ is the photoconductive gain, and is the number of charges passing through the sample per detected photon. G can be greater than one, since, if the recombination time is sufficiently large, an electron will pass through the sample and be replaced by another entering at the negative terminal. This will continue until the electron recombines. G cannot be increased indefinitely by ramping up the bias, since scattering processes eventually cause it to level off.

Table 2.1 Semiconductor Properties

(a) Intrinsic

	Direct/ Indirect	E_g (T) eV (K)	λ_c μm	ϵ
Si	I	1.12 (300)	1.1	11.8
Ge	I	0.66 (300)	1.9	16
PbS	I	0.41 (300)	3.0	17
PbSe		0.23 (195)	5.4	
InAs	D	0.41 (77)	3.0	14.5
InSb	D	0.22 (77)	5.6	17
$Hg_{0.8}Cd_{0.2}Te$	D	0.09 (77)	13.8	18
$Hg_{0.6}Cd_{0.4}Te$	D	0.49 (120)	2.5	15
$Pb_{0.2}Sn_{0.8}Te$	D	0.1	12.4	

(b) Extrinsic

S-c: Impurity	Donor/ Acceptor	Ioniz. Energy ΔE_{th} (eV)	λ_c (T) μm (K)	Range μm
Ge:Be	A	0.03	50	30-50
Ge:Ga	A	0.01	120	50-120
Si:In	A	0.15	7.4 (78)	3-7
Si:Bi	D	0.07	18.7 (29)	10-18.5
Si:As	D	0.05	24 (5)	16-25
Si:Sb	D	0.04	31 (5)	18-30

A photoconductor's sensitivity is limited by the shot-noise of the detected radiation, and noise due to the random fluctuation of carrier densities, known as generation-recombination noise (Boyd, 1983). In photovoltaic detectors, where oppositely charged carriers are separated, g-r noise reduces to dark current shot-noise and is smaller by a factor of $\sqrt{2}$.

To maximize the signal voltage, the load resistance should be much greater than that of the detector, but this is at odds with maintaining a constant bias (so that G is constant, and the response is linear over a large flux range), which is achieved when the load resistance is small.

This conflict between gain and linearity, as well as the presence of g-r noise and the necessity of applying a constant bias has meant that photoconductors have not been used as extensively as photovoltaics for integrating applications.

However, a number of arrays have been constructed, using extrinsic materials which are of high impedance (like photovoltaics) and can therefore be matched to high impedance readout elements, such as JFETs.

A 32x32 Si:In array (2-8μm) connected directly to a CCD readout has been incorporated into a camera (Tollestrup, 1985) and used to obtain a 3.5μm mosaic image of the Galactic Centre. The dynamic range was reported to be typically 4000, with an average G.qe product of 35% at an operating temperature of 30K. This experimental array seems to exhibit excess noise, possibly associated with the input connections to the CCD structure.

SBRC (Santa Barbara Research Corp.) have developed a 58x62 Si:Sb array, λ_c=29μm, employing direct readout (Goebel, 1986a), for long wavelength applications on SIRTF (Space Infrared Telescope Facility). The pixel dimensions are 76x76μm with nearly 100% of the front area optically active. At low operating temperatures (7K), G.qe is approximately 20%.

2.2 The Photovoltaic Detector

The photovoltaic (PV) detector, which in contrast to the photoconductor, operates by separating charges in an internal electric field, has been widely used in astronomy.

2.2.1 Diode Geometry

The p-n junction photodiode, the most common PV device, is formed by joining a semiconductor doped with donor impurities (where the ionization energy is so low that, for a donor concentration, N_d, N_d electrons are contributed to the conduction band), to a piece of the same material doped with acceptors. The two samples are referred to as n- and p-type. Generally the doping concentrations, N_d and N_a ($\gtrsim 10^{15}cm^{-3}$), dominate the intrinsic carrier concentration, n_i, which for InSb at 77K is $3x10^{9}cm^{-3}$.

(n_i is the density of free carriers, and is independent of the doping level. In an intrinsic sample $n_i=n=p$, where n and p are the free electron and hole densities, and for an extrinsic sample, where obviously $n \neq p$, $np=n_i^2$ holds (Yang, 1978). Thus, for an n-type sample, $n \approx N_d$ and $p \approx n_i^2/N_d$.)

The processes occurring when the n- and p-type materials are brought into contact are illustrated in figure 2.1, and described below.

For an intrinsic semiconductor, the Fermi level, or energy of a state for which the occupation probability is one half, lies in the middle of the bandgap (this is only strictly true if the density of states on either side of the bandgap are identical, but is a good approximation). At absolute zero, there are no free carriers. As the temperature is raised electrons are excited to the conduction band leaving equal numbers of holes in the valence band.

For a doped sample (ie. donors) at absolute zero, the Fermi level lies between the donor level and the conduction band. As the temperature is raised the donors become ionized and n becomes much greater than p.

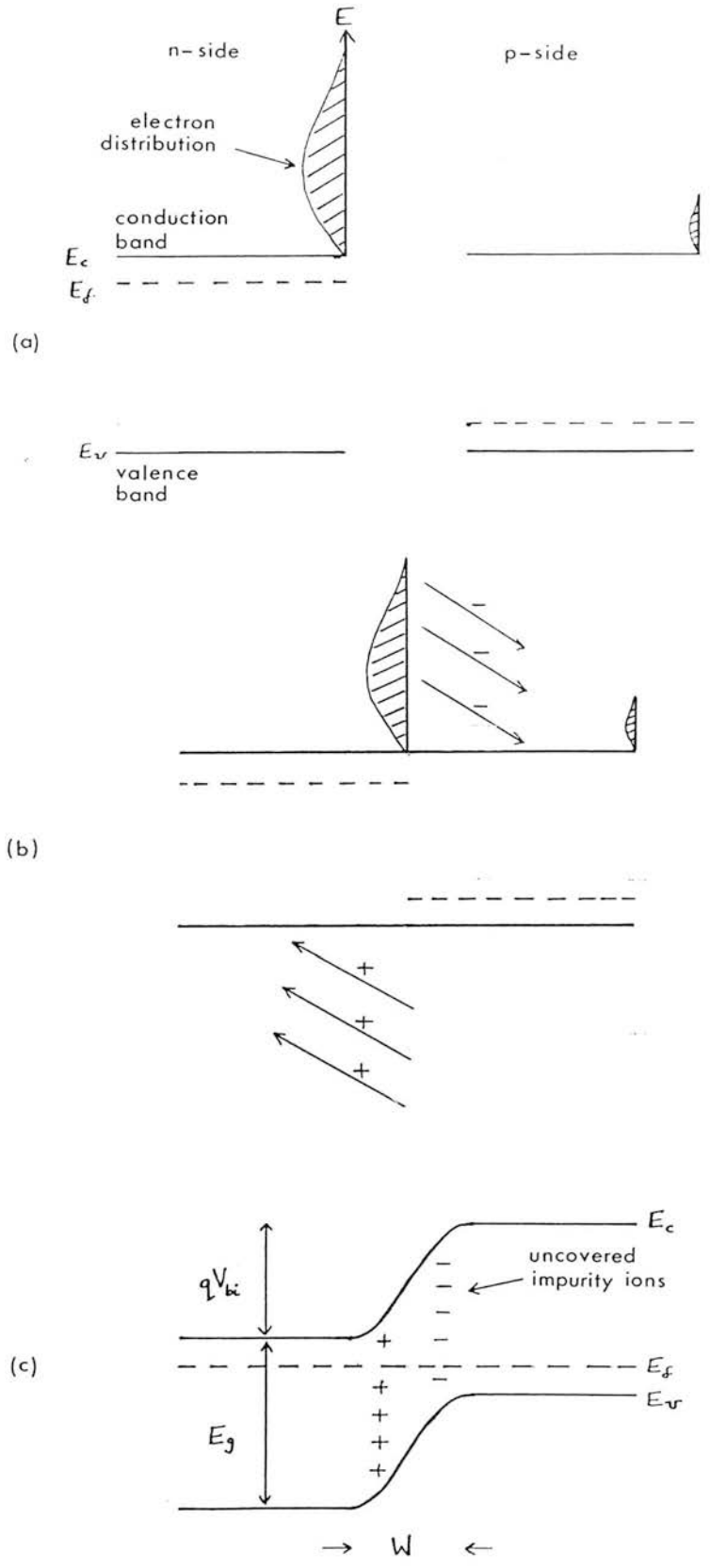

Figure 2.1
The energy levels of n and p type materials (E_V,E_f,E_C refer to the energies of the valence, Fermi and conduction levels respectively); (a) Isolated, (b) Initial contact, (c) Equilibrium, with zero applied bias.

The Fermi levels and carrier distributions for the n and p samples, apart and in contact, are shown in figure 2.1. When contact is made, electrons on the n side are able to lose energy by diffusing into empty states on the p side (and similarly for holes diffusing into the n side). Eventually dynamical equilibrium is established, accompanied by a relative shift in the energy levels, so that the carrier population at any particular energy is the same on both sides of the junction. In other words, the Fermi level is constant throughout the sample and the net current is zero.

An alternative way of picturing this process, is that the initial diffusion of electrons from the n side (high concentration) to the p side (low concentration) leads to a build-up of charge, and thus an electric field, which opposes this flow. At equilibrium the diffusion in one direction is balanced by drift current (due to thermally excited minority carriers ie. holes in the n side) in the opposite.

Due to the loss of majority carriers (ie. electrons in the n side) close to the junction, there will be uncompensated, and immobile, donor ions, which gives rise to a high impedance, depletion (or space-charge) region. A potential barrier is created, represented by the built-in voltage, V_{bi}, which the majority carriers must overcome in order to cross the junction.

Some simple properties of the diode can be derived if the transition from donors to acceptors is abrupt. Also, it is often true that one side of the junction is more heavily doped, and this leads to the one-sided step junction approximation.

Away from the junction, charge neutrality gives $n+N_a = p+N_d$. In order to give overall charge neutrality;

$$N_d . l_n = N_a . l_p$$

where l_n and l_p are the physical dimensions of the n and p depletion layers perpendicular to the plane of the junction boundary, and the total depletion width is $W = l_n+l_p$. The depletion layer extends furthest into

the lowest doped region.

Solving Poisson's equation across this region gives the built-in potential (Boyd, 1983);

$$V_{bi} = \frac{-q}{2\epsilon\epsilon_o} \left(N_d l_n^2 + N_a l_p^2 \right) = \frac{-q}{2\epsilon\epsilon_o} N_d l_n^2 \left(1 + \frac{N_d}{N_a} \right)$$

There is a small correction to V_{bi} in this equation, since the edges of the space-charge layer are not sharp, but are modified by the tail of the majority carrier distribution (Sze, 1981).

For a one-sided step junction (ie. $N_a \gg N_d$, $W \approx l_n$, referred to as p^+n), the relation between the depletion width and V_{bi} is;

$V_{bi} \approx - (q/2\epsilon\epsilon_o) \cdot N_b \cdot W^2$

where $N_b = N_d$ or N_a depending on whether $N_a \gg N_d$ or vice versa. If an external voltage, V, is applied, this will be dropped across the high impedance space-charge layer, so that the width is now given by;

$$W \approx \left[\frac{-2\epsilon\epsilon_o}{q.N_b} (V_{bi}+V) \right]^{1/2} \qquad (2.1)$$

The diode is defined to be forward biased (V positive) if the p side is positive with respect to the n side. A reverse bias, therefore, increases the depletion width and the height of the potential barrier.

By treating the depletion region as two equally charged plates (ie. the charge on the n side is $Q_n = - q.A.l_n.N_d$, A is the junction area) the capacitance can be found;

$$C_j = \frac{dQ}{dV} = A \left[\frac{-\epsilon\epsilon_o q.N_b}{2 (V_{bi}+V)} \right]^{1/2} = \frac{\epsilon\epsilon_o A}{W} \qquad (2.2)$$

Typically, W is of the order of a micron and the junction capacitance is a few x $10nFcm^{-2}$, which for a $75x75\mu m$ detector amounts to a few picofarads.

By increasing the reverse bias, the detector resistance increases and the capacitance decreases, and this has an effect on the noise behaviour.

Also, the capacitance variation with bias may affect the detector linearity.

Similar results are obtained for a diode where N_d-N_a varies linearly across the junction, where $C_j \propto V^{-1/3}$ instead of $V^{-1/2}$.

From equation (2.2);

$$\frac{d(1/C^2)}{dV} = \frac{-2}{A^2.\epsilon\epsilon_0 q.N_b}$$

so that by measuring the capacitance variation with bias, the doping density in the space-charge region, as well as V_{bi}, can be found.

2.2.2 Radiation Response

The photodiode responds to radiation in the following way; a photon is absorbed in the semiconductor, and if it has sufficient energy, will result in the production of an electron-hole (e-h) pair. Both charges are free to move in the material. In order that this event is detected, the charges must be separated by the electric field at the junction. If the diode is open-circuit this will produce an external potential drop, and if it is short-circuit, a current proportional to the flux.

Charge separation will occur immediately if the e-h pair is created at the junction, but as shown, this layer is very thin. It is more probable that the charges will be created in the neutral bulk material, and the minority carrier will have to diffuse to the junction. Thus a high qe detector requires firstly that the photon is absorbed in the bulk and secondly that the charges are within a few minority carrier diffusion lengths (the average distance travelled before recombination) of the junction, so that the thickness of the detector is an important consideration.

The optical absorption coefficient for IR semiconductors is a strong function of wavelength, increasing rapidly towards short wavelengths, so that radiation is absorbed close to the surface, where, due to the presence of trapping states, the carrier lifetime is short. The qe in this

region can be improved by depositing a passivation layer (ie. ZnS) on the surface, and also by maintaining a good vacuum around the detector (Kopeika, 1983).

For InSb at 77K, the light penetration depth at the peak wavelength, λ_p ($\approx 5\mu m$), is $3\mu m$, and the hole diffusion length (in the n side) is $55\mu m$. The diodes are generally a few x $10\mu m$ thick and fabricated as p^+n (as opposed to HgCdTe diodes, which tend to be n^+p).

The cross-section of a typical photodiode is shown in figure 3.3 (and described in section 3.1.1). For an array, the substrate (n-type for InSb) is common to all the detectors. The individual elements are then defined by p-regions diffused onto the substrate, with a metal contact to each acting as the output line.

2.2.3 Operation as an Integrating Detector

In the past, PV detectors have normally been used with a current amplifier, and in order to reduce the noise, the detector bias was maintained at, or close to, zero. This 'short-circuit' mode of operation gives a very linear current response.

In order to work as an integrating detector, the charges accumulating on either side of the junction must be stored until the detector is read out. This can be achieved using the diode capacitance. In practice, a small reverse bias is applied. This increases the depletion width (which has very little effect on the qe), uncovering more immobile charges, which act as an initial charge. The minority carrier flow reduces this charge, so that the external, open-circuit bias is reduced. The signal is thus measured as a voltage change across the detector.

2.2.4 Current Processes

An important characteristic of detectors, which is of particular significance in integrating devices, is the presence of 'dark' current. Dark current refers to the net flow of non-photogenerated charges.

The current-voltage characteristics can be derived by assuming that the depletion layer does not contribute to the current flow, and that the injected minority carriers are not influenced by electric fields in the bulk material (since charge neutrality is maintained by majority carriers attracted to the junction, which recombine with the minority carriers. Thus the minority carrier current at the junction is converted to a majority carrier current in the bulk). The net current is given by the sum of the electron and hole contributions. This is known as the diffusion approximation (Sze, 1981) and leads to the Schockley diode equation;

$$I = I_o \left(e^{V/V_t} - 1 \right)$$

$$I_o = \frac{qA.L.n_i^2}{\tau.N_d}$$

where I_o is given for a p^+n junction, L is the hole diffusion length, τ the hole lifetime in the n side, and $V_t=kT/q$, the thermal voltage (T = temperature).

When a forward bias is applied, the potential barrier is reduced and a large forward, diffusion dominated, current can flow. For reverse bias, the current saturates at $-I_o$, because the diffusion is effectively zero and the thermal excitation of carriers is independent of the junction potential.

This approximation works well for reverse and moderate forward biases.

In addition there are several other sources of dark current, which will become important in certain temperature regimes. Briefly, these are;

(i) Generation-recombination (g-r) current in the space charge layer. At thermal equilibrium, there is a balance between the generation and recombination of charges via trapping states in the bandgap (the rates for direct g-r across the bandgap are much smaller). However, when a forward bias is applied, there is an excess of carriers crossing the junction ($pn>n_i^2$) leading to an enhanced recombination rate. For reverse

bias, $pn<n_i^2$, and generation dominates. In this case the rate per unit volume is given by (Sze, 1981);

$$U = n_i/\tau_e$$

τ_e is the effective lifetime, and the total current is;

$$I_{gen} = A \int_0^W q\,|U|\,dx \approx \frac{A.W.q.n_i}{\tau_e}$$

and is in the reverse direction. The current is thus dependent on the depletion volume, which is proportional to $(1 + V/V_{bi})^{1/2}$.

For a p^+n junction, the current is dominated by holes in the n side so that τ_e refers to the hole lifetime.

An empirical formula, taking account of reverse and forward bias is (Hopkins, 1984);

$$I_{gr} = \frac{2V_t}{R_o} \left[1 + \frac{V}{V_{bi}} \right]^{1/2} \left[e^{V/2V_t} - 1 \right] \qquad (2.3)$$

$$R_o = \frac{2.V_t.\tau_e}{q.n_i.A.W_o}$$

R_o, W_o are the zero-bias dynamic resistance and depletion width.

(ii) Tunneling current. Normally this only becomes important at low temperatures, when the rapid fall-off in n_i causes the diffusion and g-r components to become negligible. For tunneling current to occur, at least one side of the junction must be partly degenerate (this will occur when the Fermi level rises above the conduction band in the n side, so that $|V_{bi}| > E_g(eV)$ or $N_aN_d > n_i^2.\exp(E_g/V_t) > 3x10^{32}\ (cm^{-3})^2$ for InSb at 30K). This, combined with a narrow depletion layer and the availability of empty states at the same energy on the opposite side of the junction, will give a high probability of electron tunneling.

As the reverse bias is increased, so will the reverse tunneling current, since the number of electrons in the p side corresponding to free states in the n side will increase. If there are no free states at the required energy, tunneling can still take place via intermediate trapping

sites close to the junction.

(iii) Leakage currents can occur at the surfaces of the diode due to trapping sites, which contribute g-r current, and surface charges which can create surface depletion regions with their own potential drops. Ohmic leaks can occur due to shorts and thin metallic contacts.

In general, as the temperature drops the dominant current sources are, in order, bulk diffusion, g-r in the depletion layer, and tunneling/surface leakage. For reverse bias InSb diodes, g-r dominates in the region 40-120K, and for short wavelength HgCdTe, this occurs below 240K.

Typical I-V curves for a p^+n diode are shown in figure 2.2.

When the photodiode is illuminated a photocurrent term must be added, $I_\Phi = -q.qe.A.\Phi$ (Φ is the photon flux), which is independent of bias, and has the effect of translating the I-V characteristic in the direction of negative current.

The reason the diode is normally operated with a small reverse bias is that leakage currents are much smaller, and the impedance larger, than in the forward bias direction.

A figure of merit for PV detectors, taking account of the dark current processes, is the product of the zero-bias dynamic resistance and detector area, R_oA. This quantity is independent of the detector size. For a PV device used in a feedback preamplifier circuit, the Johnson noise current will be proportional to $R_o^{-1/2}$, so that a large R_o implies low noise. Also, a high value of R_oA implies low dark current, which means that long integration times can be employed, so that BLIP can be achieved even at low flux levels. The dimensions of the n and p regions are chosen to optimize the quantum efficiency, whereas the doping profiles and densities of a photodiode are designed to give a maximum R_oA at a given temperature.

Also, the higher the operating temperature at which a large R_oA can

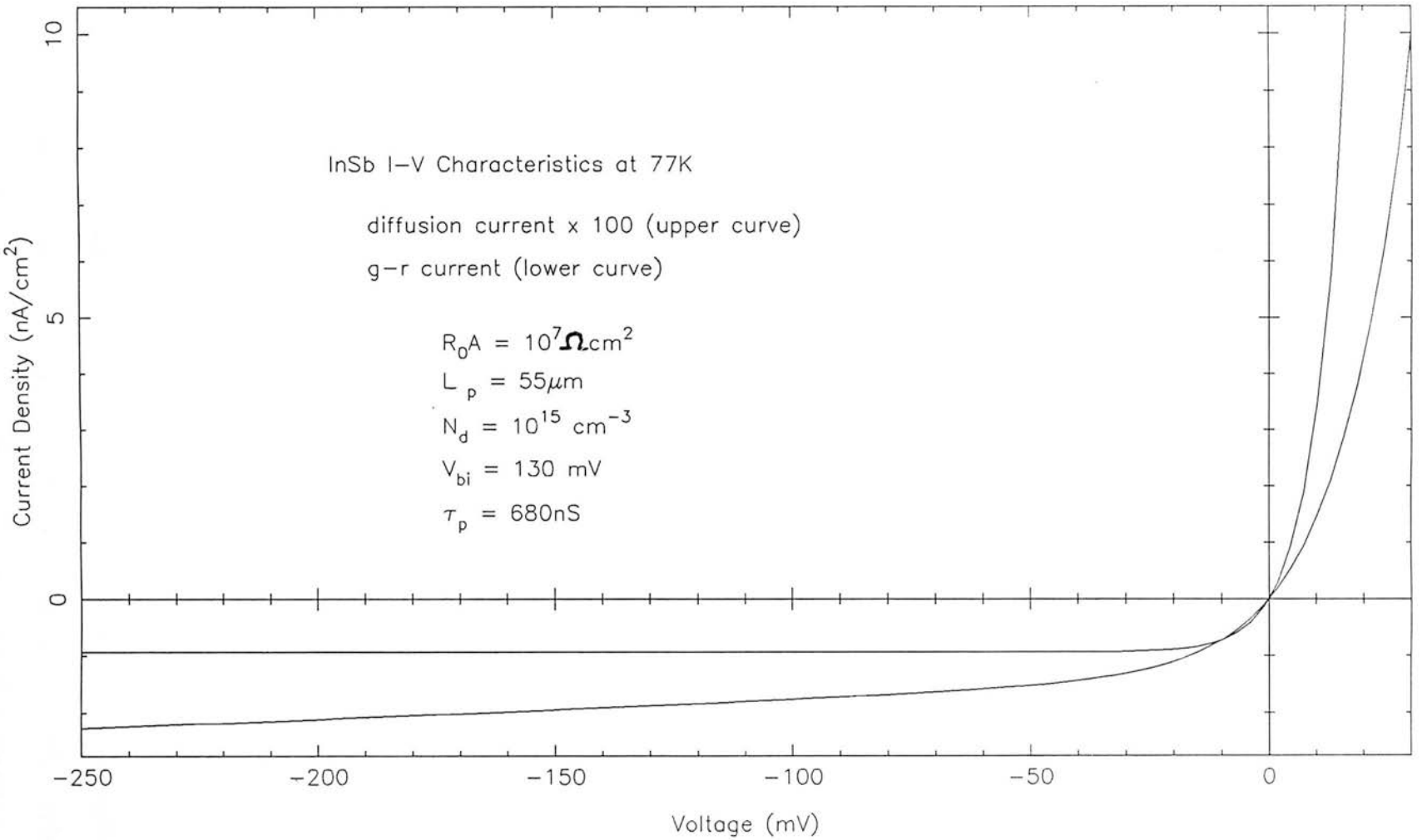
InSb I–V Characteristics at 77K
diffusion current x 100 (upper curve)
g–r current (lower curve)
$R_0A = 10^7 \Omega cm^2$
$L_p = 55\mu m$
$N_d = 10^{15}\ cm^{-3}$
$V_{bi} = 130$ mV
$\tau_p = 680nS$
Current Density (nA/cm^2)
10
5
0
−250
−200
−150
−100
−50
0
Voltage (mV)

Figure 2.2

be achieved, the lower the costs due to cooling requirements.

R_oA can be derived from the current formulae given, and it is found that the temperature dependence is governed by the n_i variation;

$R_oA \propto 1/n_i^2$ (bulk diffusion)

$R_oA \propto 1/n_i$ (g-r current)

$n_i \propto T^{3/2} \exp (- E_g/2kT)$ (Yang, 1978)

As the temperature drops, the rate of increase in R_oA drops until tunneling/surface effects cause it to level off (this typically occurs below 30K for near infrared photodiodes). Typical g-r dominated R_oA figures are;

InSb (77K) 10^7 Ωcm^2

$HgCd_{0.45}Te$ (120K) 10^8 Ωcm^2

InAs (77K) $5x10^8$ Ωcm^2

$Hg_{1-x}Cd_xTe$, where the subscripts refer to the relative proportions of mercury and cadmium, which can be varied to control the wavelength response (Kruse, 1981), offers high performance at relatively high temperatures. PV arrays have been constructed from this material, as well as from InSb and InAs.

2.2.5 The Schottky Barrier Diode

This device consists of a metal-semiconductor junction. The energy levels of the two materials are shown in figure 2.3a (a p-type Schottky diode is illustrated). The work functions Φ_m, Φ_s represent the energies required to move electrons from the Fermi level to the vacuum state, and the electron affinity, χ_s, is the energy difference between the bottom of the conduction band and the vacuum level.

When brought into contact, in order to balance the Fermi levels, there will be a flow of holes from the semiconductor to the metal, depleting the area close to the junction and creating a potential barrier for any further flow, of $\Psi_o = \Phi_s - \Phi_m$ (figure 2.3b).

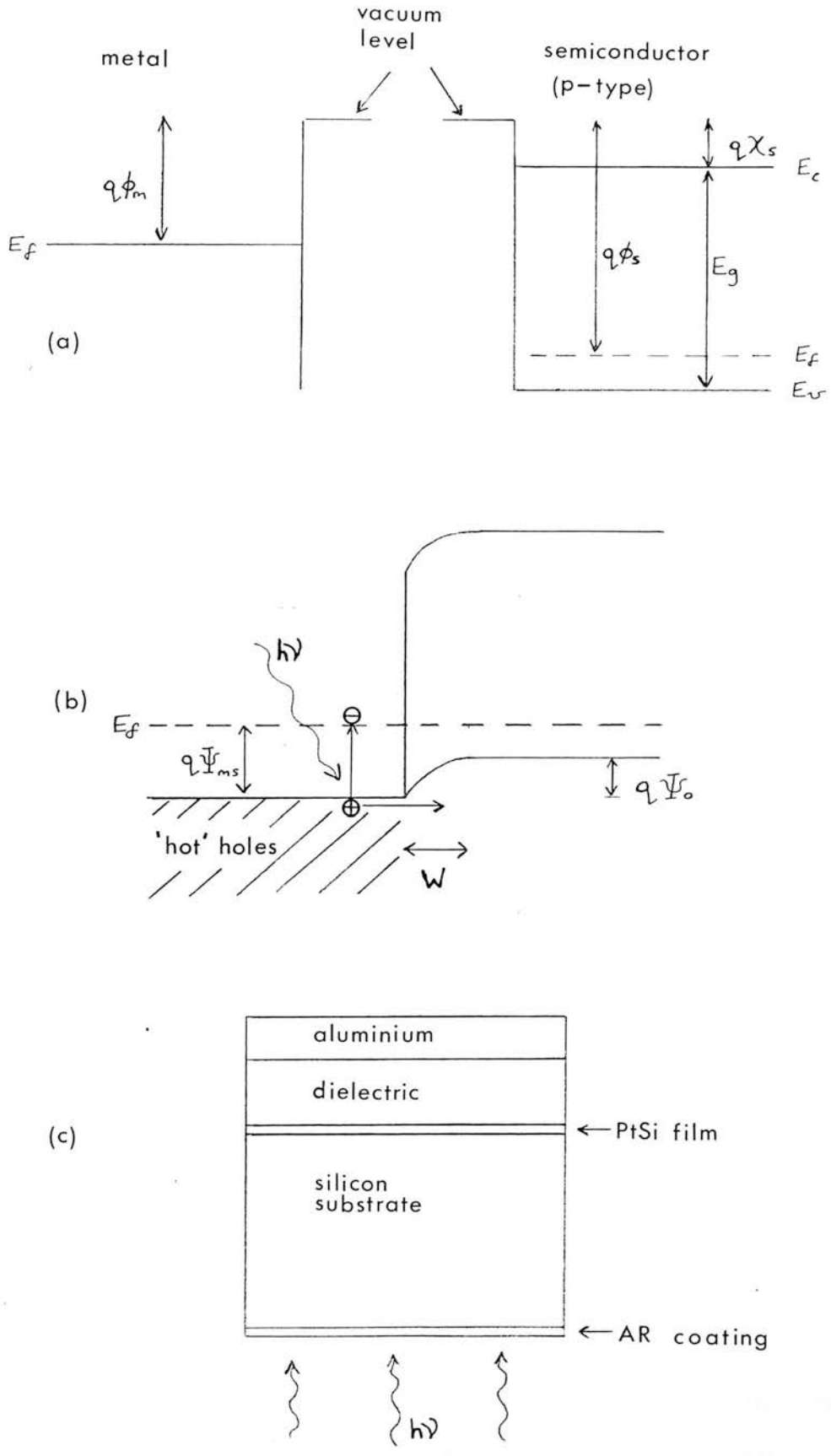

Figure 2.3 : The Schottky Barrier Diode

This junction will behave in a similar manner to a p-n junction, since a forward bias (p-type semiconductor at positive voltage with respect to the metal) will lower Ψ_0 to Ψ_0-V, leading to a large flow of holes into the metal. Thus the current processes are similar, though the flow is due to majority carriers.

For uniform doping, the depletion width is given by the formula for the one-sided step junction (equation 2.1).

The barrier of interest for photon detection, Ψ_{ms}, will be lowered by two effects;

(i) The presence of surface states in the semiconductor.

(ii) Image induced lowering combined with the presence of an electric field outside the metal, known as the Schottky effect; see Sze, 1981.

Schottky detectors have been fabricated using p-type silicon substrates mated to a thin (20-100 angstroms) layer of PtSi. The device is back-side illuminated (figure 2.3c). Photons penetrating the silicon layer, with energies less than the bandgap energy, excite electrons in the metal. If the photon excites an electron above the Fermi level, and the resulting hole has enough energy to overcome the potential barrier, $\Psi_{ms}=\chi_s+E_g/q-\Phi_m$ (ie. a 'hot' hole), then a current will flow. The Schottky diode can be used as an integrating detector in exactly the same manner as described for the photodiode.

The wavelength response is dictated by the transmission of the silicon substrate longward of 1.1μm and the long wavelength cut-off, which occurs at $\lambda_c=hc/q\Psi_{ms}$. The quantum efficiency is enhanced by depositing an anti-reflection coating on the illuminated, rear surface, and an aluminium reflector on the front surface to enhance internal reflection. Though the absorption of thick metals is poor (10%), very thin films of platinum and palladium can absorb 20-60% of the flux. For PtSi detectors the qe is typically 10% at 2μm falling steadily to 0.1% at 5.5μm (Kosonocky, 1983).

The main advantage of these diodes is that they can make use of well developed silicon technology, and it is possible to incorporate them into a CCD readout structure to form a monolithic IRCCD (The IR Handbook, 1978). Devices already constructed in this manner do have the problem, however, of a large amount of dead-space.

Linear arrays, of up to 256 PtSi elements, have been produced for spectroscopic applications (with large aspect ratios to allow matching to an entrance slit), multiplexed by a Reticon shift register (Hudson, 1987). The dark current in these devices is low ($\approx$ 3nAcm^{-2} at 77K).

2.2.6 The Metal-Oxide-Semiconductor (MOS) Capacitor

By inserting an oxide layer between a metal contact and a semiconductor layer, it is possible to form a very simple integrating photon detector. The energy levels for an ideal, n-type, MOS structure are shown in figure 2.4. Due to the insulator, under dc conditions there is no current flow through the device so that the Fermi levels are always flat.

The MOS capacitor operates as a detector in the following way; Initially a large negative pulse is applied to the gate, causing a deep depletion layer at the semiconductor-insulator boundary of width W, consisting of immobile ionized acceptors, N_a cm^{-3}. Since the Fermi level has crossed the mid-gap level, eventually thermally produced e-h pairs will cause the minority concentration to be larger than that of the electrons in this region. Photogenerated minority carriers will also be stored in the potential well, causing the surface potential, Ψ_s, as well as W, to fall.

This device can be thought of as a capacitor, with the oxide layer acting as the dielectric, in series with the depletion capacitance, with equal and opposite charges stored on the metal contact and in the semiconductor. Initially the gate charge is matched by the uncovered donors. Subsequently, since the gate potential remains constant, there

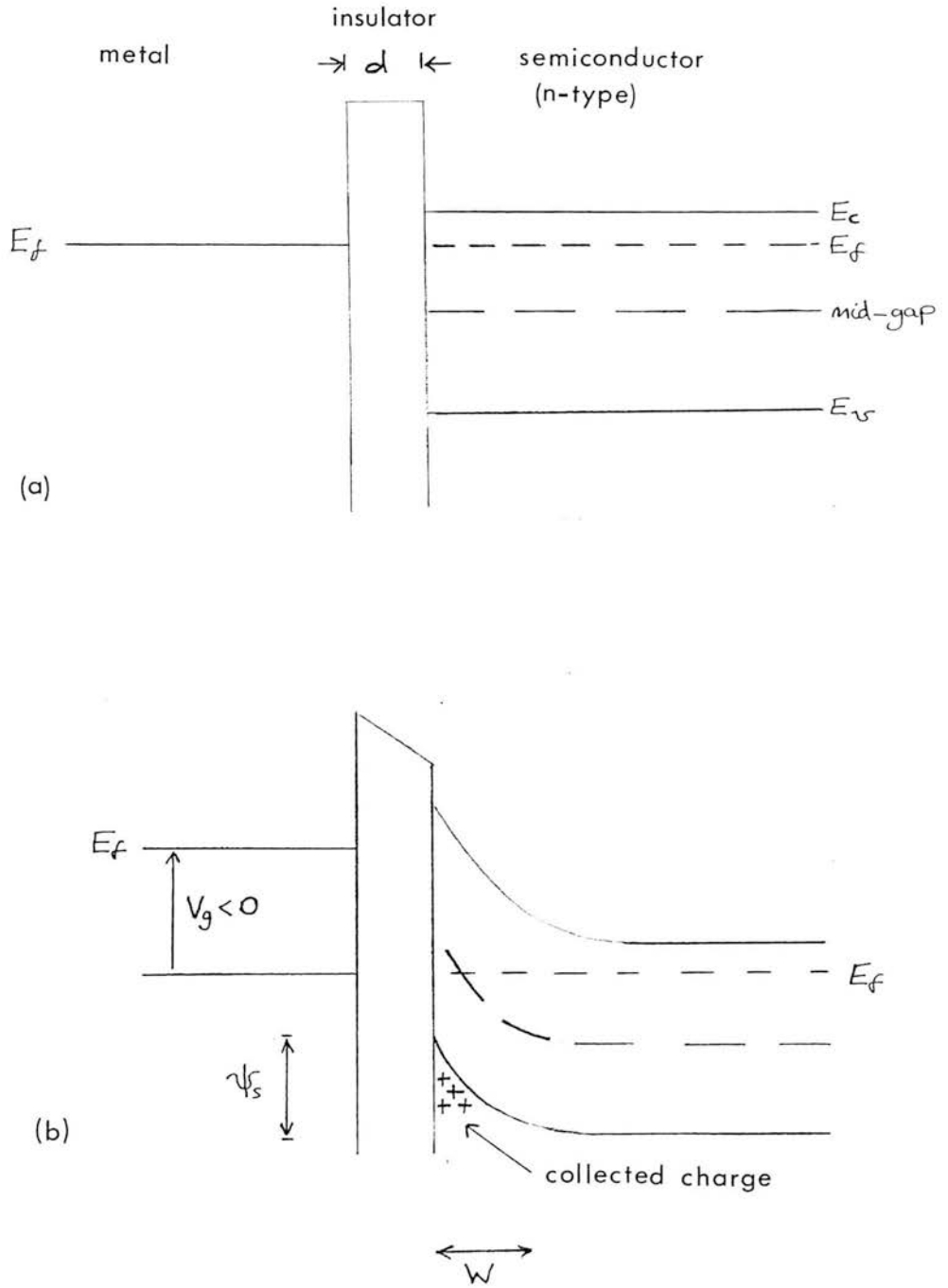

Figure 2.4
The energy levels of the MOS capacitor; (a) Gate voltage zero, (b) Inversion mode. Gate voltage negative.

will be a balance between the mobile and immobile charges in the semiconductor, ie. an increase in one leads to a drop in the other. The maximum size of the signal 'charge packet' will thus be given by;

$$N \approx \frac{\epsilon_i . \epsilon_o . A}{q.d} \quad V_g \quad \sim \text{few} \times 10^6 \text{ el. (for } d=0.1\mu m, A=10\times20\mu m, \text{Si MOS)}$$

d is the thickness of the oxide layer and ϵ_i its relative permitivity. The storage capacity in practice is slightly less than this value since, at saturation, there will still be a residual surface potential.

MOS detectors, due to the depletion region, are susceptible to similar current mechanisms observed in p-n diodes, so that in the absence of photocurrent, the potential well tends to fill up. The time for this to occur is known as the thermal charge-up time. For InSb at 77K, the current is inversely proportional to the minority carrier lifetime (equation 2.3), which is the reason that InSb MOS devices have been constructed on n-type substrates ($\tau_p \sim 200\tau_n$), and τ_{th} ~ 2 seconds.

8-14μm HgCdTe capacitors have been constructed, for which τ_{th} ~ 50μS (77K) and several InSb MOS arrays have been used for astronomical imaging (Joyce, 1984 and Rouan, 1985). The oxide layer (SiO_2) is generally 0.1μm thick and detector sizes are typically 100x100μm. In the optical region, the silicon MOS capacitor forms the detection site on a Charge-Coupled Device (CCD).

The MOS detectors are usually operated so that there is always an inversion charge (minority carriers at the surface) present, as this keeps trapping states occupied, and improves the charge transfer.

It is also possible to use a MOS capacitor in the accumulation mode, where the gate polarity is set so as to cause majority carriers to be collected at the interface. There is no depletion region, so that the band slope is smooth. Since majority carriers are collected, it is necessary to cool below the donor ionization energy to reduce the dark current. The main reason for using this technique is to enable extrinsic silicon MOS

detectors to be formed as part of a CCD structure, since under normal operation (inversion), minority carriers carry the charge. This is incompatible with extrinsic detectors, which are majority carrier devices.

A 16x16 Si:Bi array of MOS detectors used in the accumulation mode, and combined with a CID readout, has been used to obtain images at a range of wavelengths (Goebel, 1986b). The qe was reported to be ≈20%, though at low backgrounds, there were problems with charge trapping.

2.2.7 The Blocked Impurity Band (BIB) Detector

This relatively new detector works on a principle which has been known about for many years. If the doping concentration in a semiconductor becomes very large, a band of states forms in the bandgap, similar in nature to the conduction band, in which ionized impurities (ie. D^+ donor ions) are mobile and can therefore influence the current flow (what is actually occurring is the movement of electrons between closely spaced neutral and ionized donors).

By depositing an undoped, positively biased, blocking layer on top of the heavily doped material, injection of D^+ ions is inhibited, and a depletion region is created which separates photogenerated e^--D^+ pairs.

The high doping level results in a high quantum efficiency.

Detectors have been developed for the long wavelength infrared region (ie Si:As arrays using switched FET readouts (Stetson, 1986)), where few intrinsic materials are available.

The detector must be cooled to reduce the thermal generation of D^+-e^- pairs.

2.3 Readout Schemes

The methods used to read the integrated signals from infrared detector arrays have been adopted from; (i) devices used in the optical region, and (ii) electronic devices, such as memory circuits and shift registers.

The three main readout techniques involve the charge-coupled device (CCD), the charge-injection device (CID), and switched FET arrays, including direct-readout devices (DRO). They all provide a means of multiplexing the outputs of a large number of elements onto a single output line. The output consists of a stream of signal (and reference, or reset) voltage levels.

CCDs, which are fabricated on a silicon substrate, consist of a 2-D array of MOS capacitors arranged in columns and rows. These capacitors represent the individual detection sites, and can be packed together so that the dead-space is minimal. Details of the operation of these devices can be found in Beynon, 1980 and Mackay, 1986.

Briefly, the charge packets are induced to move between adjacent capacitors by the action of a number of clocking waveforms applied to the MOS gates.

The normal readout method used is to shift the charge to a floating output gate (actually a diode), where it is sensed with an on-chip MOSFET amplifier as a voltage drop across the input (node) capacitance. The signal voltage is maximized by minimizing the node capacitance. The magnitude of the depletion capacitance variation with bias can be reduced by making the substrate resistivity high and the diode dimensions small (see equation 2.2), and by placing a larger load capacitance in parallel. Thus, the signal magnitude is reduced, but the MOSFET is operating over a smaller voltage range, and the overall result is a highly linear response. The output diode is reset to its original voltage prior to the arrival of the next charge packet.

The output stage is, generally, similar for each of the readout schemes described.

CCDs, adapted to work in the infrared come in two forms; A monolithic arrangement, where the detecting material also forms the substrate of the CCD. An example of this is the array of 64x128 PtSi

schottky barrier detectors (Kosonocky, 1983). The photogenerated charges are collected in the silicon under the PtSi layer, and at readout are clocked sideways into a MOS capacitor, and then out in the normal manner. The active area of these arrays amounts to less than 50%.

The second form, which is more common at the moment, is the hybrid device, where a layer of detector material is connected to the CCD (surface channel) via an array of indium bumps. The photogenerated charges can be injected directly into the MOS capacitors, but due to the limited charge storage in the CCD (few x 10^6 electrons), low current detectors such as photodiodes and extrinsic photoconductors must be used.

A 32x32 InSb array of this type has been used to obtain astronomical images (Forrest, 1985), and HgCdTe arrays (2.5 and 4.8μm cut-offs) have also been combined with CCDs (Blessinger, 1984 and Lebofsky, 1985. Rieke, 1987, presents results from a CCD camera system used at the Steward observatory.), as well as a photoconductive Si:In (2-7.5μm) array (Tollestrup, 1985). These devices are fairly noisy, compared to optical CCDs, due to trapping of charges at the silicon surfaces. The charge injection efficiency from the detector to the MOS input, may be as low as 60%.

The CID represents an alternative means of extracting the signal from a MOS capacitor. In this case each capacitor is addressed directly. Originally, the signal was obtained by varying the gate potential so as to collapse the potential well, thereby injecting the collected minority carriers into the substrate, where they recombine. The signal was measured as a current pulse.

With modern arrays, this procedure is used to reset the detectors. For two dimensional arrays, a single detector consists of two adjacent MOS capacitors, referred to as collection and sensing sites. By switching the sensing electrode onto a high impedance output line, and then

transferring the accumulated charge from the collection to the sensing site (by altering the former's gate voltage), there will be a change in potential, since the sensing electrode charge has changed. As the charge packet remains at the detector if no reset pulse is applied, a non-destructive read can be performed.

One problem with CIDs is the presence of a response lag, or output response delay to incident flux, at low signal levels. The reason for this effect is poorly understood at present.

Arrays using CID readouts have been constructed from InSb MOS capacitors (1x32 and 32x32, see Fowler, 1982), and from Si:Bi.

The DRO readout scheme, normally used with photovoltaics, is found in a variety of configurations. It uses MOSFET switches to access a selected detector, allow the signal charge to be sensed, and the detector to be reset to an initial bias.

The linear array to be described in subsequent chapters uses this arrangement in conjunction with a Reticon shift register (see section 3.2, for a discussion of its operation). Identical arrays have recently been employed in grating spectrometers (ie. IRSPEC, see Moorwood, 1987, and CGAS, Tokunaga, 1987). This readout arrangement can be extended to 2-D arrays by the use of two shift registers to control the columns and rows (Bailey, 1986).

Another DRO configuration, known as a source follower per detector circuit, or SFD (Orias, 1986), is designed around a unit cell of four MOSFET's (three act as switches, and the fourth, an output source-follower preamplifier, senses the voltage across the node and detector capacitance combination. See figure 2.5). Row and column address decoders are used to select a single pixel, or readout (and reset) the whole array. This circuit allows non-destructive reading, which may be useful in astronomical applications, for example, as a way of monitoring the background in selected regions when the integration time is large.

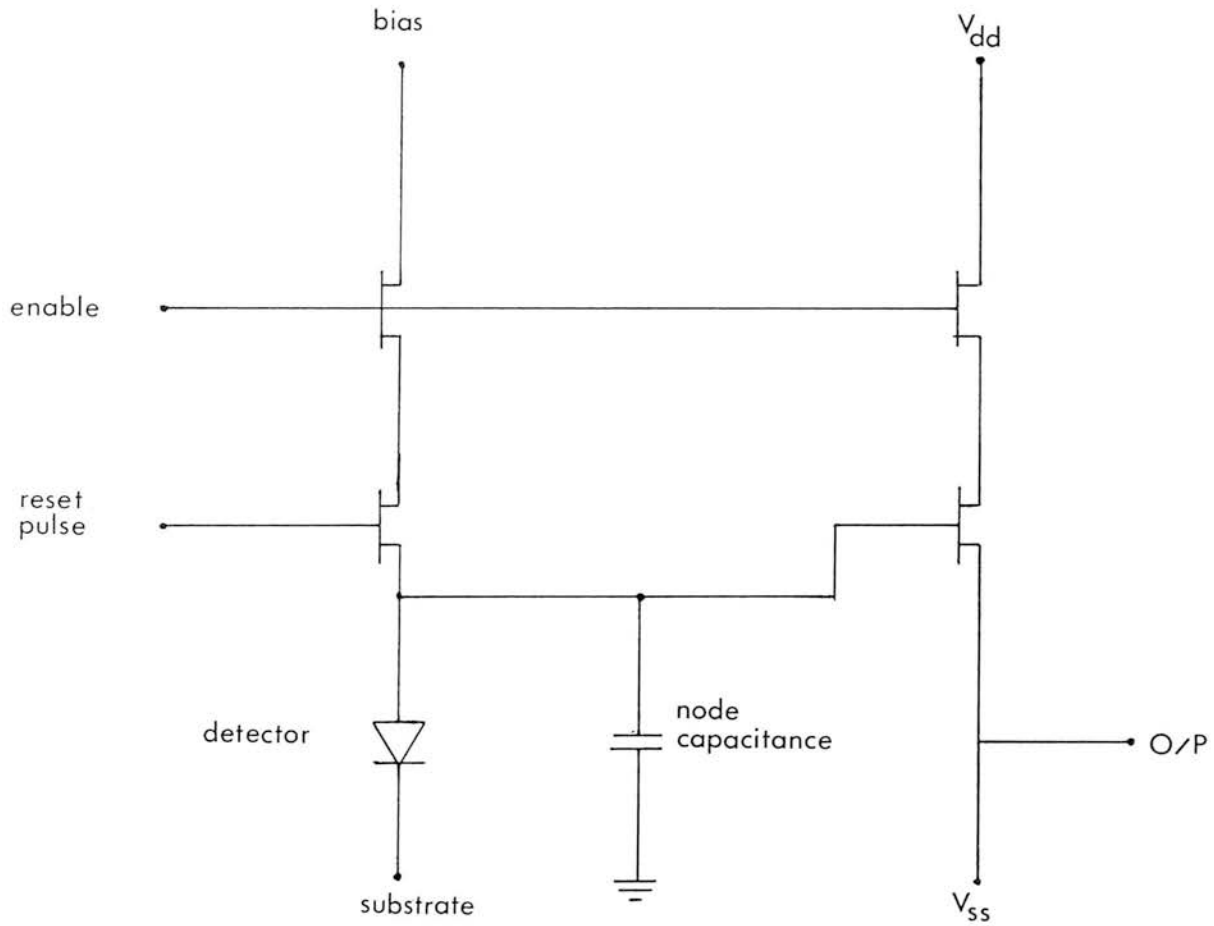

Figure 2.5

Unit cell for SFD circuit

A 58x62 InSb array of this type (manufactured by SBRC) has been incorporated into a camera for use on the 3.8 metre U.K. Infrared Telescope (McLean, 1986). Initial results give a typical pixel read-noise of 400 electrons rms for a storage capacity of 10^6. The dark current at the operating temperature of 35K seems to be very low (a few hundred el/s for a junction area of 65x65μm), and five minute integrations have been performed. BLIP has been achieved at 2.2μm in a 0.6" FOV (field of view), for an integration time of a few seconds.

It is these arrays (as well as HgCdTe arrays for the 1-2.5μm region) which are likely to be used in future imaging spectrometers (ie. CGS 4 and IRSPEC).

2.4 Noise Processes

There are a number of sources of noise associated with infrared sensor arrays, some of which are specific to the readout schemes. In general, the aim is to reduce these contributions to the level where the noise, and thus the sensitivity, is determined by the random variations in the flux of incident radiation.

The fluctuations in the photon flux, which translate to photogenerated charge fluctuations, are described in terms of Poisson statistics (Boyd, 1983). If the mean number of charges collected in an integration time is $\bar{n}$, then the rms variation, or shot-noise is $\bar{n}^{1/2}$.

There will also be shot-noise associated with each of the statistically independent, dark current components present (ie. electron and hole, drift and diffusion currents, etc.).

Other sources of noise are;

(i) Reset or 'kTC' noise. A non-integrating, high-impedance detector, when there is no illumination, operated at zero bias, will have its sensitivity limited by Johnson noise, which is due to the thermal motion of charges and gives rise to a noise voltage across the detector of;

$$V_n^2 = 4kT.R_o.\Delta f$$

The power spectrum of the noise is flat over a large frequency range.

For an integrating detector, however, the signal voltage is sampled with the detector resistance in parallel with a capacitor (ie. node capacitance of amplifier), so that the Johnson noise is effectively filtered by the RC time constant of the circuit.

The rms noise voltage across an RC parallel combination is (Beynon, 1980);

$$V_n = \surd (kT/C)$$

which can be represented as an rms noise charge;

$$N_n = (1/q).\ CV_n = (1/q).\ \surd (kTC) \quad \text{electrons}$$

R_o does not appear in this equation since the increase in Johnson noise due to an increase in R_o is offset by a decrease in the effective noise bandwidth.

This full noise charge would be observed if a switch was incorporated into the circuit in order to reset the capacitor/detector to a given bias, and would represent the uncertainty in the reset voltage, hence the term 'reset noise'.

It is possible to reduce the kTC contribution using a technique known as correlated double sampling, CDS (White, 1974). Considering again the simple RC combination; if two samples of the voltage are taken, separated by time, τ, then it can be shown (Finger, 1987) that the rms noise of the difference is;

$$N(\tau) = (1/q)\ \surd \overline{2kTC\ (1 - e^{-\tau/RC})}$$

$$= (1/q)\ \surd \overline{2kTC} \quad , \ \tau \gg RC$$

$$= (1/q)\ \surd \overline{2kT\tau/R} \quad , \ \tau \ll RC$$

If, for example, the two voltage samples used to derive the signal level can be taken during a phase when the RC value of the detector circuit is large, then the signal noise can be reduced. This is because

the Johnson noise is 'frozen' for timescales $\tau \ll RC$. CDS will also discriminate against '1/f' noise.

Generally, the process of resetting a detector, integrating signal and reading out, combined with the multiplexing arrangement, means that care is needed in the way the signal is derived, if this technique is to be effective. There may be several components of kTC present, not all of which may be removed.

In this respect, the source follower per detector DRO seems well suited to CDS noise reduction, since the voltage across the detector can be monitored constantly in a non-destructive manner.

(ii) '1/f' noise. This is proportional to some power of the current, is not present at zero bias, and may arise from surface currents. As suggested by the name, the noise power is inversely proportional to frequency ($\propto 1/f^{\beta}$, β=1-1.5). 1/f noise is very dependent on the processes involved in preparing the detector contacts and surfaces, and could be a serious problem in integrating detectors.

(iii) Amplifier noise. This generally arises through processes present in most semiconductor devices, ie. Johnson and 1/f noise. The circuit is normally designed with enough gain so that the amplifier noise is not the dominant source.

2.5 Performance of Integrating Detectors

This section is intended to provide a brief description of the important aspects which influence the performance and practical operation of an instrument incorporating a detector array.

Achieving high sensitivity, background limited performance with a given infrared detector can be a non-trivial exercise, due to the large number of variables involved. As a first step towards this aim, the detector is cooled in order to reduce the dark current shot-noise (and allow long t_i's), and the magnitude of the kTC components. The optimum

temperature may also be influenced by qe variations or the operating region of the readout device. The bias used will be dictated by striking a balance between the 1/f noise contribution and the available dynamic range, since the storage capacity increases with increasing reverse bias. Instrumental stability will determine maximum integration times. The net result will be a set of optimum operating conditions tuned to a particular wavelength and resolution.

The following condition is necessary for BLIP;

$$N_e > N_b > N_r^2 \qquad (2.4)$$

where N_e and N_r are the storage capacity and readout noise respectively, and N_b is the number of photogenerated charges collected in a single integration.

The array will be exposed to a range of illumination levels. If the largest signal present is N_b, and provided that N_r is reasonably uniform, a useful quantity to measure is the dynamic range of background limited pixels. This is simply the ratio (in terms of signal) of the brightest and faintest pixels, whose noise is determined by the background radiation, and is given by $f = N_b/N_r^2$. If the spectral, or spatial, contrast is large, $f>>1$ is clearly desirable, with $f_{max} = N_e/N_r^2$.

For a background photon flux, Φ_b, falling on a detector of area A, the minimum detectable power (giving an output signal to noise ratio of unity) will be;

$$P_{min}(W) = \frac{hc}{qe.\lambda} \cdot \frac{1}{t_i} \sqrt{\Phi_b.qe.A.t_i + N_r^2}$$

As t_i is increased there will be a transition from the read-noise limited to the BLIP case, as condition 2.4 is met, and once this has occurred the improvement in sensitivity will be the same whether t_i is increased or readouts are coadded.

For both cases, $P_{min} \propto A^{1/2}$ (if the read-noise is associated with the detector) and the time to reach BLIP, $t_i = N_r^2/\Phi_b.qe.A$ is independent of

area.

Once the detector array is placed in an instrument so that a certain FOV of the telescope is re-imaged onto it, then there are additional factors influencing the sensitivity. If point sources are to be observed then the detector element should ideally be matched to the size of the seeing disk, to reduce both the background (since the detector's FOV is proportional to its area) and the readout noise, though in practice, photometric accuracy necessitates that light is spread over a number of pixels.

For an extended source, a large FOV is desirable to give a good S/N ratio. High sensitivity can be obtained for both types of sources by either combining signals from adjacent pixels (which is most effective for extended sources in BLIP conditions) or employing variable FOV's.

For BLIP, the NEP is;

$$NEP = \frac{hc}{qe.\lambda} \sqrt{2\Phi_b.qe.A}$$

and a figure of merit used to compare different detector materials is D^*, the S/N output per watt of incident power (normalized to unit area and bandwidth);

$$D^* = \frac{qe^{1/2}.\lambda}{hc.\sqrt{(2\Phi_b)}}$$

D^* effectively describes the quantum efficiency, and typical curves for a range of semiconductors can be found in Boyd, 1983.

In practice, the signal from a pixel, for a single readout, will be obtained by differencing the final state with a reference level, which may vary from pixel to pixel (fixed pattern noise), and a number of frames will be coadded. Since the detectors are not identical (there may be variations in the active area, quantum efficiency, initial bias and temperature), the coadded data will not represent an accurate image or spectrum. Two stages of data reduction are required; the first involves

removing offsets (ie. dc offsets and dark current contributions), and the second, correcting for gain variations (responsivity non-uniformities) or 'flat-fielding'. This amounts to inputting a 'flat', or uniform, illuminated field in as similar a manner as possible to the signal field. The output then represents the array non-uniformity (and also any quirks of the optical arrangement, ie. vignetting) which was present in the signal frames. A single flat-field applies a linear correction, so any non-linearities must be dealt with separately, possibly at a later stage using a calibration curve.

The flat-field is normally bright enough so that when it is divided into the signal image, the noise contribution is minimal. If the system stability is good, and the flat-field truly flat and matched in wavelength, then this process would add very little noise. In practice, however, voltage levels drift (as well as bias levels and temperatures) between times when the frames are obtained. The flat-field may be on a different portion of the qe(λ) curve for the detector (more of a problem in broadband cameras), and a more sophisticated dark current correction may be required. In the end, the sensitivity of the result will be degraded.

Various techniques have been used in the optical region to overcome these calibration problems (ie. drift scanning, Mackay, 1982 and adaptive modal filtering, Tyson, 1986), which, when applied in the infrared, should reduce the noise to <1% of the background level (compared with a shot-noise percentage of $100/N_b^{1/2}$ = 0.04% for N_e = 5×10^6, and integrating to full well).

Finally, background subtraction is required at some stage, and this will be dependent on the observing conditions and whether doing imaging or spectroscopy.

CHAPTER THREE

THE CE 32 ELEMENT DETECTOR ARRAY

Introduction

In this chapter a description is given of the detector array obtained by the ROE for possible inclusion in a 1-5 μm cooled grating spectrometer (CGS 4), and which was used for the experimental tests described in subsequent chapters.

The detector package (shown in figure 3.1, with a pin diagram in figure 3.2) was obtained from the Cincinnati Electronics Corporation and consists of the following elements; a linear array of thirty-two InSb photodiodes, where the signal is detected and stored during the integration period, a shift register which multiplexes the detectors onto a single output line, a JFET preamplifier acting as an output buffer, a MOSFET switch for detector resetting and biasing and a temperature sensor. All of these elements are electrically isolated from the case.

Following a brief description of these components, the normal operation of the device is described.

The relation between the output voltage levels and the incident radiation is analysed in detail in order to make predictions concerning signal response.

There are several sources of noise associated with the operation of this device including non-linear effects which are not fully corrected for, noise due to the operation of the MOSFET switches of the shift register and reset facility, preamplifier noise, and the Poisson noise of the accumulated charges on the detector capacitance. The method of sampling may also have an effect on the output S/N ratio, and these topics are dealt with in the final section.

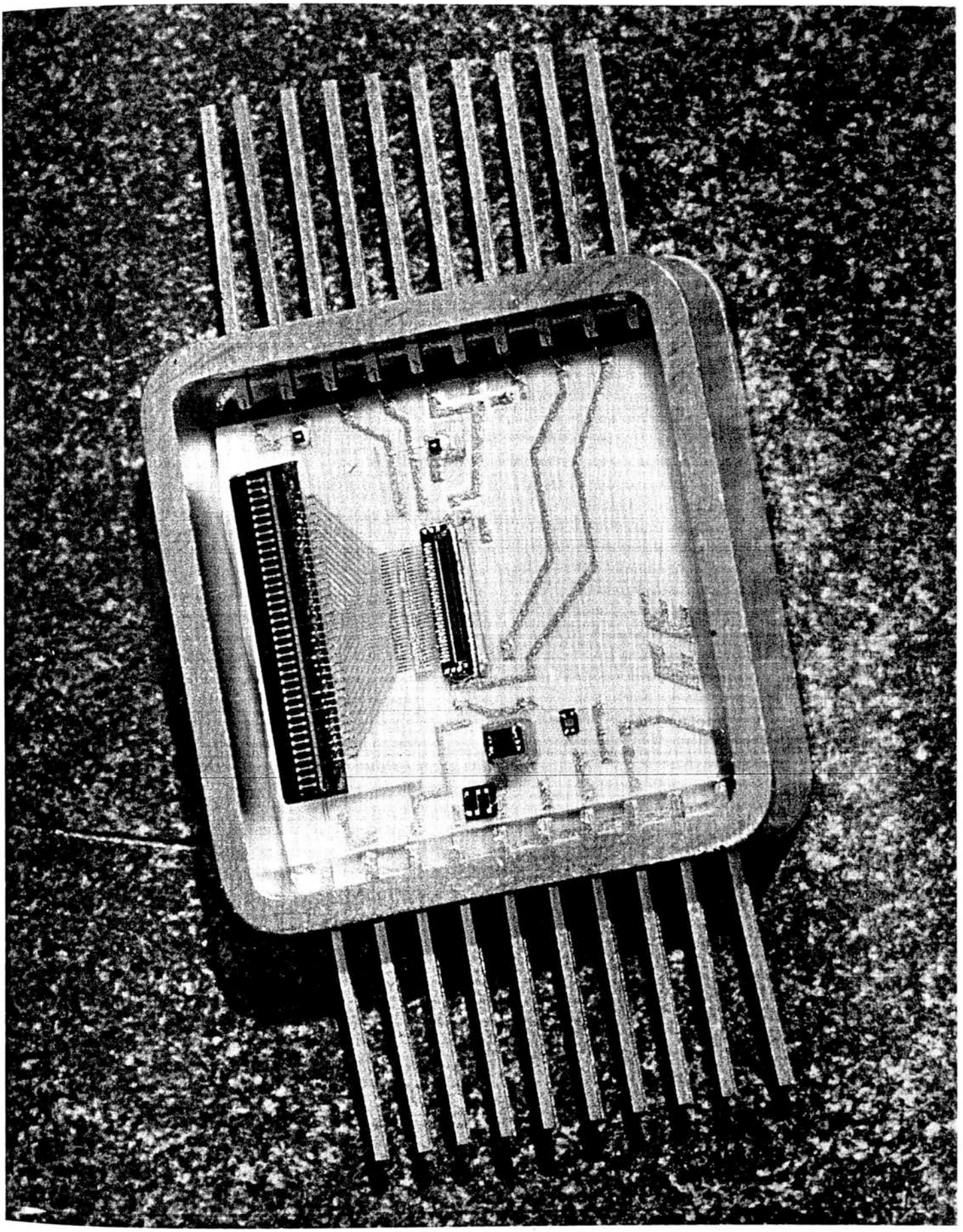

Figure 3.1
The CE array package. For scale, the length of the InSb array (at top of fan-out) is roughly 8mm.

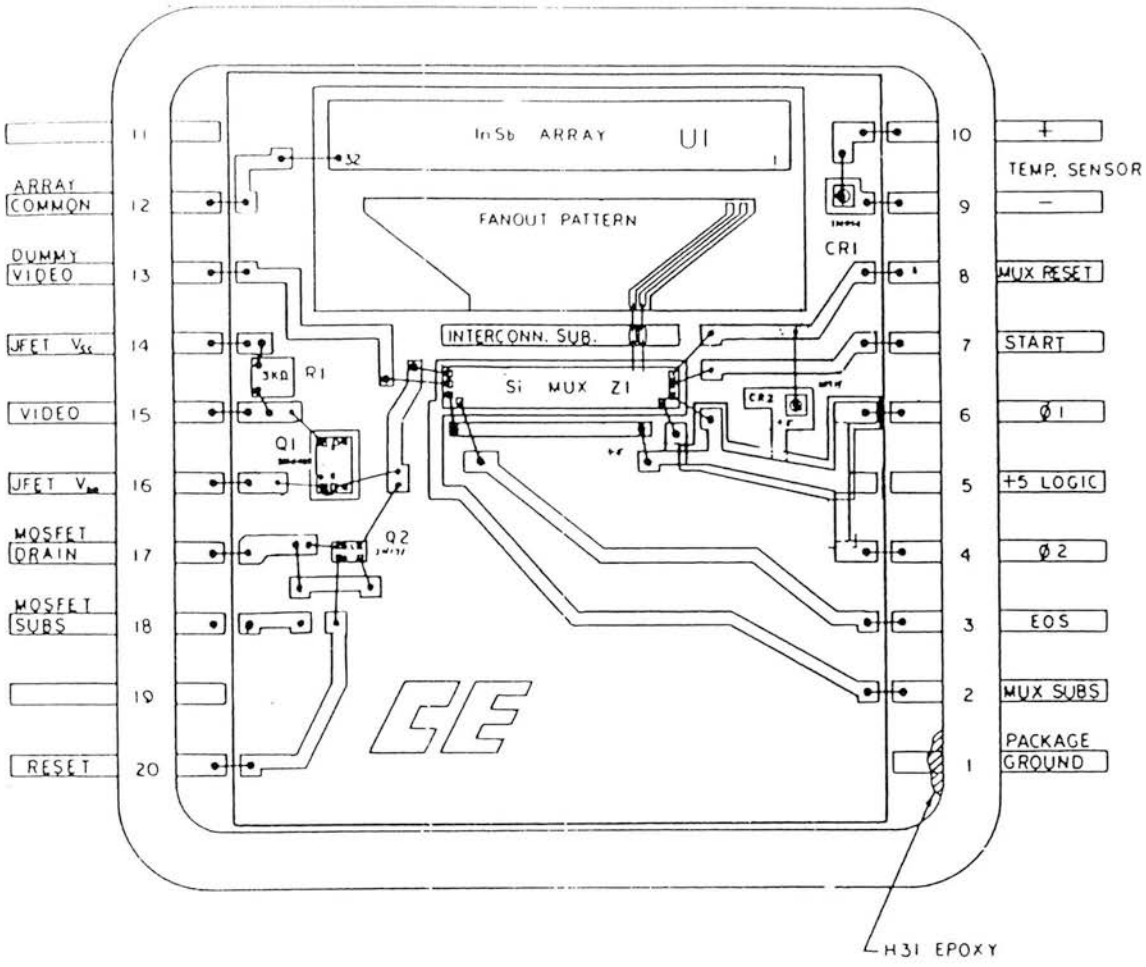

Figure 3.2 : Pin connections and physical layout of array package.

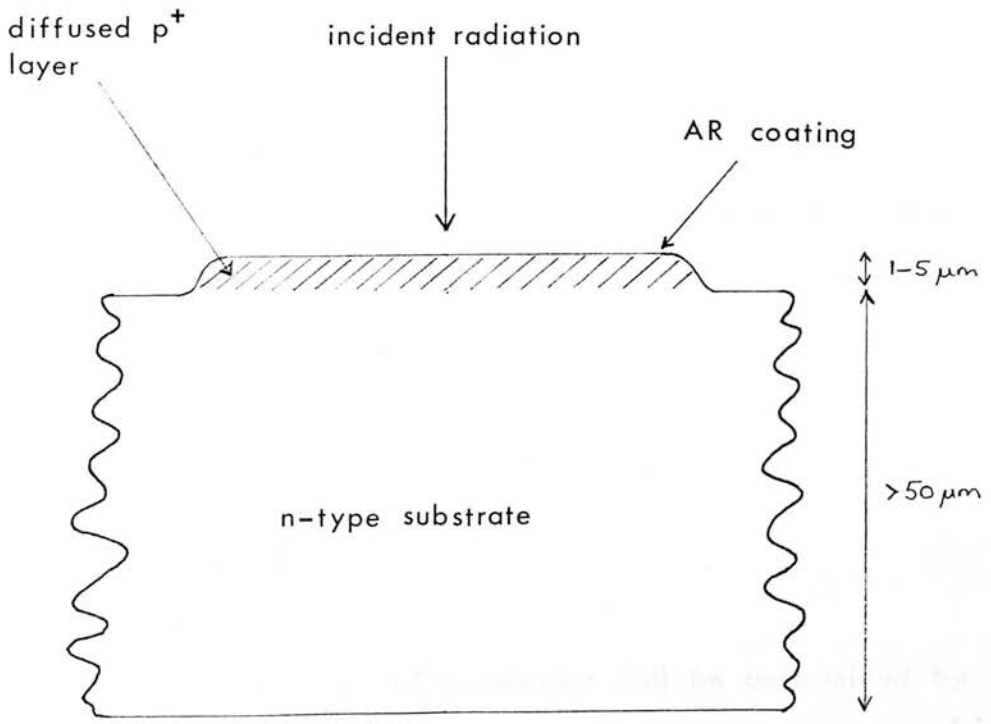

Figure 3.3 : Cross-section of a front-side illuminated InSb photodiode (Schoolar, 1986).

3.1 Description of Circuit Components

3.1.1 InSb Diodes

Each InSb detector (or pixel) has a responsive area of 200x200 μm with a 30 μm gap between adjacent pixels. The cross-section of a single diode is shown in figure 3.3. The doping in the p layer is much larger than in the supporting n type substrate, so that the equations for a one-sided abrupt junction can be applied. The variation of detector capacitance with applied reverse bias is shown in figure 3.4 (This curve was supplied by the manufacturer and represents the average of measurements made on several diodes, which were cut from a processed InSb wafer. The bonding-pad capacitance, C_{bp}, is included). Using this curve, the best fit to equation 2.2 was obtained for the following detector parameters;

$N_d = 8 \times 10^{14}$ cm^{-3}
$C_{bp} = 4.5$ pF
$V_{bi} = -0.16$ V
$W_o = 0.6$ μm

and the total detector capacitance is given by;

$$C_d(V) = (C_d(V=0) - C_{bp}) . (1 + V/V_{bi})^{-1/2} + C_{bp} \qquad (3.1)$$

Another important parameter is the total charge which can be integrated on a detector, as this will partly determine whether BLIP can be achieved, as well as influencing the maximum integration time. The storage capacity (figure 3.5) is given by;

$$N_e(V_i) = \frac{1}{q} \int_{V_i}^{0} C_d(V)\, dV \quad \text{electrons}$$

C_d detector capacitance

V_i initial bias (negative)

The quantum efficiency (qe) of a detector will be determined by the proportion of incident photons which are absorbed within a few minority-carrier diffusion lengths of the junction, so that the

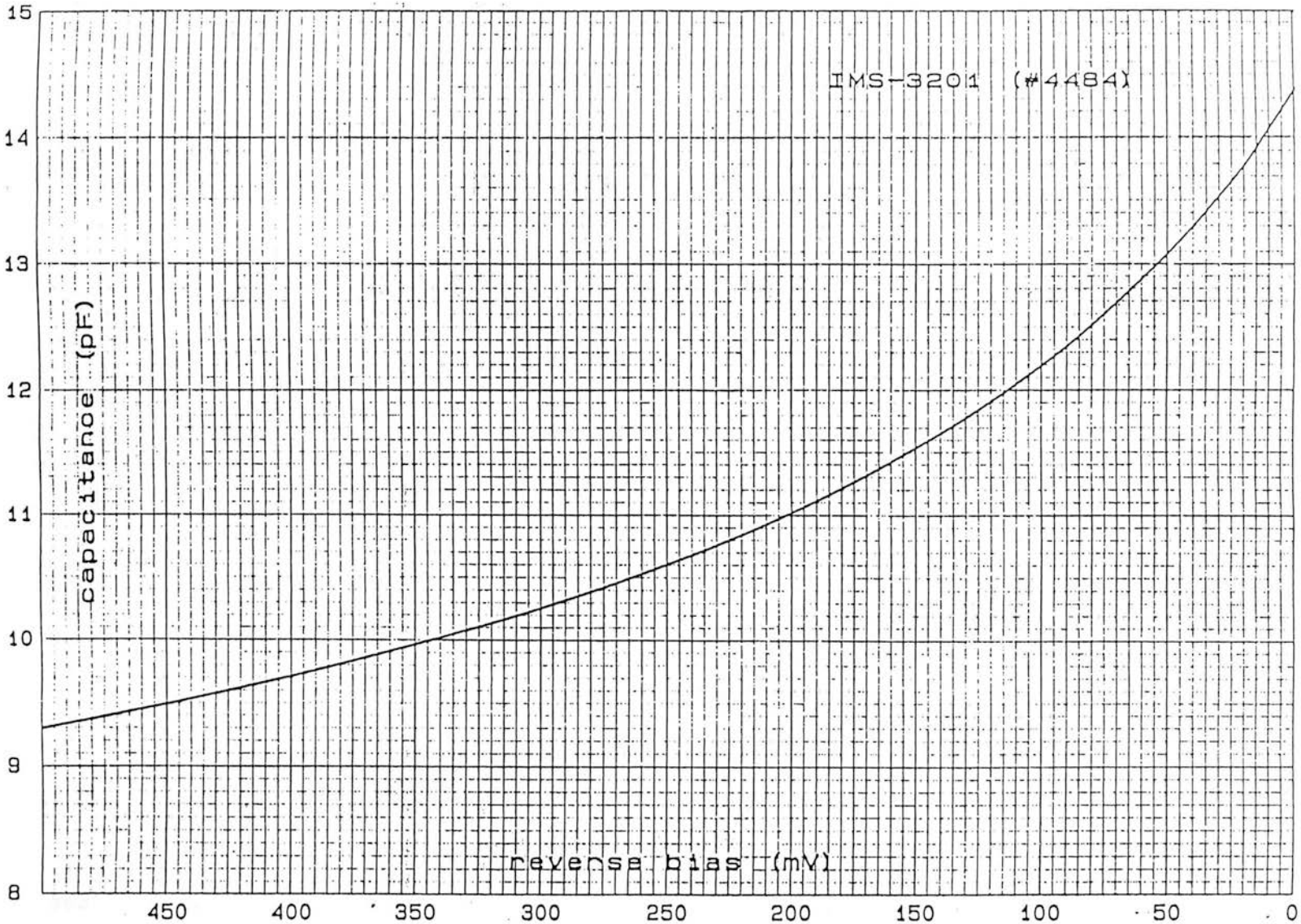

Figure 3.4 : Capacitance curve of a single photodiode, $C_d(V)$.

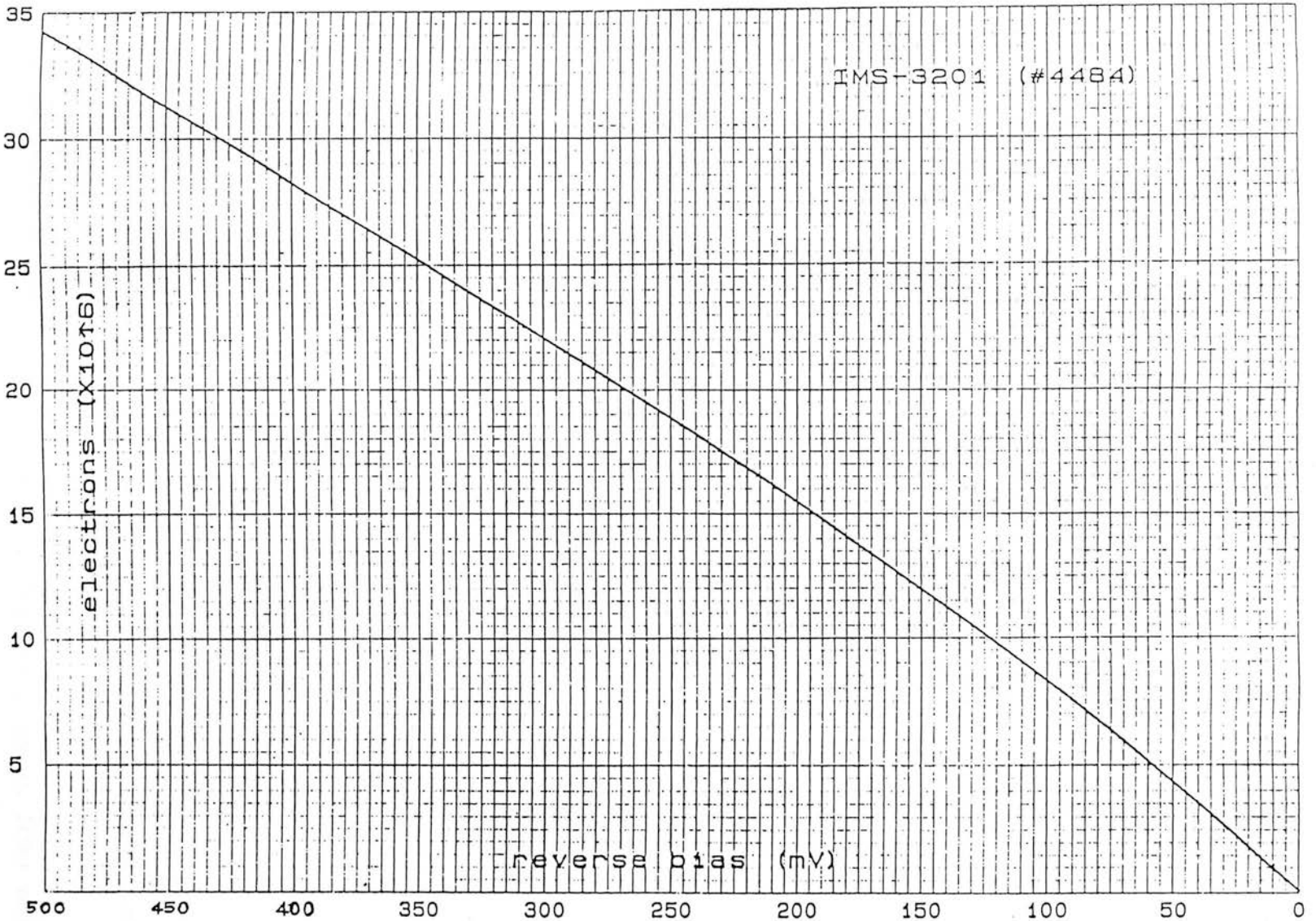

Figure 3.5 : Photodiode storage capacity, $N_e(V_i)$.

electron-hole (e-h) pairs created are separated by the electric field, and contribute to the capacitive discharge of the detector. E-h pairs created too far from the junction will re-combine. CE quote a qe figure of 0.8 for this particular geometry.

Because of the narrow band-gap of InSb, the intrinsic carrier concentration at room temperature is so large that the detector resistance is only a few hundred ohms. In order to reduce the dark current to a level where reasonable integration times can be achieved, the diodes must be cooled below 100 K.

3.1.2 Shift Register

The purpose of the shift register is to process the signals from thirty-two detectors, which are illuminated simultaneously, in order to provide a single, serial output. This multiplexing is achieved by sequentially switching each of the detectors onto a common output line (the video line), which is connected to a preamplifier.

The status of the thirty-two detector switches is determined by the voltage level at the Start input, which is passed along the shift register (and thus presented to each of the detectors in turn) by the action of a two phase, complementary clock, Φ_1/Φ_2. A high voltage level will open the MOSFET switch, whereas a low level will cause it to close.

This voltage is loaded from the Start input each time Φ_1 has a low to high transition.

Under normal operation, a single low level is clocked along the array, accessing each pixel in turn. As the thirty-second pixel is selected an End of Scan (EOS) pulse is generated.

The clocks Φ_1/Φ_2 can be run over a frequency range from several kilohertz up to seven megahertz.

3.1.3 JFET Preamplifier

The JFET (Junction Field-Effect Transistor) preamplifier is configured

in the source-follower mode with the gate connected to the video line. The JFET used (type 2N6483) consists of an n type channel between drain (d) and source (s), surrounded by a p type gate (g), giving rise to a rectifying junction. When the junction is reverse biased the input impedance is large ($>10^{12}\Omega$), so that voltages are effectively frozen on the video line.

The depletion layer, which extends into the channel, affects the drain to source resistance, which can therefore be controlled by the gate voltage.

For preamplifier applications the JFET is operated in the saturation region, where a cross-section of the channel is fully depleted of mobile charges, and I_{ds} is independent of V_{ds}, but dependent on V_g.

The voltage gain of the JFET is (Millman, 1979, pp 402-405);

$$A_j = \frac{r_d\, g_m}{r_d\, g_m + 1}$$

r_d channel resistance (V_{gs}=0) ($\approx$5kΩ at 300 K)

g_m transconductance ($\approx 3.5\times10^{-3}$ A/V at 80 K)

This gives an approximate gain of 0.95 at 80 Kelvin.

The input noise voltage of the 2N6483 is typically 5nV/$\sqrt{}$Hz

3.1.4 MOSFET Reset Switch

The purpose of the reset switch is to allow a detector to be recharged through the bias line in preparation for the next exposure. The MOSFET (type 3N171 n-channel enhancement) operates in a similar manner to the JFET, although in this case, the channel is of opposite carrier type to the drain and source, and is separated from the gate by an insulating oxide layer. When the gate voltage (V_g) is positive with respect to the source, electrons are induced into the channel from the heavily doped drain and source, forming a low resistance path ($\approx$200Ω) between the two. This is the 'on' condition.

For V_g low (ie. zero volts) electrons in the channel recombine with

returning holes, giving the large resistance, rectifying characteristic of two p-n junctions back to back (formed by the combination of n^+ source, p channel and n^+ drain). This is the 'off' state.

The threshold voltage, V_t, above which the MOSFET is on is of the order of a few volts.

3.2 Operation

A schematic representation of the detector circuit is shown in figure 3.6. This, along with the timing diagram (figure 3.7), should be referred to in the following discussion of the normal operation of the array. Table 3.1 lists some of the typical component values.

In order to operate, the device requires a number of d.c. voltage levels (supplies for the JFET, two levels for the shift register) and four driving waveforms (Start pulse, Φ_S, two clocks, Φ_1/Φ_2, Reset pulse, Φ_R). Typical voltage levels are given in table 3.2.

The array common and dummy video pins are grounded, and the external bias is applied through the MOSFET drain. The video and EOS pulse are the only outputs (the on-chip temperature sensor was not used).

The sequence of operation is as follows;

(i) A readout sequence is initiated by the coincidence of a low Φ_S level and a low to high transition of Φ_1. From this point until the EOS pulse, a low level in either Φ_1 or Φ_2 will cause a multiplexer switch to close. Pixel one is accessed by the first low state of Φ_2. At this point there will be a redistribution of charge between the video line and the detector capacitances, causing a voltage change on the video line. Equilibrium is reached after a time of the order of $C_dC_tR_m/(C_d+C_t) \approx 0.05$ μs. This corresponds to the signal portion of the video signal.

(ii) While the detector is still accessed, the reset switch is closed (Φ_R high state) so that the video line voltage is set to the external bias V_{ext},

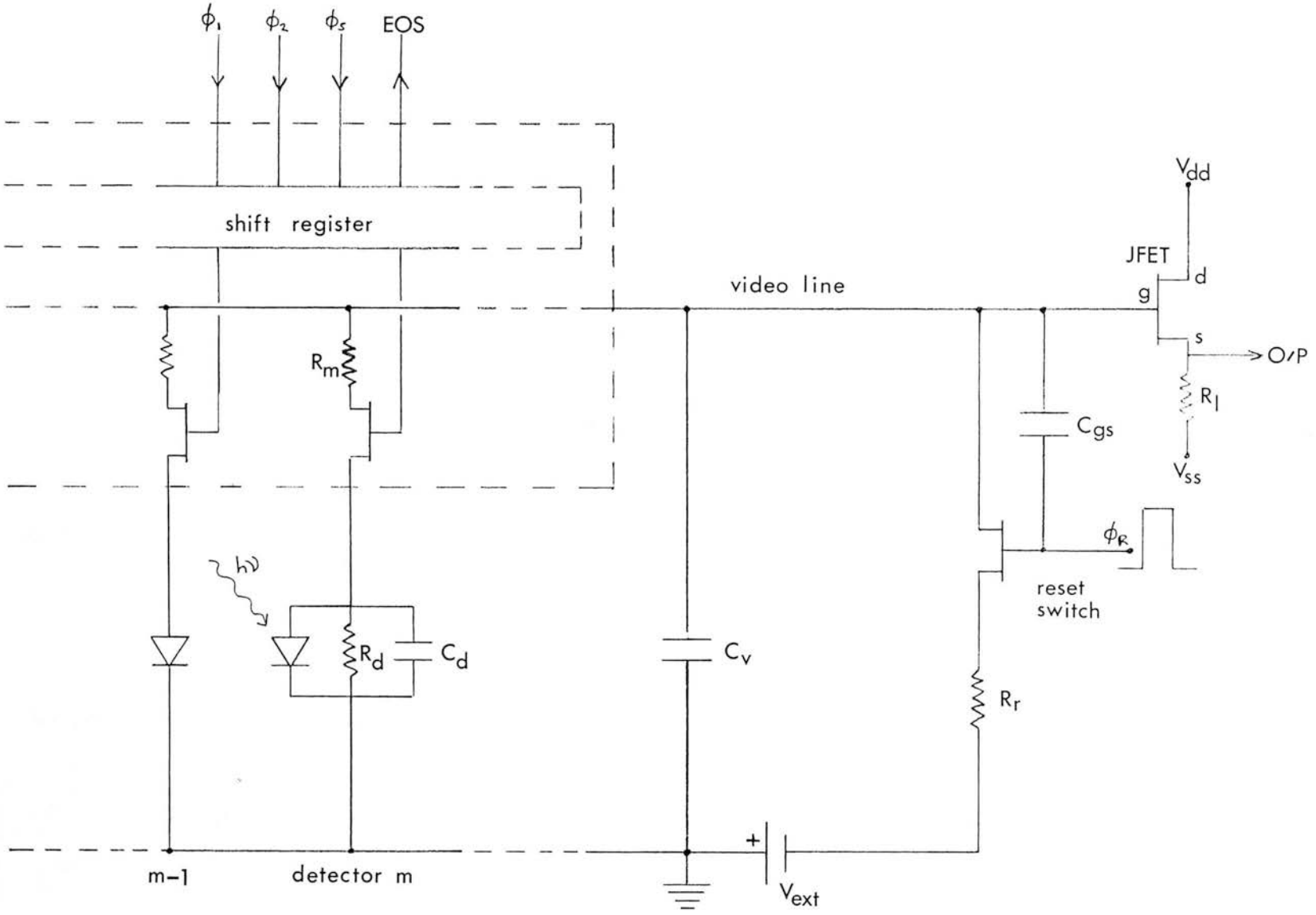

Figure 3.6 : Detector readout circuit

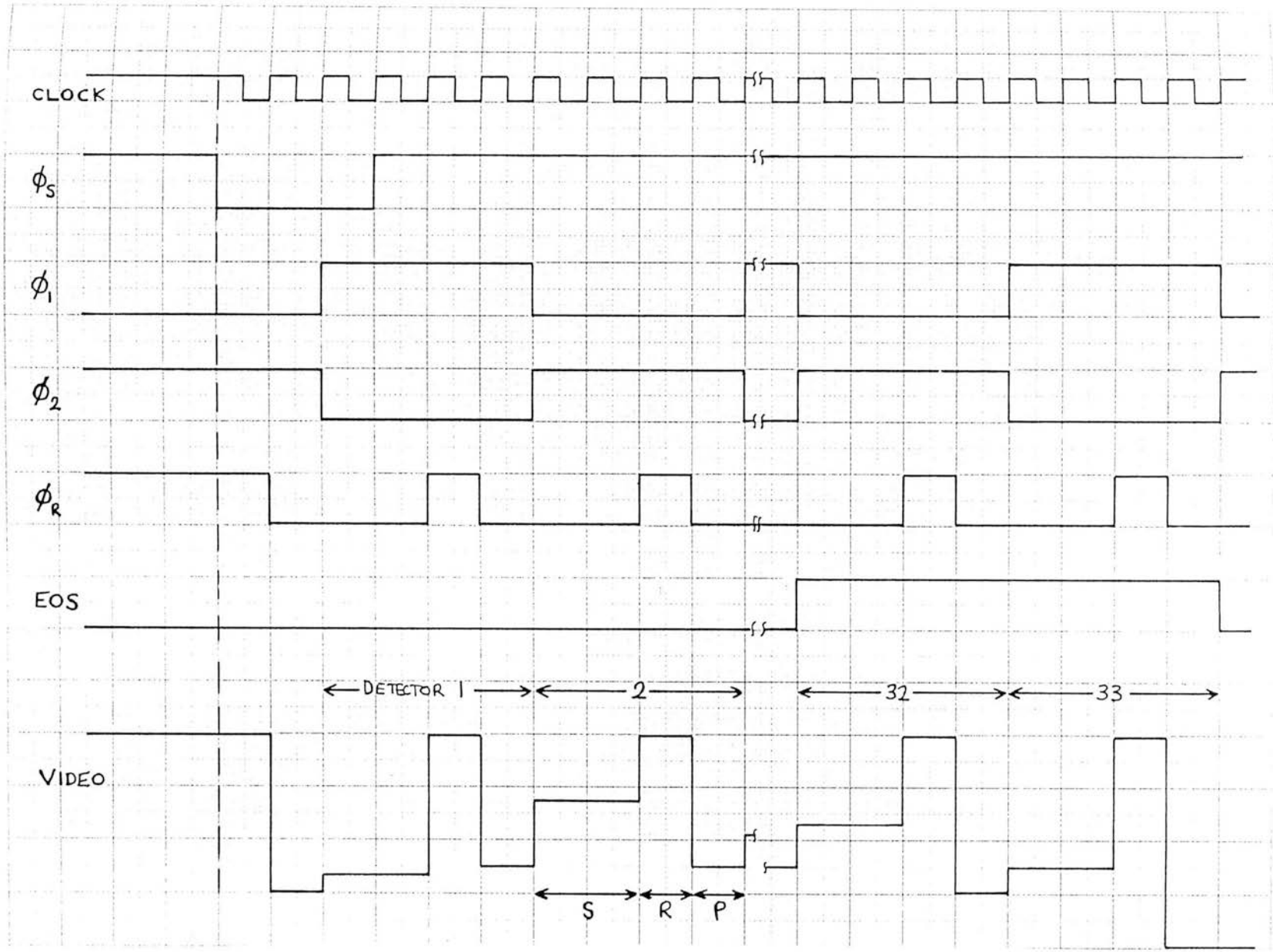

Figure 3.7
Timing diagram (S,R,P refers to signal, reset and pedestal). The clocks are disabled during the integration phase.

Table 3.1 Typical Detector Parameters

Description		Value (at 80K)
detector capacitance	C_d	13 pF
detector impedance	R_d	10^{10} Ω
multiplexer switch 'on' resistance	R_m	7.5 kΩ
reset switch 'on' resistance	R_r	200 Ω
preamplifier load resistance	R_l	3 kΩ
video line capacitance	C_v	12 pF
reset switch gate-source capacitance	C_{gs}	1 pF
preamplifier gain	A_j	0.94
InSb quantum efficiency	qe	0.8
mean voltage transfer efficiency	$\overline{VTE}$	0.5
mean charge transfer efficiency	$\overline{CTE}$	0.04 pF^{-1}

Table 3.2 Typical Voltage Levels and Timing

Description		Value
Start	Φ_s	-5/+4 V
clocks	Φ_1/Φ_2	-8/+3 V
Reset	Φ_R	0/+3 V
JFET supply voltages	V_{ss}	-4 V
	V_{dd}	+8 V
multiplexer supply voltages	reset	+4 V
	substrate	+6 V
array common		0 V
dummy video		0 V
fundamental clock frequency (fig.3.7)		78 kHZ
pixel time		51 μS
minimum readout time (34 pixels)		1.7 mS

which is negative, and the detector becomes reverse biased. This represents the reset portion of the video.

(iii) When the reset switch is opened, some of the reset pulse voltage is coupled through C_{gs} onto the video line (the amount will depend on the switching characteristics of the MOSFET), which acts to increase the detector reverse bias by an amount V_{int}, the internal bias. V_{int} can be inferred by charge conservation between the two states in figure 3.8;

$$V_{int} = \frac{-\Delta V_R . C_{gs} + V_{ext} \left[C_d(V_{ext}) - C_d(V_{int}+V_{ext}) \right]}{C_d(V_{int}+V_{ext}) + C_t} \qquad (3.2)$$

$C_d(V)$ throughout the text refers to the detector capacitance at an external voltage, V, normally in the reverse bias direction.

$C_t = C_v + C_{gs} = 13pF$ at 80 K

C_v represents the total stray capacitance of the video line, and includes contributions from the shift register, the reset MOSFET and the input of the JFET.

$\Delta V_R \approx V_t - V_L$, is the voltage coupled through C_{gs}.

If $C_d(V)$ is constant, equation (3.2) reduces to;

$$V_{int} = \frac{-\Delta V_R . C_{gs}}{C_d + C_t} \qquad (3.3)$$

For $\Delta V_R = 2.5$ V, $V_{int} \approx -100$ mV

The video signal is now at the pedestal level, the detector is in its initial state with a total bias, $V_i = V_{int} + V_{ext}$, and will be detached from the output line when Φ_2 returns to the high state.

This sequence is repeated for all thirty-two detectors. It is worth noting that the action of the multiplexer MOSFET switches also gives rise to capacitive coupling onto the detector and video line, though the induced voltages are smaller than V_{int}, since the gate-source capacitances are smaller. As the even pixels are controlled by Φ_1 and the odd pixels by Φ_2, any differences in the clock profiles will lead to an odd/even voltage difference, which is referred to as the odd/even effect (and can

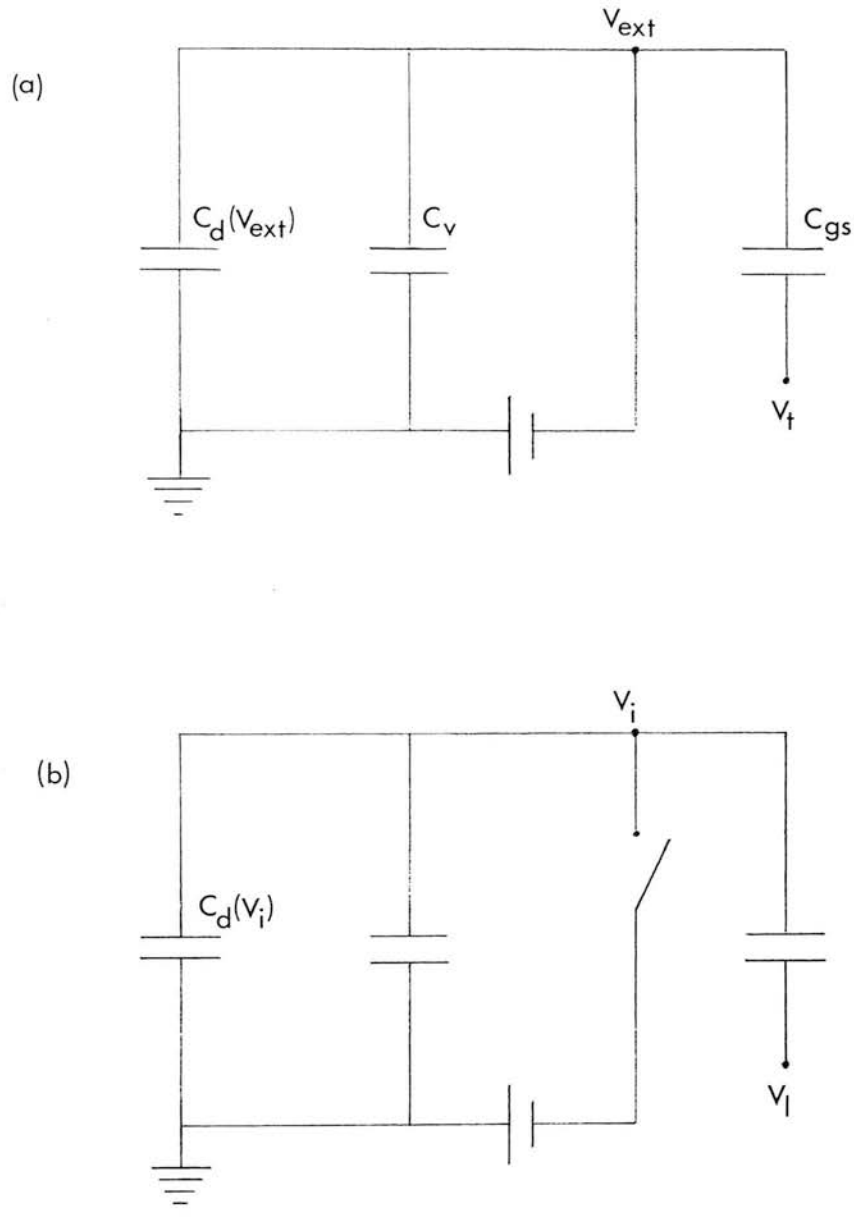

Figure 3.8
Derivation of internal bias; (a) Detector circuit immediately before reset switch opens, (b) Circuit during pedestal portion of readout.

be observed as a modulation of the signal levels).

(iv) After the EOS pulse all the detectors are isolated and can integrate signal. The initial charge is reduced by photocharge and dark current (which will be determined by the reverse diode I-V characteristics), and the detector discharges toward zero bias (in certain circumstances, ie. a high level of illumination, it is possible for the detector to become forward biased. See chapter 5).

During the integration phase the driving waveforms are disabled, and the video line is held at V_{ext}, to reduce noise pick-up at the array.

(v) After an integration time, t_i (the time separating two consecutive start pulses), another readout is initiated.

The time spent on a single pixel, which relates to the readout rate, will be determined by the settling times of the levels (signal,reset,pedestal) and the sampling speed of the data acquisition system. It may also be necessary to consider the minimum t_i which will allow the array to operate in high background conditions.

3.3 Detector Signal Response

In the detection process it is important to be aware of the relation between the input and the derived output signal, in order to compare and calibrate widely varying output levels. In this section this relation will be derived by analysing the state of a detector at each point of operation, from the initial bias to readout. The purpose of doing this is to find the conditions which will give the most linear response, and these results will then be compared with experimental results in chapter 5.

The relation between the output signal and the amount of radiation incident on the detector during t_i is complicated by two effects;

(i) The detector capacitance is a function of bias (figure 3.4)

(ii) Charges left on the video line by pixel m-1 will contribute to the signal level of pixel m.

The output response is derived in the following manner;

At readout n-1, the pedestal of pixel m represents the initial state of this detector. Figure 3.9a shows the waveform and equivalent circuit at this point. For an initial bias V_i, the total charge in the circuit is;

$$Q_1 = C_d(V_i).V_i + C_t.V_i$$

Assuming that the dark current is zero during the integration period, the detector is discharged at a steady rate, so that the charge change, ΔQ_d, is;

$$\Delta Q_d = q.qe.\Phi.t_i = C_d(V_f).V_f - C_d(V_i).V_i$$

Φ incident flux (photons/pixel/second)

V_f represents the voltage across the detector after t_i but immediately prior to readout (figure 3.9b), and the charge in the circuit is now;

$$Q_2 = Q_1 + \Delta Q_d \qquad (Q_1, Q_2 \text{ -ve}, \ \Delta Q_d \text{ +ve})$$

Since

$$V_f = V_i + \Delta V_d \qquad (V_i, V_f \text{ -ve}, \ \Delta V_d \text{ +ve}),$$

there is a non-linear relation between the charge and voltage changes during the integration, given by;

$$\Delta V_d = \frac{\Delta Q_d}{C_d(V_f)} - V_i \left[1 - \frac{C_d(V_i)}{C_d(V_f)} \right] \qquad (3.4)$$

The video line voltage at this time is V_i'. For simplicity assume that pixels m-1 and m have equal capacitances so that $V_i' = V_i$ (from eqn. (3.2)).

During readout (figure 3.9c) there will be a redistribution of charge between C_d and C_t, until they achieve equal voltages. At equilibrium, therefore, the total charge is;

$$Q_3 = C_d(V_i+\Delta V_v).(V_i+\Delta V_v) + C_t.(V_i+\Delta V_v)$$

and the video line voltage is now;

$$V_s = V_i + \Delta V_v \qquad (V_i, V_s \text{ -ve}, \ \Delta V_v \text{ +ve})$$

A measure of the integrated signal of pixel m is given by ΔV_v, which

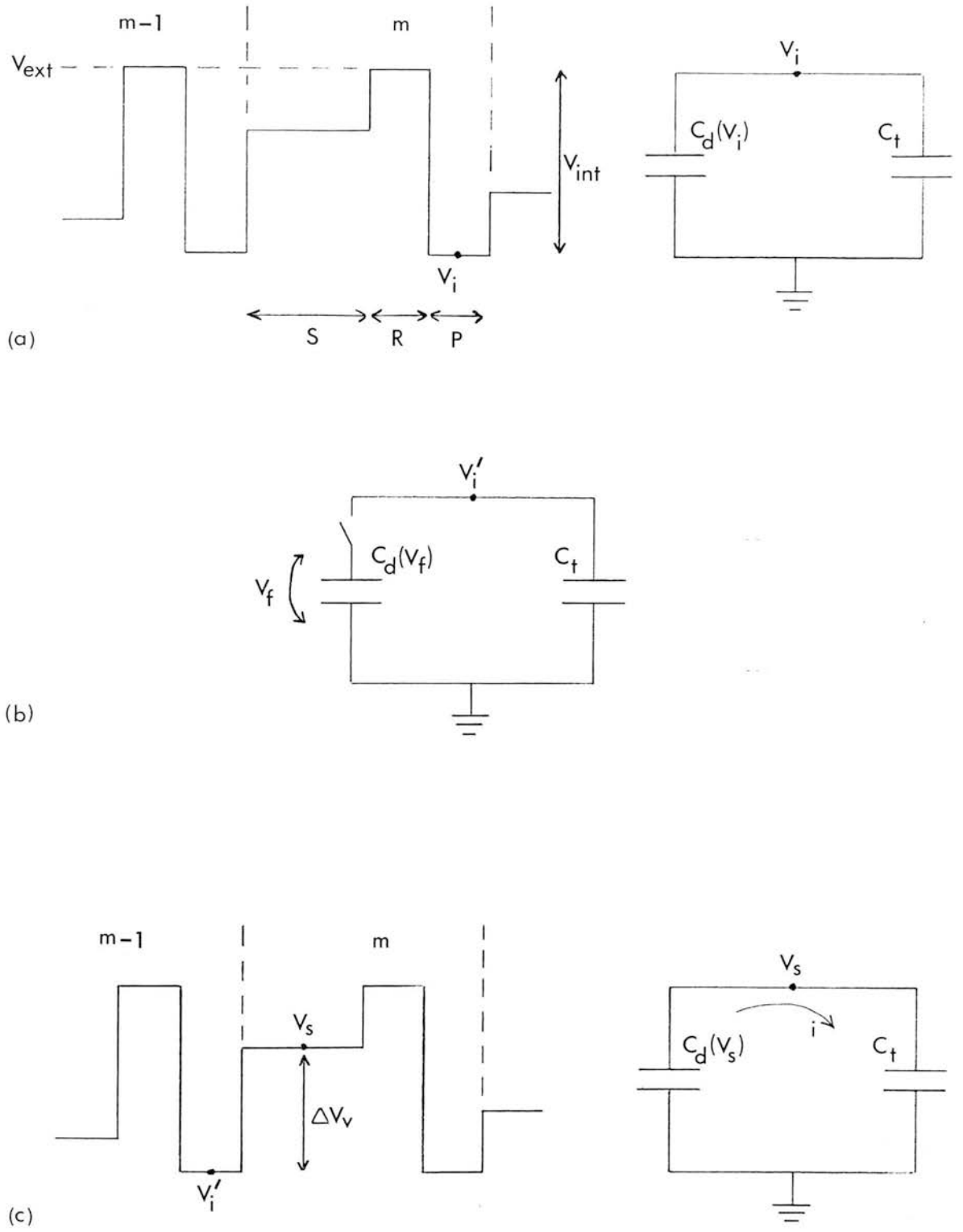

Figure 3.9
Video output and equivalent detector circuit for derivation of signal response; (a) Initial state, readout n-1, (b) After integration, immediately before readout, (c) Final state, readout n.

can be derived in terms of ΔV_d by applying charge conservation, $Q_3 = Q_2$;

$$\Delta V_v = \frac{C_d(V_f)}{C_d(V_s) + C_t} \left[\Delta V_d + V_i \left\{ 1 - \frac{C_d(V_s)}{C_d(V_f)} \right\} \right] \qquad (3.5)$$

For the simple case, $C_d(V)$ constant,

$$\Delta V_v = \left[\frac{C_d}{C_d + C_t} \right] \Delta V_d \qquad (3.6)$$

The term in brackets, referred to as the Voltage Transfer Efficiency (VTE), represents the coupling of detector voltage onto the video line and has a value of ≈ 0.5. The variation of the VTE predicted by equation 3.5 is shown in figure 3.10.

In terms of charge, again for the simple case;

$$\Delta V_v = \frac{\Delta Q_d}{C_d + C_t} = CTE.\Delta Q_d \qquad (3.7)$$

The Charge Transfer Efficiency (CTE) relates the incoming radiation to the change in initial and final detector states as seen on the video line, ΔV_v. In effect, it represents a form of signal gain whose value depends on the readout point. By substituting eqn. (3.4) into (3.5) a more accurate version of the above is;

$$\Delta V_v = \frac{\Delta Q_d + V_i \left[C_d(V_i) - C_d(V_s) \right]}{C_d(V_s) + C_t} = CTE(V_i, V_s).\Delta Q_d \qquad (3.8)$$

and the resultant variation of CTE with bias and readout point is shown in figure 3.11, which is plotted as 1 - CTE/initial CTE (see section 5.3). The initial CTE is the value of CTE as ΔV_v approaches zero, which is different from the quantity $1/(C_d(V_i)+C_t)$.

From this curve it can be seen that there is a small variation ($\approx$2%) in the CTE for a reasonable bias and a range of signal levels up to saturation (when V_f=0). Also, for a given detected signal, this model predicts that the non-linearity increases as the initial bias is reduced, probably due to the increasing steepness of $C_d(V)$ as V=0 is approached.

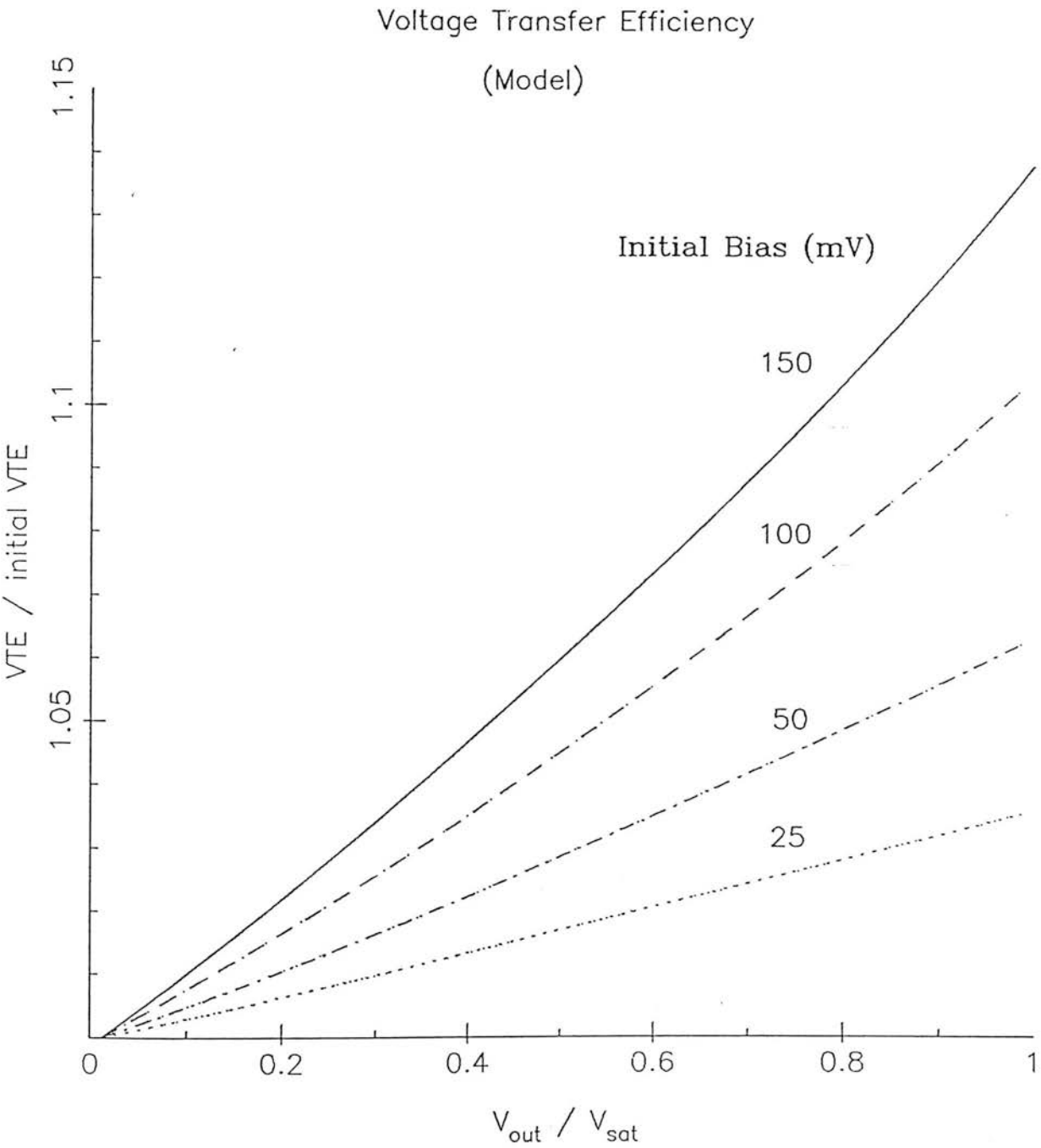

Figure 3.10
VTE as a function of readout point and bias (derived using CE capacitance data and equation 3.5, with the approximation $V_s=V_i+\Delta V_d/2$).

Bias	Initial VTE
25	0.50
50	0.48
100	0.45
150	0.43

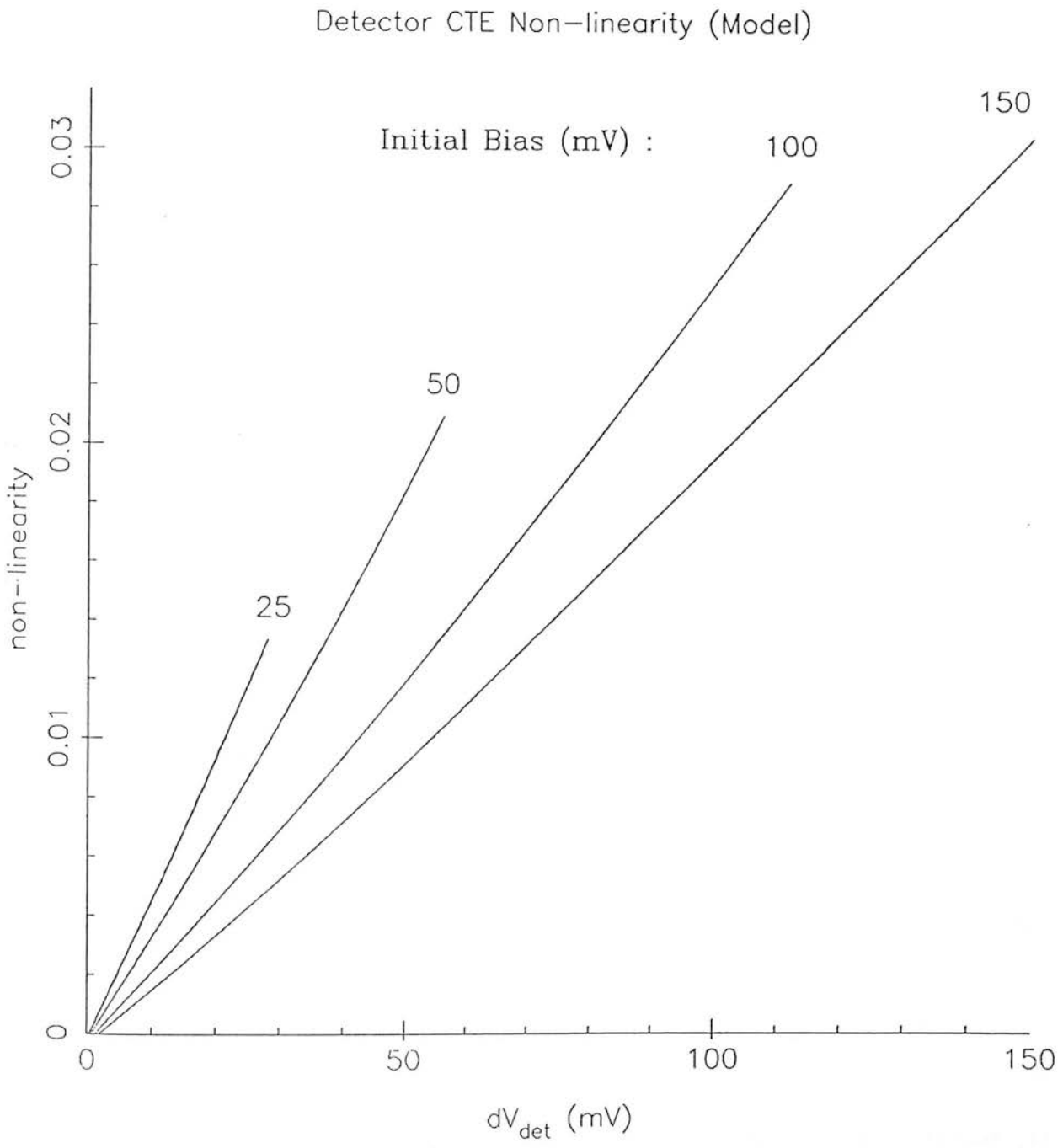

Figure 3.11
The detector CTE non-linearity (derived using CE capacitance data and equation 3.8).

Bias	Initial CTE (pF^{-1})
25	0.038
50	0.040
100	0.042
150	0.044

The VTE variation, however, is much larger. In effect the non-linearities predicted by eqns. (3.4) and (3.5), when combined in (3.8), have to some extent cancelled to give a fairly linear detector response to radiation. These results are independent of the reference pedestal used.

If there are capacitance variations from pixel to pixel then V_i' will not equal V_i, and there will be an additional term in the square brackets of eqn. (3.5);

$$V_i \frac{C_d(V_s)}{C_d(V_f)} \left[1 - \frac{V_i'}{V_i} \right] \approx V_i \frac{C_d(V_s)}{C_d(V_f)} \cdot \frac{\Delta C}{C_d'(V_i') + C_t} \qquad (V_{ext}=0)$$

ΔC represents the average pixel to pixel capacitance difference, and $C_d'(V_i')$ is the detector capacitance which gave rise to the pedestal V_i'. For $\Delta C/C \approx 0.01$ (see chapter 5), and a detector left to saturate from V_i=-60mV, the two terms in square brackets in eqn (3.5) are 60mV and -3.8mV respectively, and the above term gives a contribution of -0.3mV, in which case its effect can be neglected.

In practice, even after fine tuning, the odd/even effect on V_i and V_i' tends to dominate the capacitance variation. This will introduce a d.c. error term which will be a weak function of bias and readout point, and will not have a significant effect on the results summarised in figures 3.10 and 3.11.

Though the results presented are specific to the CE array, the method of invoking charge conservation to derive the signal response can easily be applied to other readout configurations. This was done for an SBRC InSb DRO array.

The calculation in this case is simplified since the detector is permanently connected to the output line, as represented in the unit-cell of figure 2.5, so that equation 3.4 can be applied directly. The total capacitance is the sum of all stray capacitances and the bias dependent junction capacitance, which can be found from equation 3.1.

Using typical operating values, supplied by the manufacturer,

response and non-linearity curves were derived (figure 3.12). The non-linearity in this case could be improved by making C_j a small proportion of the overall parallel combination.

3.4 Signal Extraction and Noise Sources

As outlined in the last section, the detector characteristics and readout sequence do not allow a direct measurement of a signal level (by the differencing of two suitably located samples) which is linearly proportional to the integrated input.

From the video output, the most likely reference points for the signal of pixel m are;

(i) Pedestal of pixel m, readout n-1

(ii) Pedestal of pixel m-1, readout n

(iii) Pedestal of pixel m, readout n

(i) accurately represents the initial state of the detector, but is separated from the signal by the integration time and is therefore susceptible to 1/f noise. (iii) also represents the initial state but will differ from (i) due to reset noise. Although (ii) refers to a different pixel, when referenced to the signal, it relates directly to the charge change on the video line caused by the charge change on pixel m, and in this respect may have a stronger correlation to the signal level than (i) or (iii). The problem of signal referencing will be discussed further in chapter 5.

There is another source of non-linearity in the signal response, due to dark current. Since the detector dark current is a function of bias, during an integration the total dark current contribution will depend not only on V_i and V_f, but also on the rate at which the detector is discharged ie. on the level of illumination. A 'dark' frame (no illumination) will have a larger contribution than a strongly illuminated exposure when the integration times are equal. Models to correct for this effect will be discussed in chapter 6 in connection with experimental results.

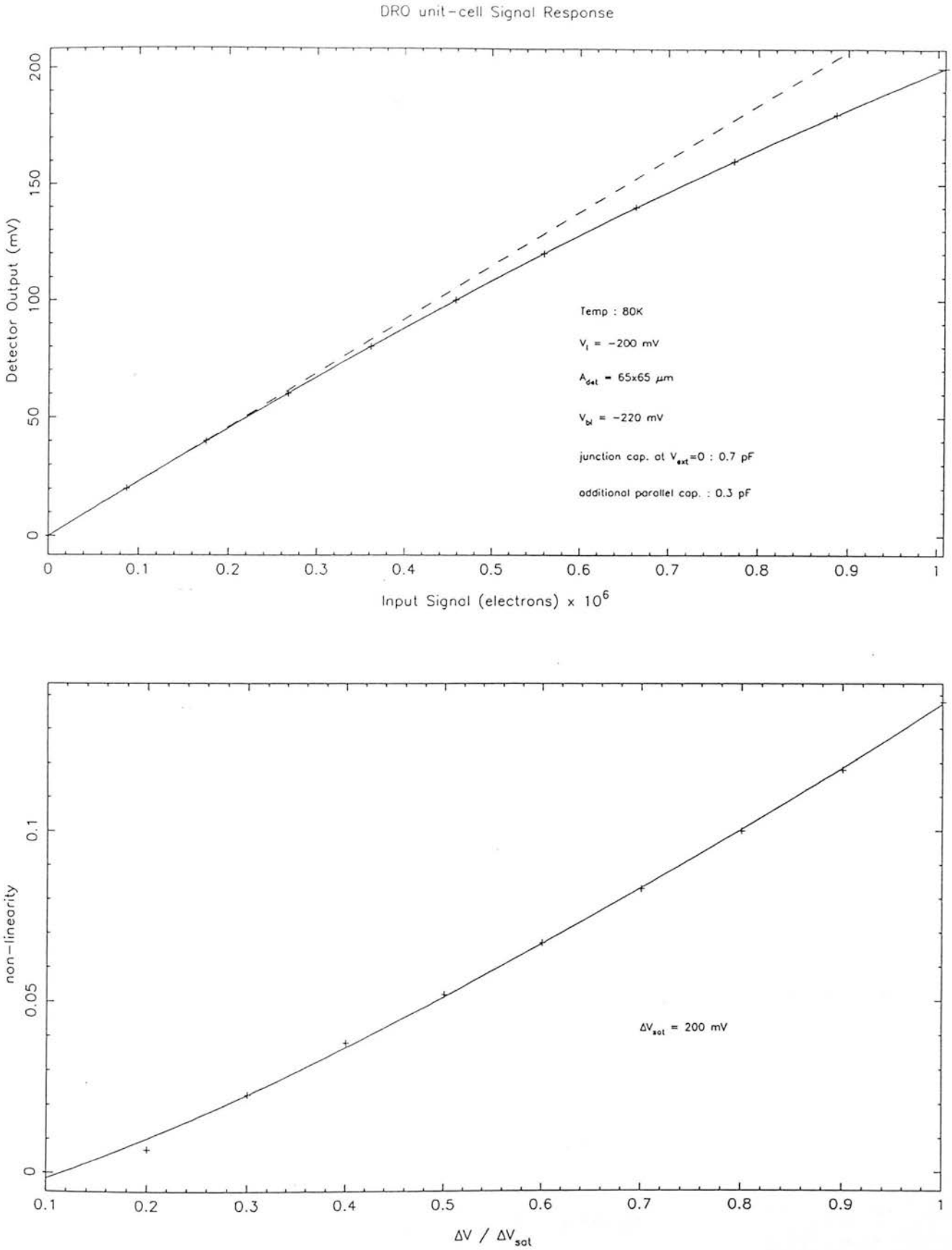

Figure 3.12
Predicted response (a) and non-linearity (b) of SBRC DRO detector array.

Once the signal has been corrected for the effects of charge transfer non-linearity and dark current, the sensitivity will be determined by the dominant source of noise. For the detector array the main sources are;

(i) Shot noise of the incident radiation

(ii) Shot noise on the dark current

(iii) kTC reset noise

(iv) JFET preamplifier noise

(v) 1/f noise

Another potential source is pick-up on the input and output lines. In particular, noise on the bias line will be coupled directly onto the detector during the reset phase. Pick-up can be minimized by shielding the device, and by the use of RC filters.

Components of kTC noise are introduced due to the switching nature of the device. Initially, closing the reset switch, followed by opening the multiplexer switch, will give an uncertainty in the initial bias. Secondly, there will be an uncertainty in the video line charge, due to the multiplexer switch of pixel m-1 opening immediately before readout, and thirdly, an uncertainty in the signal level itself, due to the Johnson noise of the multiplexer 'on' resistance, modulated by the RC time constant of the multiplexer switch and the capacitances, C_d and C_t.

Davis and Niblack (Davis, 1986) have derived the overall kTC contribution for the readout scheme described. They find a figure for the rms noise at the detector of;

$$N_{ktc} = \frac{1}{q}\sqrt{(kTC_N)} \approx 1600 \text{ electrons at } 50 \text{ K}$$

$$C_N = \frac{C_d}{C_t}(C_d+C_t) + C_d + \frac{1}{C_t}(C_d+C_t)^2 \approx 90 \text{ pF}$$

Finger et al. (Finger, 1987) have used the technique of correlated double sampling to remove the video line kTC contribution, by sampling the video line with all the multiplexer switches open (so that RC ≈ 200

seconds), and then referring this level to the signal portion. They report a net kTC rms noise of 1000 electrons using the same device at 50K.

The bandwidth of the external electronics is such that the JFET noise is small compared to the kTC contribution, and it is the latter that determines the limiting readout noise.

Finally, in order to give a rough idea of the magnitude of the output signals involved, one thousand integrated charges (the approximate minimum rms readout noise of this device) will give a voltage change at the JFET output of 6 μV. In order not to add further noise to this low level signal, careful design of the signal processing circuitry is required.

CHAPTER FOUR

INVESTIGATION OF THE 32 ELEMENT ARRAY I

Introduction

The purpose of this chapter is to give a brief description of the experimental set up used for assessing the performance of the detector array. In designing a system to run the array, and process the signal output, the main overall aims were;

(i) Achieve a readout noise level as close as possible to the kTC limit of the detector, so that the noise could be analysed under different operating conditions.

(ii) Allow a wide range of integration times, and the ability to repeat readouts in order to improve the signal statistics. For these reasons, fast data processing is required.

(iii) Allow comparison of different sampling configurations

(iv) Illuminate selected detectors with controllable flux levels.

(v) Vary the wavelength of incident radiation between one and five microns in order to measure the relative quantum efficiency.

(vi) Allow a variety of detector operating temperatures.

(vii) And a range of initial detector biases.

(viii) Maximise the dynamic range of the data acquisition system to allow noise and large signals to be observed simultaneously.

The majority of these aims were achieved, though there was not time to incorporate (v) into the design.

An outline of the final, complete system is shown in figure 4.1. In the description that follows the detector end will be dealt with initially, and from there the signal path will be followed 'downstream', finishing with details of the control software.

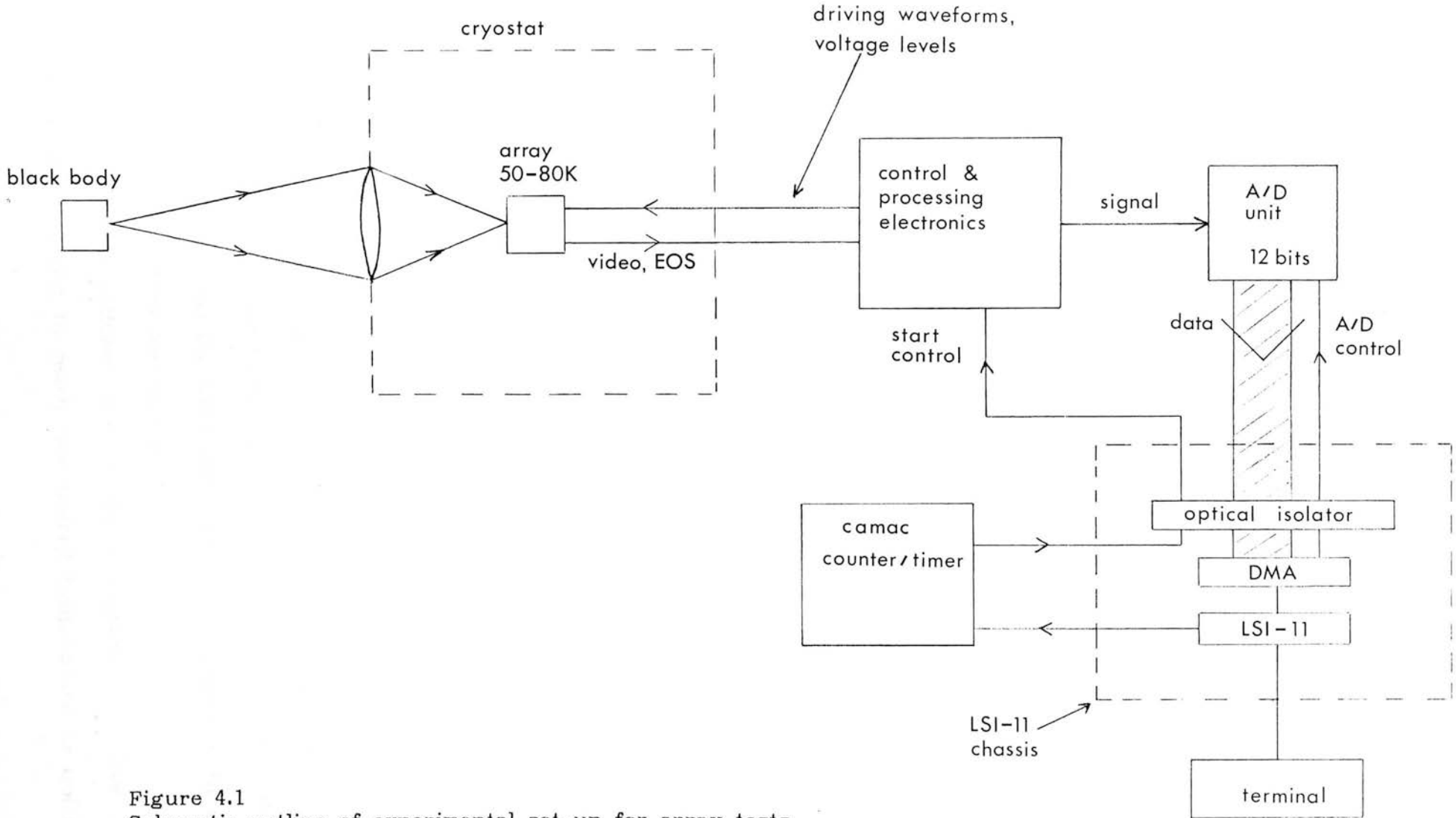

Figure 4.1
Schematic outline of experimental set-up for array tests.

4.1 The Detector Mounting

4.1.1 Cryogenics

As already discussed, in a BLIP system the overall sensitivity can be improved by reducing the background level. In an astronomical spectrometer, the detector has a field of view (FOV) on the sky determined by the external optics, through which it 'sees' background from the sky and the warm, low emissivity, optical surfaces such as the telescope primary. As well as this, radiation will reach the detector from its immediate surroundings. It is for this reason that the detector enclosure is cooled to a level where the sky plus telescope background dominates. An 80K enclosure is normally adequate.

In addition, the detector itself must be cooled to reduce the dark current. This will enable long integration times, which will improve the detector sensitivity at low backgrounds (where S/N is directly proportional to the integration time), and at high backgrounds large storage capacities (ie. large initial biases) can be employed to achieve BLIP.

Since the same principles apply to the array testing apparatus, a two vessel cryostat was used. The outer vessel is filled with liquid nitrogen (LN_2), which cools a cold shield surrounding the detector and inner vessel. The inner vessel, which cools the detector array and its mounting, can be filled with LN_2 or liquid helium (LHe). If the vapour pressure of the cryogen is reduced (by the use of a rotary pump attached to the fill tube), its boiling point will drop. Nitrogen will solidify when the triple point is reached at 63.1 K, and further reduction in the pressure leads to another temperature drop, as the solid loses heat via sublimation. In this way the detector temperature can be varied.

In order to ensure efficient use of the cryogens, and allow the components in the cryostat to reach the desired temperature as quickly

as possible, a number of precautions are necessary.

The time which these components will remain cold for is determined by the hold time, which is the time taken by the outer vessel to empty, since this is where the major heat loading occurs.

Heat can reach the outer via radiation, convection and conduction.

Net radiation flow from warm to cold surfaces can be minimised by lining the inside surfaces with highly reflecting materials such as aluminised mylar.

Improving the vacuum by preventing leaks, keeping out materials with a tendency to outgas, and using an adsorption pump or 'getter' attached to the cold face of the inner vessel, will help to reduce the convective and conductive heat flow.

Conduction occurs down the fill tubes and along the wiring connecting the detector to the outside world. The latter effect can be reduced by using long, small cross-section, low thermal conduction wire such as constantan, though the electrical resistance must not be too large, as currents may cause undesirable heating.

Good thermal links to the cold face are essential if rapid cool down times and low component temperatures are required.

For the cryostat used, typical hold times using LN_2 were twenty hours. For a 2.5 litre capacity outer vessel, this corresponds to a heat input of six Watts.

In practice, using only LN_2, the cool down time was about five hours, and the equilibrium detector temperature (when running) was 80 K.

The array assembly was mounted on a copper block held off the 80K surface by two fibre glass pillars. The mounting arrangement was constructed to allow a certain freedom of movement in the position of the aluminium base (see figure 4.2) and the copper block, which could slide along the pillars. In this way the detector could be positioned at the focus of the CaF_2 window lens, and allowances made for the contraction

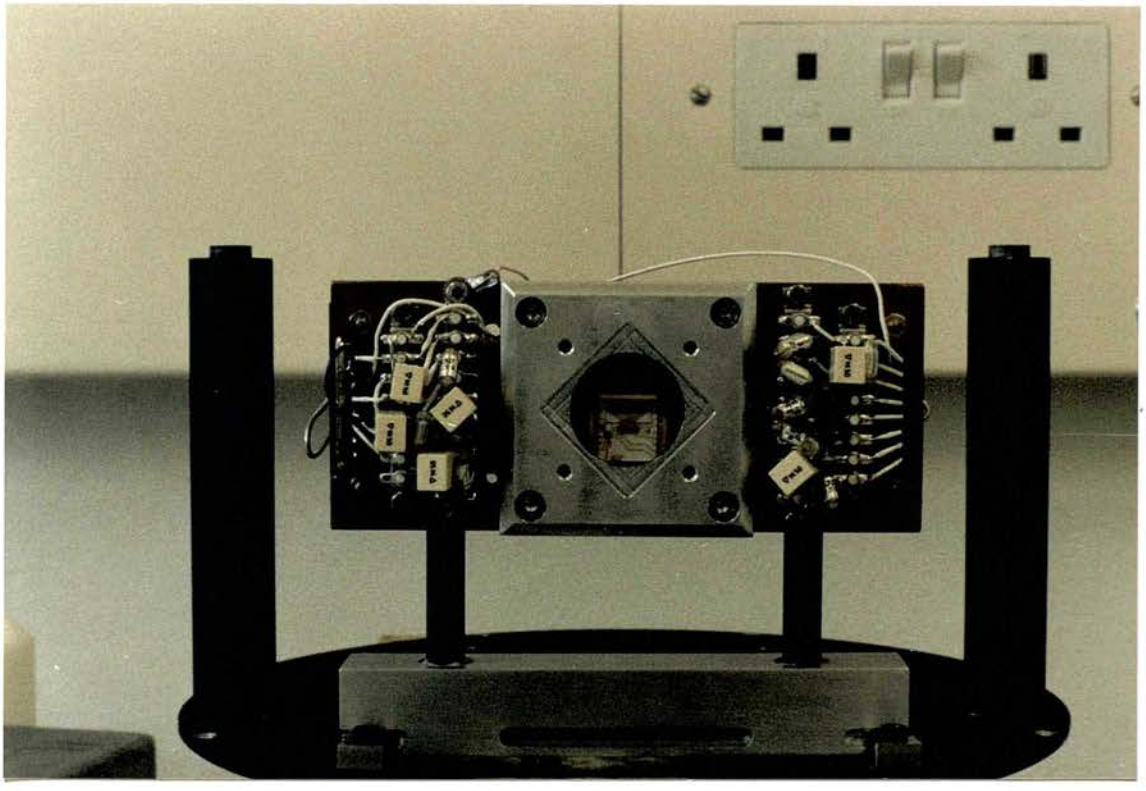

Figure 4.2
Detector mounting showing components and array cold-shield.

of the cryostat's copper support structure on cooling (this was calculated to be ≈ 1 mm in going from 300 K to 80 K).

The copper block was cooled via a short flexible link, made up of several strips of copper soldered together at either end, which was attached via a copper 'finger' to the cold face. The temperature was monitored by a Lake Shore Cryotronics DT500 silicon diode temperature sensor, which screwed into the rear surface of the block.

The array itself was surrounded by an aluminium cold shield bolted to the copper block, whose purpose was to restrict the FOV of the detectors, and onto this was fixed a cold aperture, with a slit running parallel to the array, and a 2.2μm K-filter. This geometry meant that the central pixel had an approximate FOV of 34 ° by 80 °.

For dark current measurements the slit was covered with aluminium foil, as was the entrance hole of the cold shield.

4.1.2 Electrical Considerations

To reduce noise pick-up at the detectors, each of the lines was filtered to attenuate high and low frequencies in the d.c. supplies and high frequencies in the clocking waveforms, by using RC combinations mounted close to the detector. In addition, a 1 MΩ resistor was placed between the reset gate and ground, to reduce the possibility of static discharge damaging the high impedance MOSFET input, and a potential divider (÷20) was placed on the bias line to attenuate input noise (after suggestions from Dr Gerd Finger).

Polystyrene and polyester capacitors were used for the filters, and when tested at 80 K, were found to drop by between five and ten percent of the room temperature value. The corresponding change in the resistors was less than one percent.

The analogue (ie. voltage levels, bias and video) and digital (Φ_1/Φ_2, EOS etc.) lines were kept apart to reduce mutual interference, and this

was continued out to the control electronics where there were separate analogue and digital boards.

To allow more control over the grounding, and in order to use the cryostat as a Faraday cage, the detector mounting was electrically isolated by inserting an alumina (Al_2O_3) washer between the thermal link and the cold finger. This material allows reasonable thermal conduction.

The general grounding scheme around the detector is summarised in figure 4.3, which includes the other components of the system.

4.2 Control Electronics

4.2.1 Description

After the detector had been supplied, CE also provided two control boxes to operate the array and provide a means of digitizing the signal.

The first box (IME-200) consisted of two boards; one, digital, providing the driving waveforms and allowing their levels to be varied, ie. for fine tuning of the clocks to reduce the odd/even difference, the other, analogue, containing the signal processing circuit. This circuit is shown in figure 4.4, and is described below;

The clamping amplifier operates in the following manner;

With the analogue switch closed (clamp command low), the capacitor C_c charges up to the post amplifier output voltage in a short time of the order of R_cC_c ($2\mu S$), and the output of the clamp amplifier at this time represents the ground level. When the analogue switch opens, the charge remains on C_c for a large time, $R_{in}C_c$ ($R_{in}=10^{12}\ \Omega$). Since the voltage drop across C_c is the same in both states (once charged), any change at the input will appear at the clamp output referenced to the voltage level present when the signal was clamped, as outlined in figure 4.5a.

By synchronizing the operation of the analogue switch to various parts of the video waveform, it is possible to perform analogue differencing of, for example, the pedestal and signal levels. The

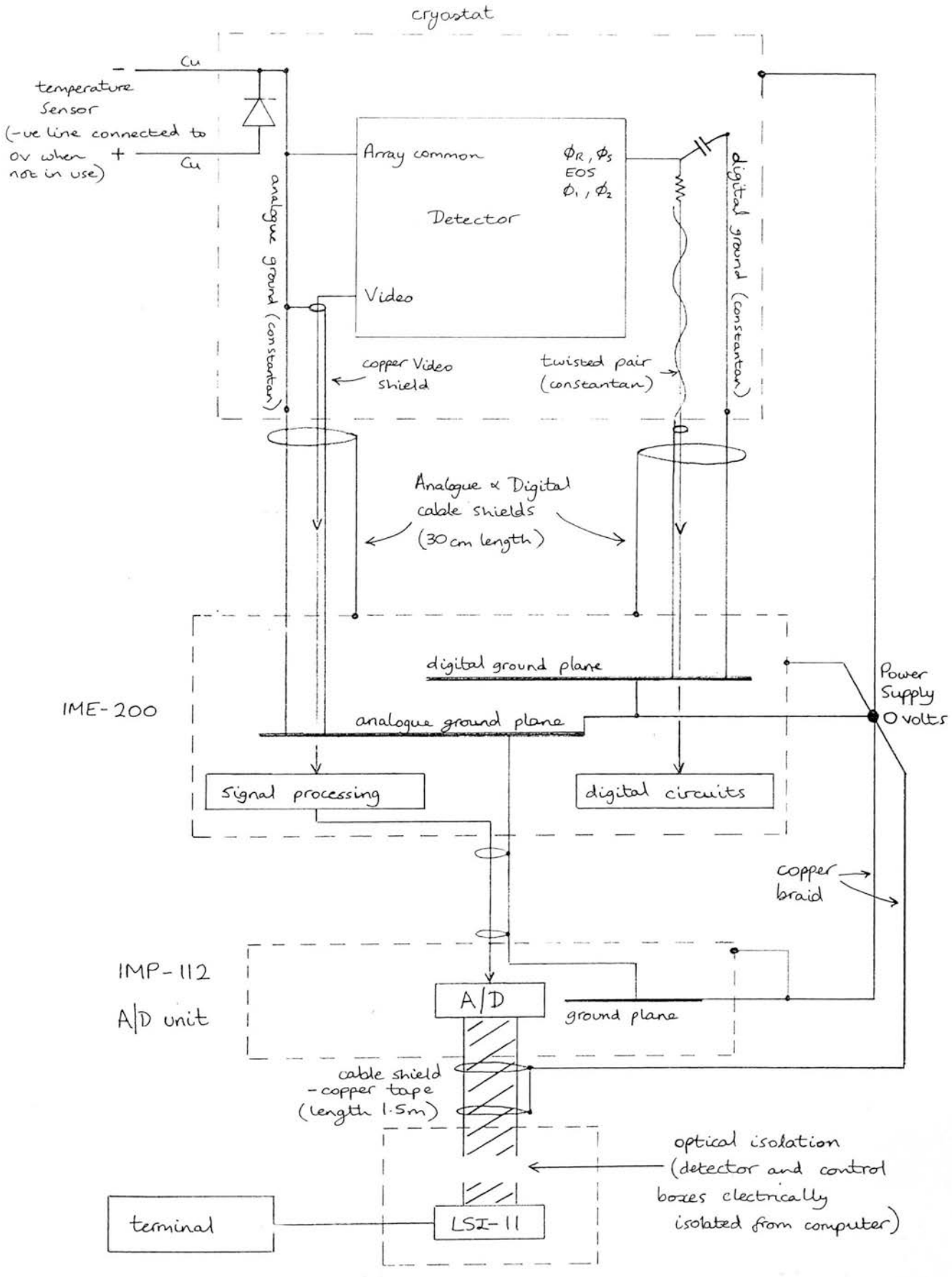

Figure 4.3 : Grounding scheme.

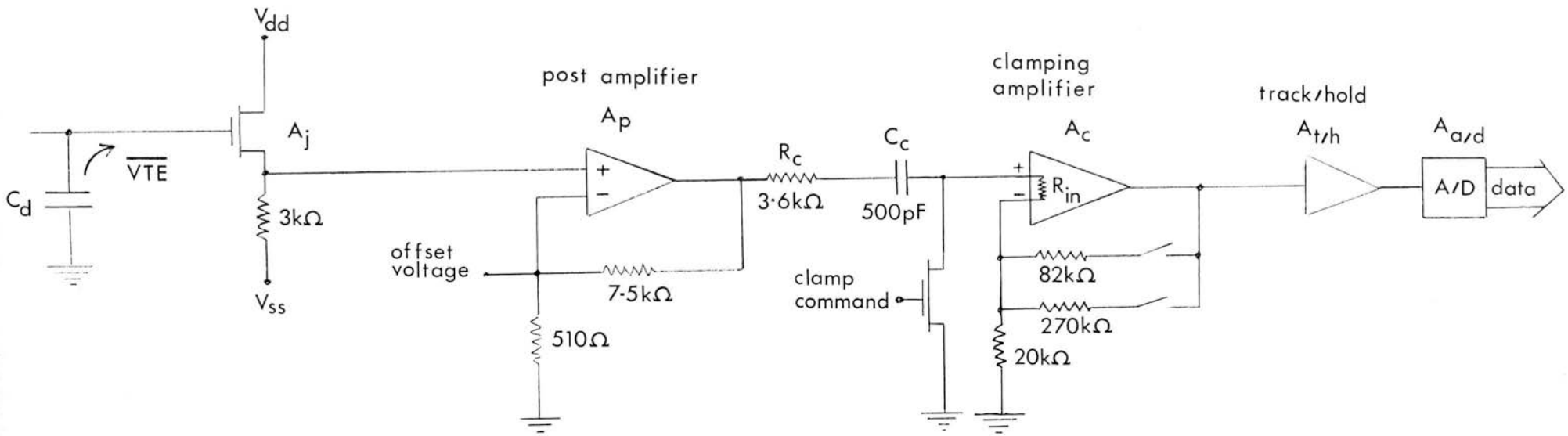

measured gains

A_j	0·94 at 80K
A_p	15·8
A_c	4·17, 5·12, 14·7
$A_{t/h}$	−1
$A_{a/d}$	$(1{\cdot}223\ mV/dn)^{-1}$

Figure 4.4 : Signal path.

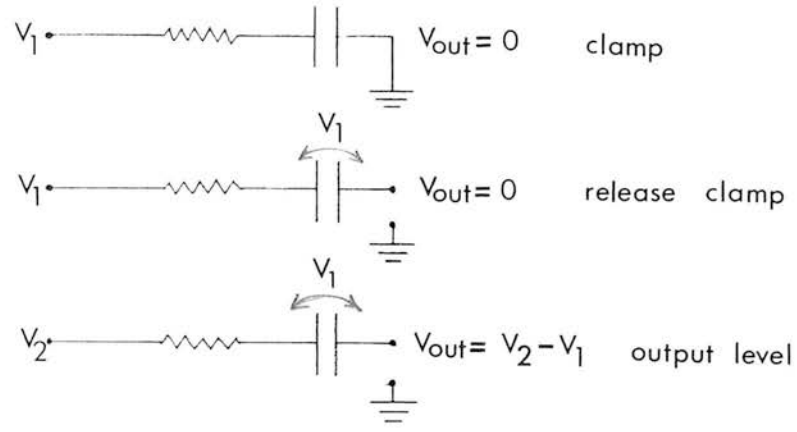

a.

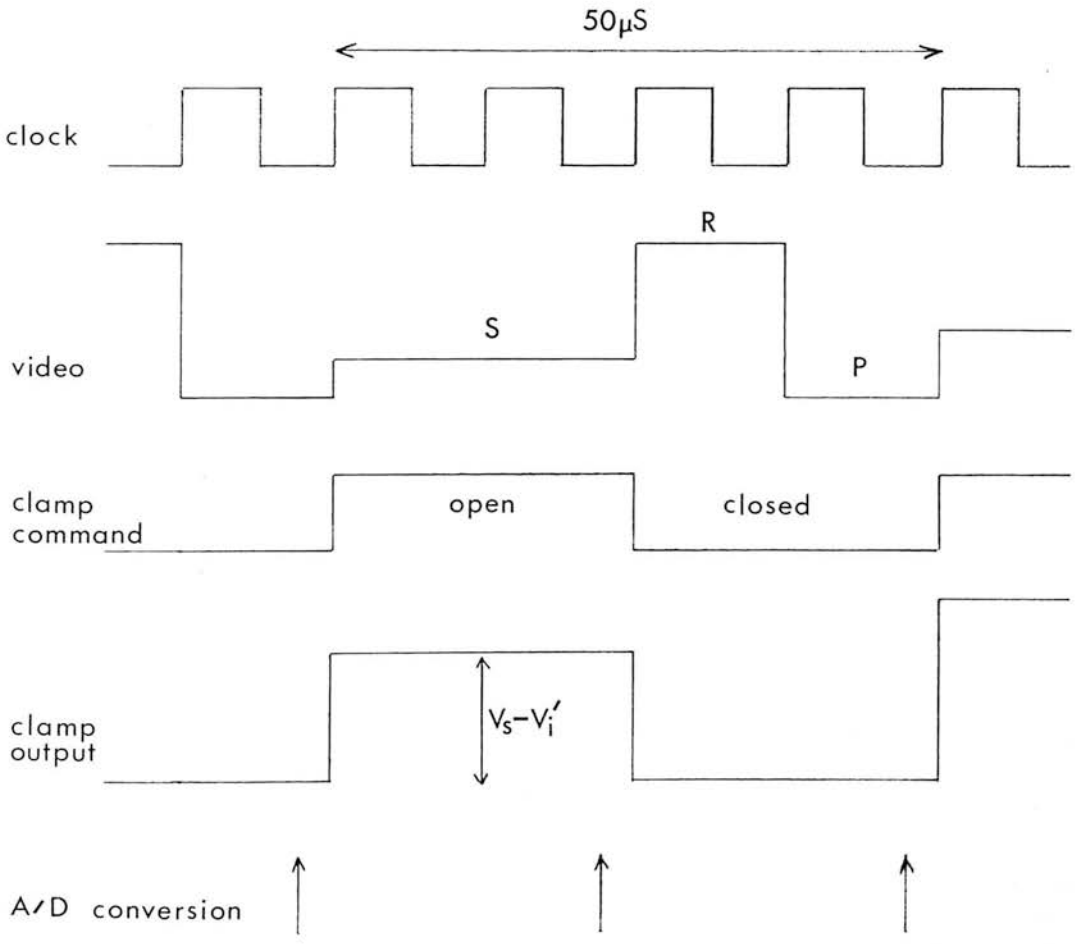

b.

Figure 4.5
Operation of clamp amplifier; (a) Equivalent circuit, (b) Timing diagram.

arrangement that was used is shown in figure 4.5b and gives a relatively simple output of two levels, signal (by differencing the signal and preceeding pedestal portions) and ground. Also shown are the encode waveforms used for triggering the A/D unit.

The main advantage of using the clamp amplifier is that it forces a high sampling frequency on the video signal, which rejects low frequency voltage variations such as the 1/f noise contribution of the post amplifier, though this could also be achieved by sampling the relevant levels with the A/D unit and differencing them.

The gain of the clamp could be switched between three values (figure 4.4) to allow noise observations to be made at high resolution, and signal measurements up to saturation, for reasonable biases.

For some tests the raw video was digitized by tapping the output of the post amplifier.

The second box (IMP-112) contained a 12 bit, successive approximation, Analog-to-Digital (A/D) converter with a conversion time of 4 μS, which was triggered by the encode pulses. A delay was imposed on the A/D trigger to allow the voltage level to settle, and, during conversion, was held constant by a track-and-hold amplifier.

Synchronization with the readout sequence was achieved by triggering on the Start and EOS pulses.

The IMP-112 has a 37 pin D-type connecter which gives access to the twelve data channels and a Data Ready output, which indicates when an A/D conversion is ready for transmission. A Data Request input, when set high by an external device, will allow data acquisition.

4.2.2 System Gains

The gains at each stage of the signal path are shown in figure 4.4 and the total system gain, A_S, is given by;

$$A_S = \overline{VTE}.A_j.A_p.A_c.A_{T/H}.A_{A/D} \qquad \text{dn mV}^{-1}$$

By switching in different feedback resistors, three system gains could be selected, which for convenience were referred to as; very low (VL), low (L) and high (H). The reason for this arrangement was to match the dynamic range of the detector, as represented by the ratio of the storage capacity to the readout noise level (a value of 2000 was achieved experimentally for an initial bias of -60 mV), to that of the A/D unit. When the clamp output, which is effectively unipolar, was sampled, the useable range of the A/D (bipolar input) was reduced to 2^{11} levels. Hence, in order to easily resolve the readout noise of the detector, the above aim could not be realised, except by the use of a variable signal gain.

Instead of using A_s, a more useful figure to describe the signal path is the conversion factor, C_e, representing the charge change (in electrons) at the detector, Δn, which will give rise to a signal change, ΔS, at the output, of one data number (1 dn).

Firstly, in terms of ΔV_d;

$$\Delta n = \left[\frac{1}{V_f - V_i} \int_{V_i}^{V_f} \frac{dN_e(V_d)}{dV_d} \, dV_d \right] \Delta V_d$$

The term in brackets was measured (using figure 3.5) to be $\approx$ 83 el/μV, for detector voltages in the range zero to -125 mV.

Therefore;

$\Delta n = - [10^3 . (83 \text{ el}/\mu\text{V}) . A_s^{-1}] \Delta S = C_e . \Delta S$

The conversion factor can thus have the following values;

VL gain	3300	el dn^{-1}
L ,,	2700	,,
H ,,	900	,,

These figures are only accurate to about +/- 10%, due to the uncertainty in the zero-point detector capacitance, and the fact that C_d

and A_j vary with temperature, but are a useful guide for measuring detector noise (H gain) and signal levels (VL gain) in terms of electrons.

4.2.3 System Linearity

Since one of the aims of the investigation is to analyse the intrinsic signal response of the array, it is important to measure the linearity of the signal processing electronics after the JFET (the JFET is operated over a small range of ≈50 mV, and can be assumed to be linear). This was done in the following way;

Firstly, the A/D unit (IMP-112) was tested by taking a large number of samples of the output for a given input voltage. This was then repeated over the complete output range of +/- 2.5 V. From these measurements the conversion factor of the A/D was found to be 1.223 mV/dn with an rms error, from least squares fitting, of 10^{-4} mV/dn (0.01 %).

The post amplifier also exhibited excellent linearity when the output (connected straight to the A/D input) was varied over the range of the A/D. The rms error in terms of the gradient of response (or gain) was found to be ≈ 0.05 % over this range.

Due to the modulation of the clamp, its response was measured by using a signal generator to produce a small amplitude square wave (of the same frequency and phase as the clamp command pulse), which was passed through a d.c. attenuator and then into the post amplifier. For each setting of the attenuator, the amplitudes of the clamp input and output were digitized. The percentage error in the gain in the two cases (ie. ground to +ve voltage and ground to -ve) was found to be 0.1% rms.

4.2.4 System Noise

As already mentioned, the system gains were chosen so that some noise analysis could be performed on the array output. For this to be the limiting noise source of the whole system requires a lower noise

contribution from the amplifier circuits and the A/D converter.

For a noise free, d.c. level at the A/D input, the output uncertainty (or digitization error) is +/- 1/2 dn, but if the input peak-to-peak noise is greater than a few dn, then it can be shown (Connor, 1973, pp79-80) that the digitization error falls to $1/\sqrt{12} \approx 0.3$ dn rms.

By shorting the input to the post amplifier, and taking many samples of the A/D output, the noise from the amplifiers could not be resolved above the digitization noise (H gain), and was therefore $\leqslant$ 500 electrons rms at the detector.

The smallest conversion factor was thus chosen so that an optimistic detector readout noise could be well resolved by the A/D converter.

4.3 Data Acquisition System

4.3.1 Hardware

Data from the A/D converter was transmitted to an LSI-11 computer, where all the lines (input and output) passed through an optical isolator unit (so that there was no common wiring between the computer and the rest of the system, in order to reduce interference from computer clocks etc.), and into a Direct Memory Access unit (DMA). Once programmed, this unit accepted a string of data, in phase with the Data Ready pulse, at a maximum rate of 250 kHZ for 16 bit words and stored it directly in memory, from where it could be retrieved and processed after a run had finished. This configuration allowed rapid readout rates.

An array readout could be initiated in one of two ways; in the IME-200 box itself, using a pulse counting circuit running on the fundamental clock to generate a Start pulse, or externally, in a similar manner, using a computer controlled counter/timer unit.

The advantages of using the external restart were that the clock frequency running the counter could be varied (or an internal 1 MHZ clock used), and the maximum pulse count which could be programmed

was 2^{24}, thereby giving a large range of selectable integration times.

4.3.2 Software

The processes of taking data and, if desired, of dictating the integration time, were controlled by an LSI-11 processor. Two programs were written to meet these ends; a Fortran program consisting of subroutines which provided the working environment, and a faster program, written in a form of assembler language (Macro), which controlled the operation of the DMA and arranged the cumulative storage of data for a pre-selected number of readouts of the array.

To illustrate the tasks performed by the software (in terms of the set-up in figure 4.1), a typical sequence of operations within the Fortran control program, in order to take data and process it, might be;

(i) Set up the parameters necessary for taking data. This involves selecting whether or not the readout rate is to be controlled by the computer, the pixel frequency (determines minimum t_i), the running frequency of the Camac counter/timer (determines maximum t_i), the integration time, and the number of readouts to be coadded. Different ways of referencing the signal (sample modes) can be selected (ie. referencing a level to either the preceeding or following level or taking the absolute level itself, unreferenced). Selected pixels can be excluded from the statistical analysis of the results, and a pixel can be used to produce a histogram of the signal.

(ii) Begin a data-taking run. Control is passed to the Macro routines, which set-up and start the counter/timer for integration control, prime the DMA unit, and then begin taking data by setting the Data Request line. For the selected number of readouts, the data is checked for overflows (and if necessary, an error flag set), the cumulative total and sum of squares is stored, and when a run has finished, control is returned to the Fortran program.

(iii) Analyse results of last run. Various statistics are returned, such as; Mean signal, standard deviation (or rms error), σ, and mean error, σ_m, for each detector, an average signal and noise over a range of pixels, the odd/even difference, and a signal histogram (which is useful for checking that the A/D is operating properly). The results can also be sent to an output file (an example of which is shown in figure 4.6).

There were also a number of routines available for specific experiments;

(i) A routine to calculate the cross-correlation between two selected levels.

(ii) A routine to take data from a single pixel, and display the noise of each level used to derive the signal output, as well as the noise on the signal level itself (useful for comparing the effectiveness of different sampling modes). A histogram of the latter noise measurement was generated, and this was used to investigate the relationship between output noise and illumination level.

(iii) A routine which could be set up with the number of readouts to be taken at a single t_i, and a range of integration times to be performed. When run, an output file containing the variation of signal with integration time was generated. This was used for a major part of the illumination experiments, and was especially useful for measuring the dark current response at low temperatures, where the integration times were large ($\approx$ 90 S), as the apparatus could be left running, unattended, for several hours.

4.4 Optics

The simple optical arrangement used to illuminate the detector array is shown in figure 4.7. This arrangement was chosen in preference to one which involved a collimated beam from the black body source (with spot scanning achieved by rotating a mirror in this beam), due to alignment

```
SATURATION LEVELS
81K,0V EXT
 Integration time              :    200.00 M
 Number of readouts            :   500
 Chopping                      :  F
 Mode                          :  3
 Pixel frequency ( khz )       :    20.000
 Clock frequency ( khz )       :  1000.000
```

Pixel	mean signal (dn)	error in mean, σ_M	rms error σ_{n-1}	exclude flag	A/D data overflow flag
1	0.000	0.000	0.000	1	0
2	1412.238	0.050	1.115	0	0
3	1376.932	0.053	1.191	0	0
4	1398.636	0.059	1.317	0	0
5	1384.816	0.052	1.168	0	0
6	1396.668	0.050	1.110	0	0
7	1382.764	0.050	1.118	0	0
8	1402.696	0.053	1.188	0	0
9	1385.144	0.057	1.277	0	0
10	1388.276	0.055	1.221	0	0
11	1373.972	0.056	1.258	0	0
12	1399.402	0.063	1.403	0	0
13	1387.846	0.060	1.347	0	0
14	1402.524	0.058	1.307	0	0
15	1386.842	0.060	1.339	0	0
16	1399.422	0.071	1.578	0	0
17	1378.332	0.069	1.551	0	0
18	1395.228	0.071	1.579	0	0
19	1376.502	0.063	1.415	0	0
20	1400.738	0.074	1.663	0	0
21	1378.460	0.067	1.490	0	0
22	1403.156	0.066	1.482	0	0
23	1378.216	0.071	1.594	0	0
24	1404.292	0.072	1.621	0	0
25	1383.394	0.072	1.615	0	0
26	1408.004	0.074	1.648	0	0
27 ← Hot pixel	1310.900	0.090	2.005	0	1
28	1397.044	0.075	1.685	0	0
29	1381.264	0.075	1.678	0	0
30	1406.560	0.074	1.646	0	0
31	1394.994	0.077	1.729	0	0
32	1210.868	0.071	1.594	0	1

```
 Mean over 29 pixels     =  1391.875 +/-   0.064
 Average standard deviation =   1.425
 system noise ( electrons ) =     3991. @ 2800.el/dn
 rms noise ( % )            =   0.102
 range ( % )                =   2.749
 odd/even difference        =   17.385
 odd/even effect ( % )      =   1.249
```

Figure 4.6 : Typical results printout

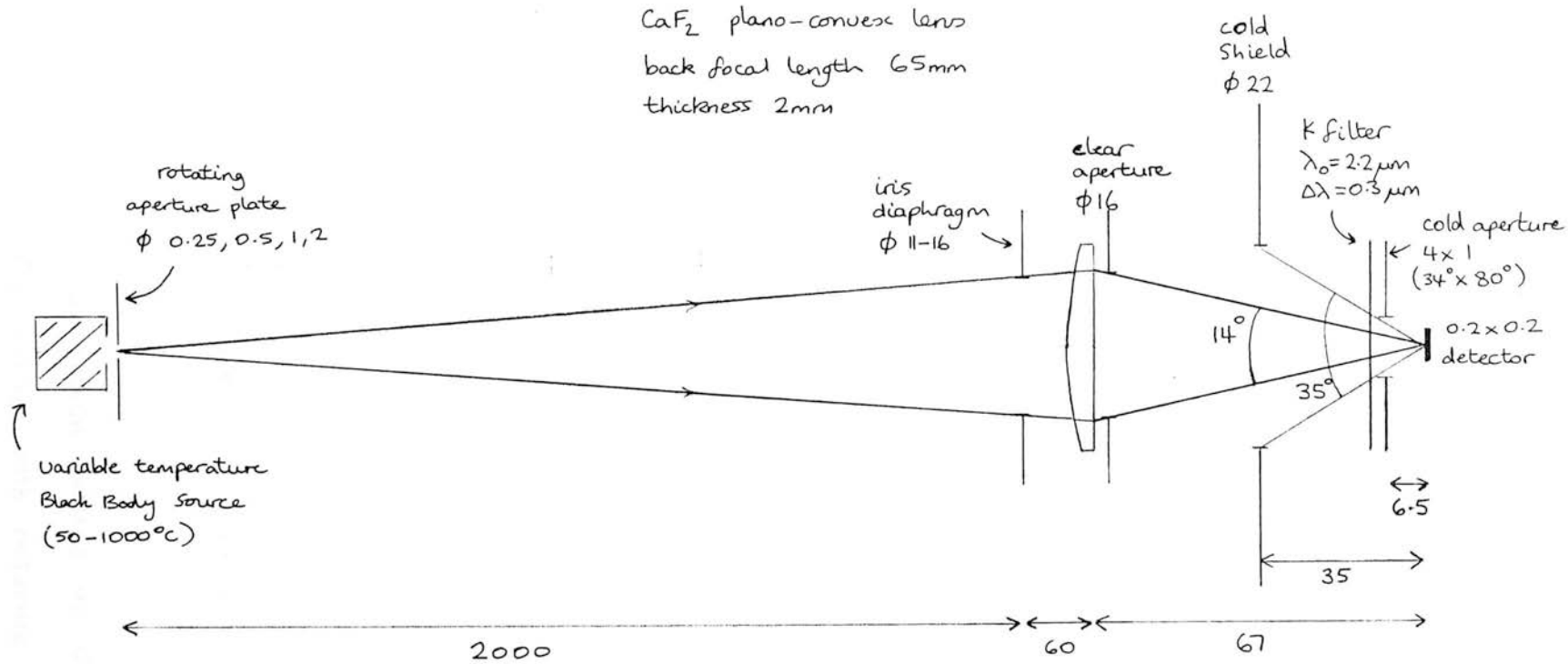

Figure 4.7
Optical arrangement for detector illumination (not to scale). All dimensions are in millimetres.

difficulties.

In the adopted set up, an aperture at the black body (normally at 350 ° C) was imaged on a detector and was scanned by moving the black body itself. The available apertures gave spot sizes of between 8 and 64 μm, assuming an aberration free system. The diffraction limited spot size of the lens, however, was 10 μm at a wavelength of 2.2 μm.

The radiance of a black body is given by the Planck radiation law;

$$L_\lambda(T) = \frac{2hc^2}{\lambda^5} \left\{ e^{hc/\lambda kT} - 1 \right\}^{-1} \quad W\ m^{-3}\ sterad^{-1}$$

Applying conservation of radiance, the photon flux detected, N, from background at temperature, T, and of emissivity, ϵ, is therefore;

$$N = \epsilon . qe . A_d . \Omega_d \int_{\Delta\lambda} \left\{ \frac{\lambda}{hc} \right\} L_\lambda(T)\, d\lambda \qquad \text{detections } s^{-1}$$

A_d is the area of a single detector

Ω_d is the detector FOV

$\Delta\lambda$ is the wavelength range over which radiation is detected

An upper limit estimate of the photon flux from a 300 K background, seen through the K filter and cold shield aperture is,

$N = 4 \times 10^7$ (ϵ=1,qe=1),

which, with an initial bias of -60 mV, will saturate the detectors in about 100 mS. Since the minimum integration time is 2.2mS, this does not restrict the array operation.

The flux from the cold enclosure (T $\approx$ 85 K) is negligible.

4.5 Conclusion

A major part of the time spent setting up the system outlined (figures 4.1 and 4.3) was concerned with reducing the readout noise, which initially was very large.

The primary factors in achieving a noise level of 2300 electrons rms

(section 5.2) were, housing the LSI-11 in a metal chassis to reduce radiative interference, and using the grounding arrangement between the detector and post amplifier shown in figure 4.3.

Of secondary importance were the use of filters at the detector, opto-isolating the computer from the rest of the system, and the general grounding scheme used between the system components to reduce ground-loop interference. The contribution of each of these modifications to the overall reduction in noise was difficult to judge, since it was not feasible to implement a single change at each stage of the set up, and then check for an improvement.

CHAPTER FIVE

INVESTIGATION OF THE 32 ELEMENT ARRAY II - EXPERIMENTAL RESULTS

Introduction

The results of tests carried out on the CE array are presented in the following two chapters.

The overall aim of the investigation was, firstly, to understand in detail the behaviour of the InSb photo-diodes and, secondly, address the aspects contributing to the performance of an integrating infrared detector in an astronomical instrument; efficiency, dynamic range, stability, response linearity and the sensitivity limiting source of noise.

The most difficult area to investigate is the noise performance under a variety of operating conditions. The reason for this is that it is sometimes difficult to isolate where noise is being introduced into a system, and, once found, it is another matter to identify the source of this interference. The amount of time spent, in setting up the test apparatus, providing electrical shielding and effective grounding reflects this difficulty. Adding to this situation is the number of operating variables involved (temperature, bias, integration time, illumination level, detector voltage levels), each of which may give rise to spurious noise.

The question of detector quantum efficiency, though important, was not addressed in any experiments, the reason being, that to make accurate measurements requires accurate radiometric calibration, which would have required a large amount of effort in the optical design. Also, InSb has been well studied as regards this property (eg. Bailey, 1982), and the figure of 0.8 already quoted is consistent with these results.

Of particular concern with this device, and indeed all infrared p-n junction integrating detectors, is the linearity of its response to radiation, and how this response is affected by the presence of dark

current. Linearity is of major importance in astronomy where an object's brightness is derived, after a process of background subtraction and flat-fielding, by calibrating against a source which may have a different spectral distribution and intensity. For this reason, a number of experiments investigated ways of deriving a linear response from the output signals.

For a large number of experiments concerned with signal response, the technique of repeatingly sampling the detector signal level, and coadding the data, was used to reduce the resultant statistical error. This method was used to obtain accurate curves of signal output against either integration time or input flux level.

For some experiments, modifications were made to the electronics (for example, to allow the array to run in a different manner), but for most, the set up described in the previous chapter was used.

5.1 Preliminary Tests

5.1.1 General Array Operation

The output waveforms from the detector, running normally, were photographed from an oscilloscope and are shown in figure 5.1a. The signal levels are reasonably uniform, the exceptions being the first pixel level (displaced due to charge coupling from the transition of the start pulse), pixel nineteen which is illuminated, pixel twenty-seven which was found to have a higher dark current than the other pixels (and is hence referred to as a 'hot' pixel), and pixel thirty-three which is not photo-sensitive and has a constant signal level.

Figure 5.1b shows the effect of very large fluxes on the output. The external bias was zero, so that at saturation the signal level will be approximately half-way between the pedestal and reset levels (VTE $\approx$ 0.5). If the signal rises above this level, then the voltage change on the detector is greater than the initial bias, which leads to a forward biased

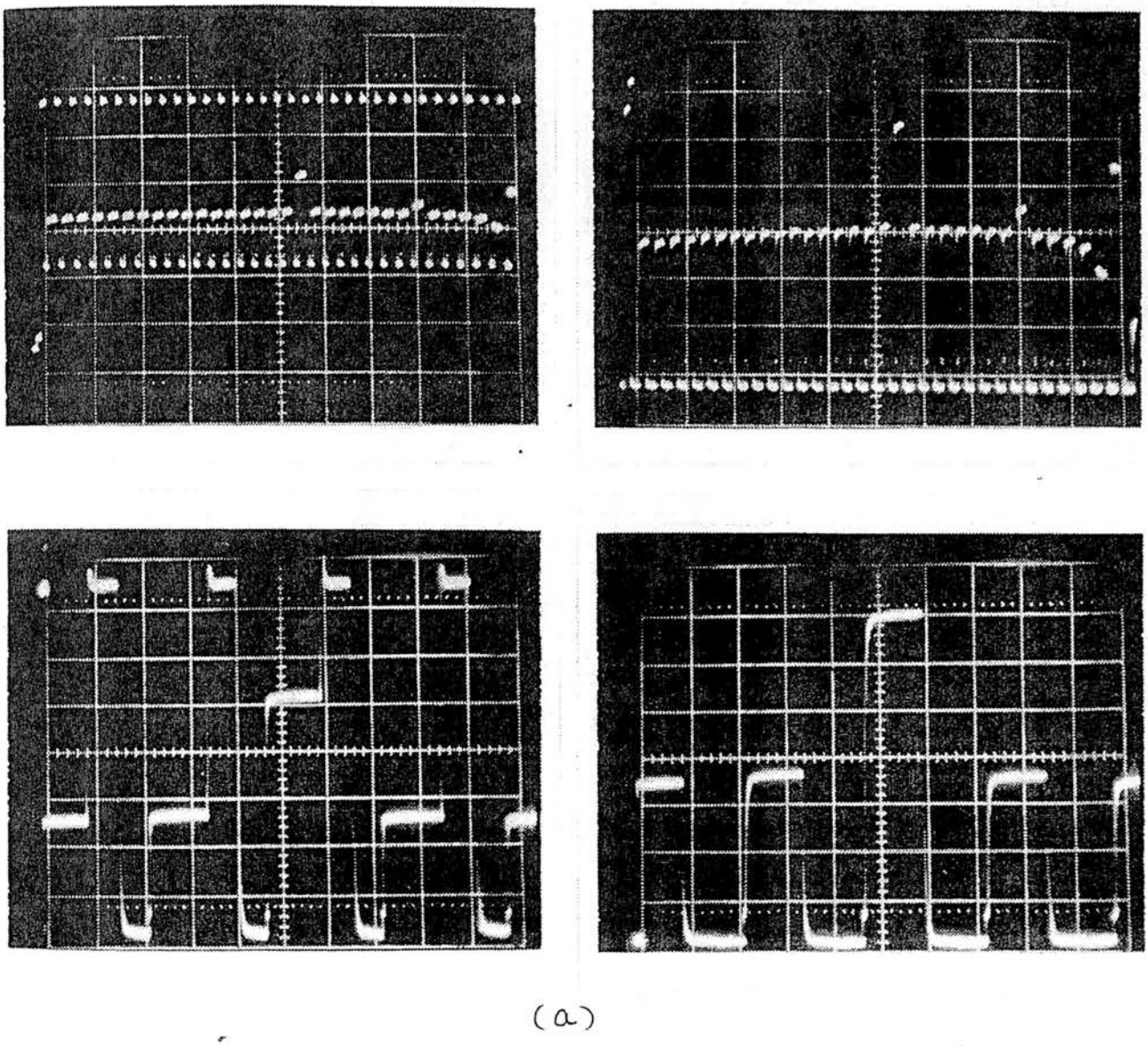

(a)

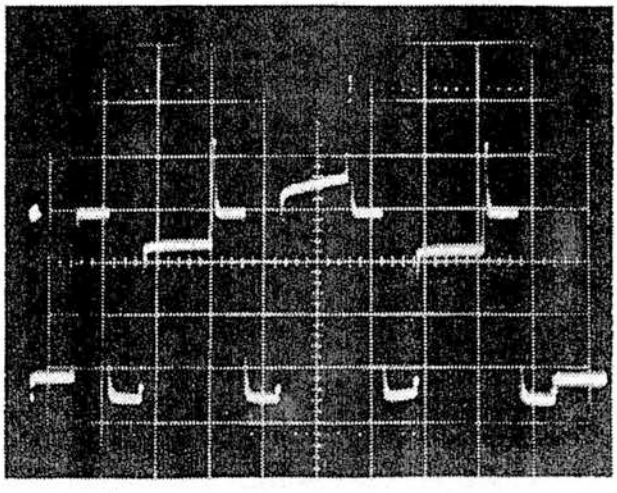

(b)

Figure 5.1
Video waveforms; (a) Postamplifier output (left), clamp output (right), (b) Postamplifier output for large light signal.

diode.

This behaviour can be explained in the following way; When the detector is reverse biased and isolated, so that the detector capacitance is charged, photocurrent and dark current flow in the same direction to discharge it. When fully discharged, the detector bias is zero. Normally, there can be no net flow of current, but if the charges are provided by an external source, such as radiation, a photocurrent will continue to flow, due to the built-in electric field at the junction (causing a displacement in the diode I-V curve towards negative current). This current now acts to charge the detector in the opposite direction. As soon as the detector becomes forward biased, dark current flows in the forward direction, opposing the flow of photocurrent and leading, at readout, to an equilibrium balance between the two, reflected in the signal level.

There are two reasons why it is undesirable to operate the detector in this region. Firstly, the detector impedance falls rapidly, giving rise to large dark currents and short integration times. Secondly, the detector capacitance increases dramatically, leading not only to a higher kTC noise, but also to a greater CTE non-linearity.

The oscilloscope traces of figure 5.2 show the output from the clamp amplifier for a single pixel. The transients in the low-noise ground level are caused by the RC response of the clamp input during the clamp phase. The signal level shown represents the lowest read-noise achieved (short integration time, low signal), measured to be approximately 2300 electrons rms.

5.1.2 Isolating a Single Detector

At an early stage of testing the array, an experiment was carried out to isolate a single detector for observation, by keeping the multiplexer switch closed. This was achieved by constructing a circuit which disabled

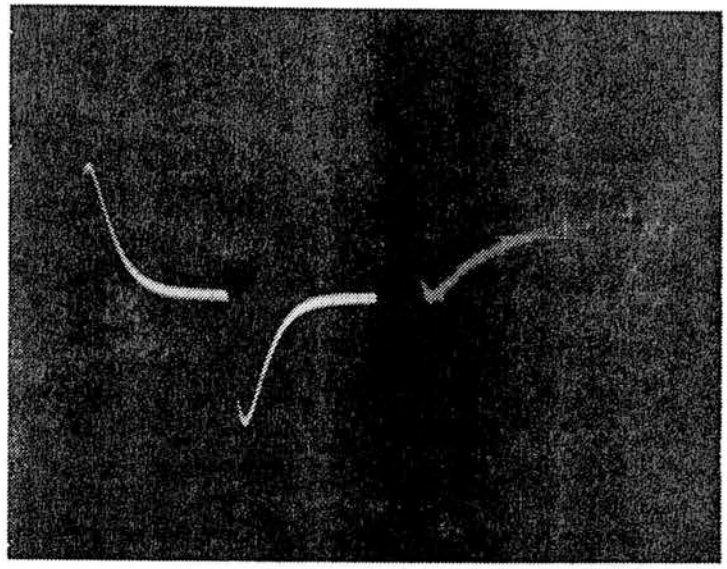

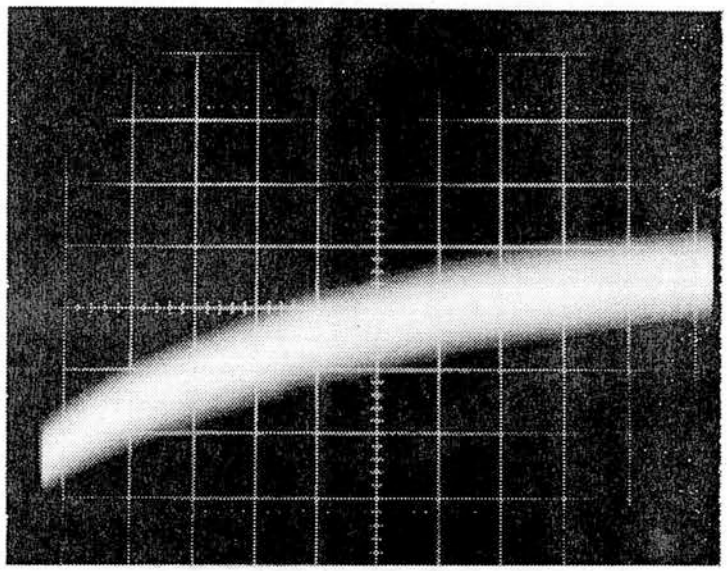

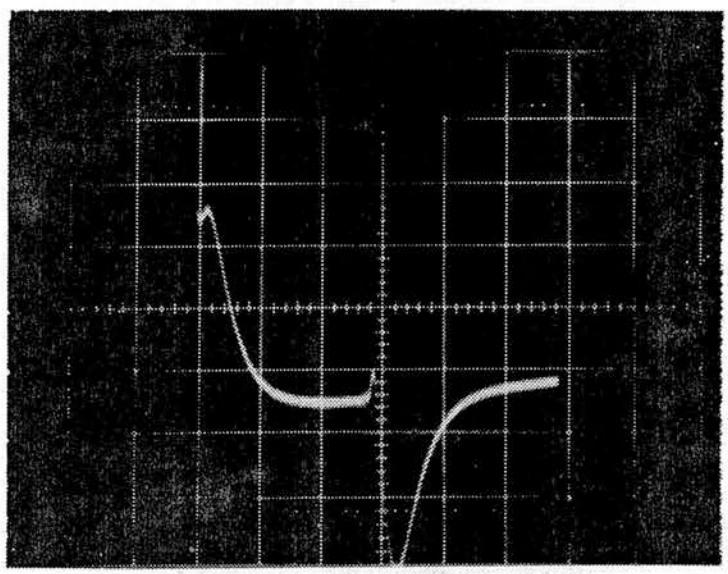

Figure 5.2

Clamp output for a single detector; low signal level (top); noise voltage on signal portion (middle); noise voltage and RC transients on ground reference portion (bottom).

all the driving waveforms at a pre-selected point in the readout. With a slight modification, a reset or start pulse could be applied.

Since the output waveform from the post amplifier was effectively a constant level (ie unmodulated by periodic reset pulses etc.), the noise could be studied with a spectrum analyzer. This showed a prominent 50 Hz component and an increase in the noise power towards low frequencies (<5Hz), which was probably partly due to the post amplifier.

A more useful application of this configuration was the possibility of measuring the JFET gain. This was done by varying the external bias (which at this stage was applied to the array common connecter), and observing the output variation. When the blanked off detector is fully discharged, it is effectively shorted, and the external bias feeds through directly onto the video line. A plot of post amplifier output versus external bias will give a straight line with slope proportional to A_j. The measured gain was A_j = 0.940 +/- 0.005 at a detector temperature of 80 K.

When a periodic reset pulse was applied to the isolated pixel, the noise was observed by digitizing the signal level at a number of positions between consecutive reset pulses, in other words, at different stages of discharge. It was found that the output noise increased by a factor of six in going from a point immediately after reset to a point close to saturation (which occurred in a few hundred milliseconds), but only when an external bias was applied, and could reflect noise on the bias line.

5.1.3 System Gain and Voltage Transfer Efficiency

The VTE of the array is of importance for two reasons; firstly, it leads to signal attenuation, and secondly, it attenuates the detector noise. If the VTE is too small, the detector will not be the noise limiting component of the system, and this will prevent high sensitivity operation. Therefore, the absolute VTE as well as its variation with temperature are of interest.

Measuring the system gain is a relatively simple process, that involves measuring the saturation voltage output averaged over the array pixels, as a function of the external bias. In order to achieve intrinsic saturation levels, the detector must be blanked off and fully discharged by dark current, for reasons described in section 5.1.1.

The signal change at the output of the A/D unit is (section 4.2.2);

$\Delta S = A_s.\Delta V_d = A_s\ (V_f - V_i)$

A_s represents the total signal gain and includes the VTE.

At saturation (V_f=0);

$\Delta S_{sat} = - A_s\ (V_{int} + V_{ext})$

Thus, a plot of saturation signal against V_{ext} will give A_s and V_{int}, and from A_s the VTE can be calculated. The results of measurements made at six detector temperatures are summarised in table 5.1. Between three and eight saturation values were taken at each temperature, over a bias range of -10 to -70mV.

Table 5.1

Temperature (K)	V_{int} (mV)	A_s (VL gain) (dn/mV)	A_j	VTE_{sat}
54	78.4	22.14	0.925	0.444
57	72.4	22.60	0.930	0.451
67	65.6	23.72	0.935	0.471
71	64.3	24.01	0.937	0.475
75	62.5	24.25	0.938	0.480
80	60.8	24.77	0.940	0.489
	+/- 0.2	+/- 0.1	+/- 0.001	+/- 0.003

The response equation (3.5) reduces, at saturation, to;

$$- \frac{\Delta V_v}{V_i} = \frac{C_d(V_s)}{C_d(V_s) + C_t} = VTE_{sat}$$

where $V_s = V_i + \Delta V_v \approx V_i\ (1 - \overline{VTE})$

For the bias range used, the variation in the detector capacitance is small, and the VTE is approximately constant. This is reflected in the small errors in the gradients, measured using least squares fitting.

The error in the value of V_{int} will be larger than would be judged from the straight line fit, due to differences in the ground potential between the power supply and the detector, which will cause an offset in the measured value of V_{ext} of a few millivolts.

The variatiation of A_j was derived by combining a plot of the relative gain as a function of temperature (supplied by CE Corp.) with the absolute value measured at 80 K. The VTE could then be inferred using the gains already measured for the control electronics.

The temperature dependence of the VTE and V_{int} are probably mainly due to capacitance variations. The VTE change seems to indicate a drop in C_d with decreasing temperature, which is confirmed by Wimmers and Smith (see Wimmers, 1982), who observed a 7% drop in InSb diodes going from 80 to 54K.

The VTE variation is smooth and would suggest that operation as low as 30 K is feasible, though at this temperature A_j has dropped dramatically, and the JFET may in fact not operate (this problem could be overcome by thermal isolation from the device, allowing self-heating in the JFET to keep it operating at optimum gain).

Once the system gain is known, then the output signal can be translated into voltage changes at the detector, which is useful for deriving the diode I-V characteristics and the intrinsic detector response. This technique was used for presenting most of the results.

There are two points worth noting about the results of the last experiment. Firstly, the derived VTE represents the VTE at saturation, which differs from the VTE at other readout points as predicted by the

results of the response analysis (section 3.4), so that this represents the maximum VTE for a given initial bias.

Secondly, there is another effect leading to a discrepancy between the measured VTE_{sat} and the true VTE_{sat}, caused by the variation of V_{int} with V_{ext}, as predicted by equation 3.2. It would be expected that, as the external bias is increased (in the reverse bias direction), the internal bias will also increase, and this was observed (figure 5.3a) by measuring the difference between the reset and pedestal portions (which equals V_{int}) of the video output, directly from an oscilloscope.

The magnitude of this effect on VTE_{sat} is illustrated in figure 5.3b which shows the true saturation output. As can be seen, the effect is not dramatic at 80K for moderate values of bias.

This effect is of little importance to the practical running of the array where only the approximate detector bias (ie +/- 10%) is of interest, and bias stability is more important. The reason it is mentioned in this context is to show the difficulties involved in measuring the intrinsic detector characteristics, which are modified at readout by the two effects; the variation of V_{int} with V_{ext} and the VTE non-linearity. An attempt will be made to correct for both of these effects to demonstrate the true I-V detector behaviour, but the corrections are constrained by the use of the capacitance data supplied by the CE Corporation.

5.1.4 Pixel to Pixel Capacitance Variations

There are two effects leading to pixel differences; the odd/even modulation of the signal levels and capacitance variations. The former will cause a distinct difference between the odd and even pixel biases, whereas the latter will add 'noise' to the bias variation.

Pixel to pixel variations are undesirable because;

(i) There will be a variation in the dark current contribution across the array, which must be subtracted accurately from each pixel to

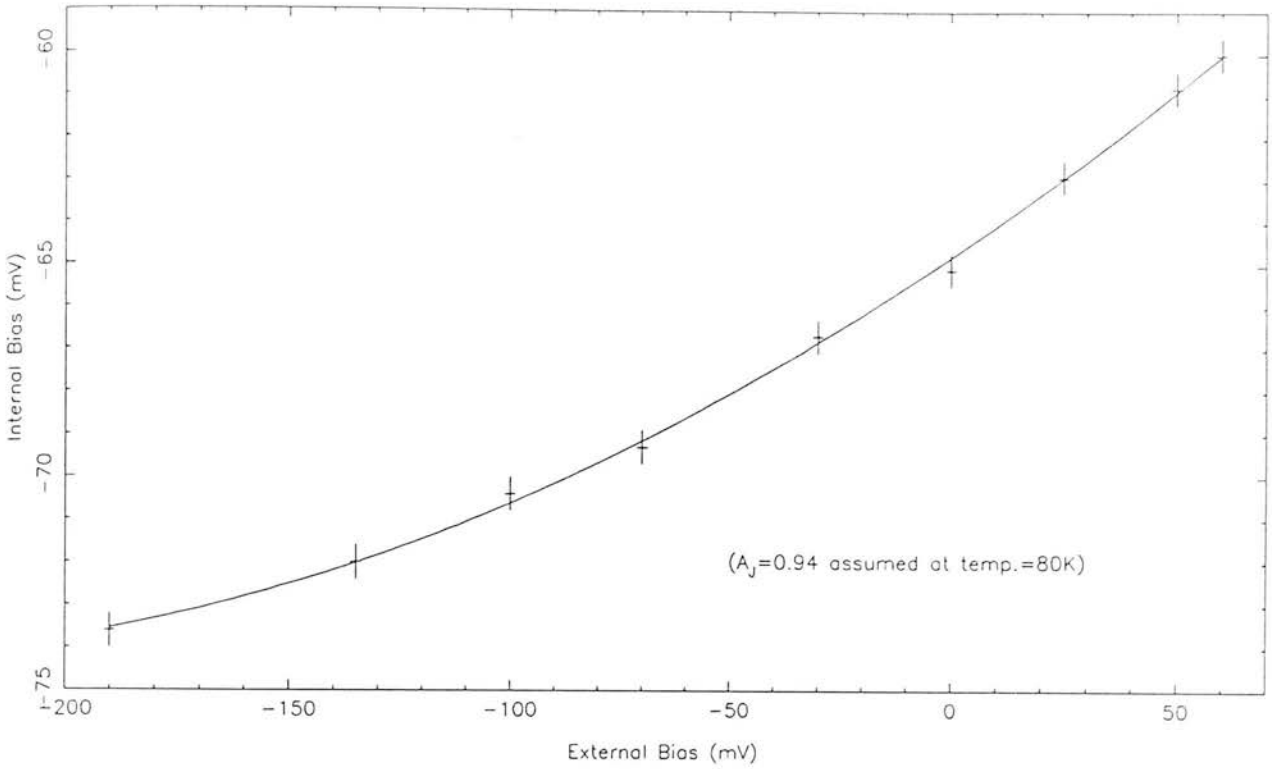

Figure 5.3a
Measured variation of internal bias as a function of external bias (for V_{ext}=60mV, the total bias was found to be zero, implying that V_{int}=-60mV).

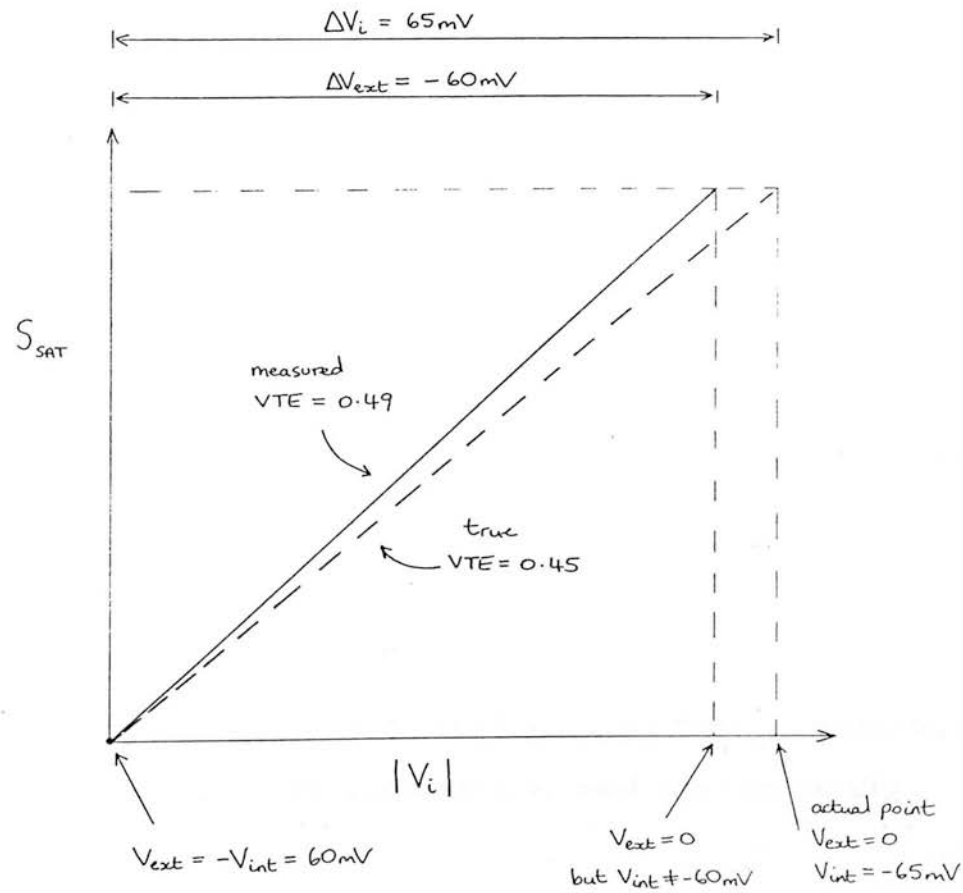

Figure 5.3b : True VTE_{sat} at 80K.

maximize the sensitivity.

(ii) Pedestal variations across the array (fixed pattern noise), if of large amplitude, may cause problems in the high gain, signal processing circuitry. An example of this is the spurious level of the first pixel. By the output of the clamp amplifier, this level is outside the range of the A/D converter and is therefore lost. This pixel could be recovered, however, by placing a dummy diode at the beginning of the array.

The bias variation across the array was measured by recording the output signals for a saturation frame (t_i = 200ms at 80K. Array blanked off), and subtracting from this a 2ms integration frame, for which the total detector bias was set to zero volts, in order to cancel out voltage offsets. The result represents the intrinsic saturation level, which, when divided by the system gain, gives the initial bias applied to each detector. As can be seen from figure 5.4a, there is a clear odd/even effect which gives rise to a 1.3% bias difference. Since the magnitude of this effect is dependent on the shape of Φ_1 and Φ_2 it should be possible to minimize at the point where the clocks are generated, in the control electronics, though these results represent the smallest difference that could be achieved with this set-up.

The variation in the detector capacitance can be found by measuring each pixel's bias variation from the mean level of its respective group (odd or even), and this is shown in figure 5.4b. The standard deviation of this distribution is 0.2%. By differentiating equation 3.3 and substituting in the mean VTE, then;

$$\frac{dC_d}{C_d} \approx - \left(\overline{VTE} \right)^{-1} \frac{dV_{int}}{V_{int}} \qquad (5.1)$$

This implies a corresponding variation in the pixel capacitance, across the array, of 0.4 % rms, and consequently, good pixel uniformity.

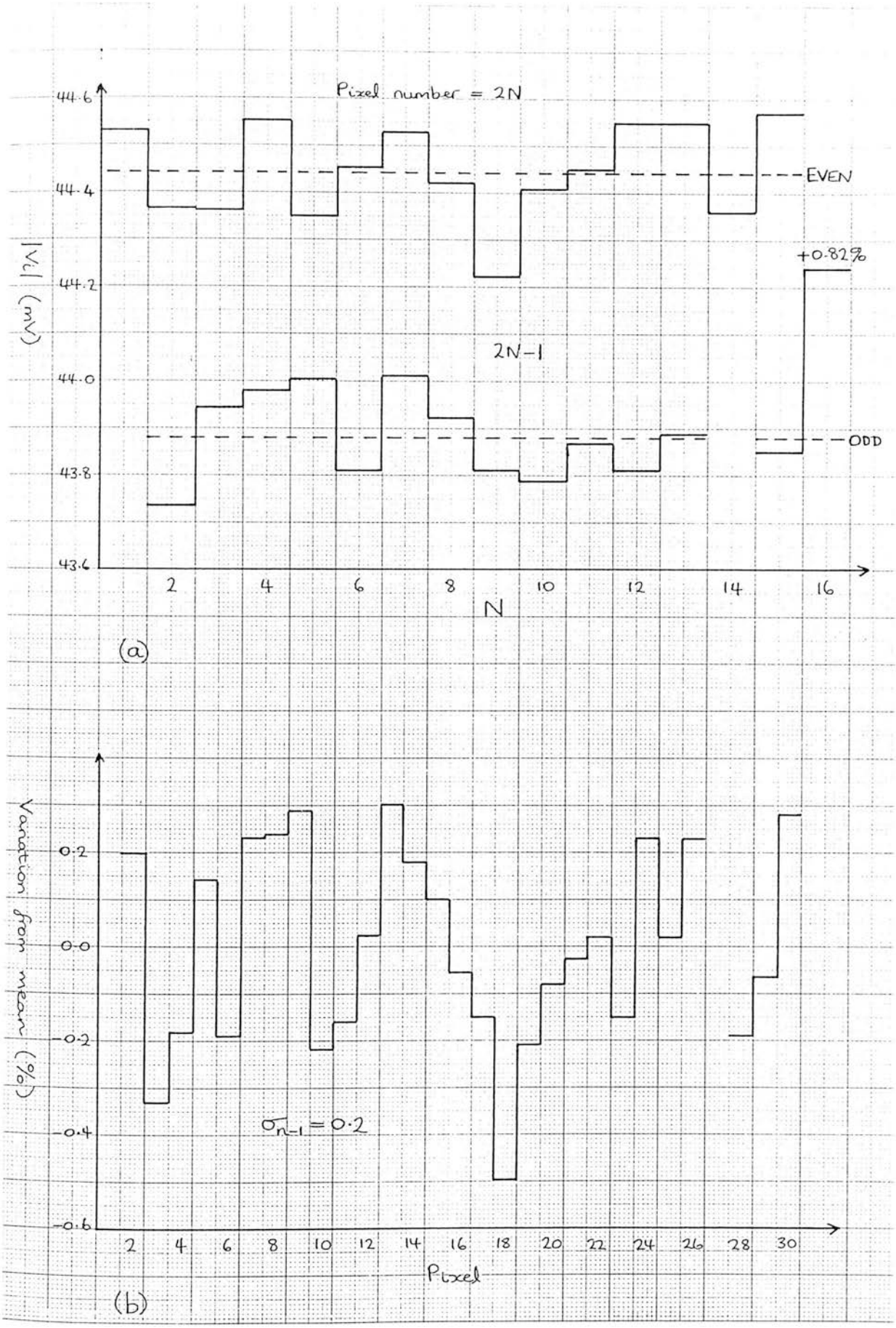

Figure 5.4
Initial bias across array (a), and variation from respective odd / even mean (b).

5.1.5 Scanning a Light Spot across the Array

A spot of light, whose dimensions are small compared with the detector element size, scanned across the array, is useful for measuring cross-talk between adjacent pixels, for checking the array geometry, and the response uniformity (though the latter is best achieved using a uniform field across the whole array).

Using the smallest black body aperture and restricting the lens aperture by closing the iris diaphragm, in order to minimize the aberrations, a spot was focussed on pixel fifteen by peaking up the signal on an oscilloscope, and was then scanned across the array by moving the black body parallel to it. The positional accuracy was approximately 1/2 mm, which corresponds to 15 μm at the array. For each position of the black body, the signal was recorded from five adjacent pixels and the background subtracted results are displayed in figure 5.5.

The separation of two consecutive crossing points gives an effective detector width of 230 μm, in agreement with the specification. The reason the crossing points occur below the half-maximum level is due to the presence of the 30 μm dead space.

It is possible to estimate the illuminating spot diameter in the following manner;

Assume the spot is circular, uniformly illuminated, and is centred on the mid-line running parallel to the array. The expected ratio of detector illumination between the peak (ie. centred on a detector) and crossover (ie. mid-way between two detectors) positions of the spot, given the spot radius, dead space and detector width, can then be calculated. This is equivalent to the signal ratio at these two positions.

Comparing the measured ratio for pixel seventeen with the derived curve of figure 5.6 gives a spot diameter of 234+/-10 μm, in which case, when peaked, roughly 90% of the light falls on a single detector.

The low signal at pixels sixteen and eighteen when seventeen is

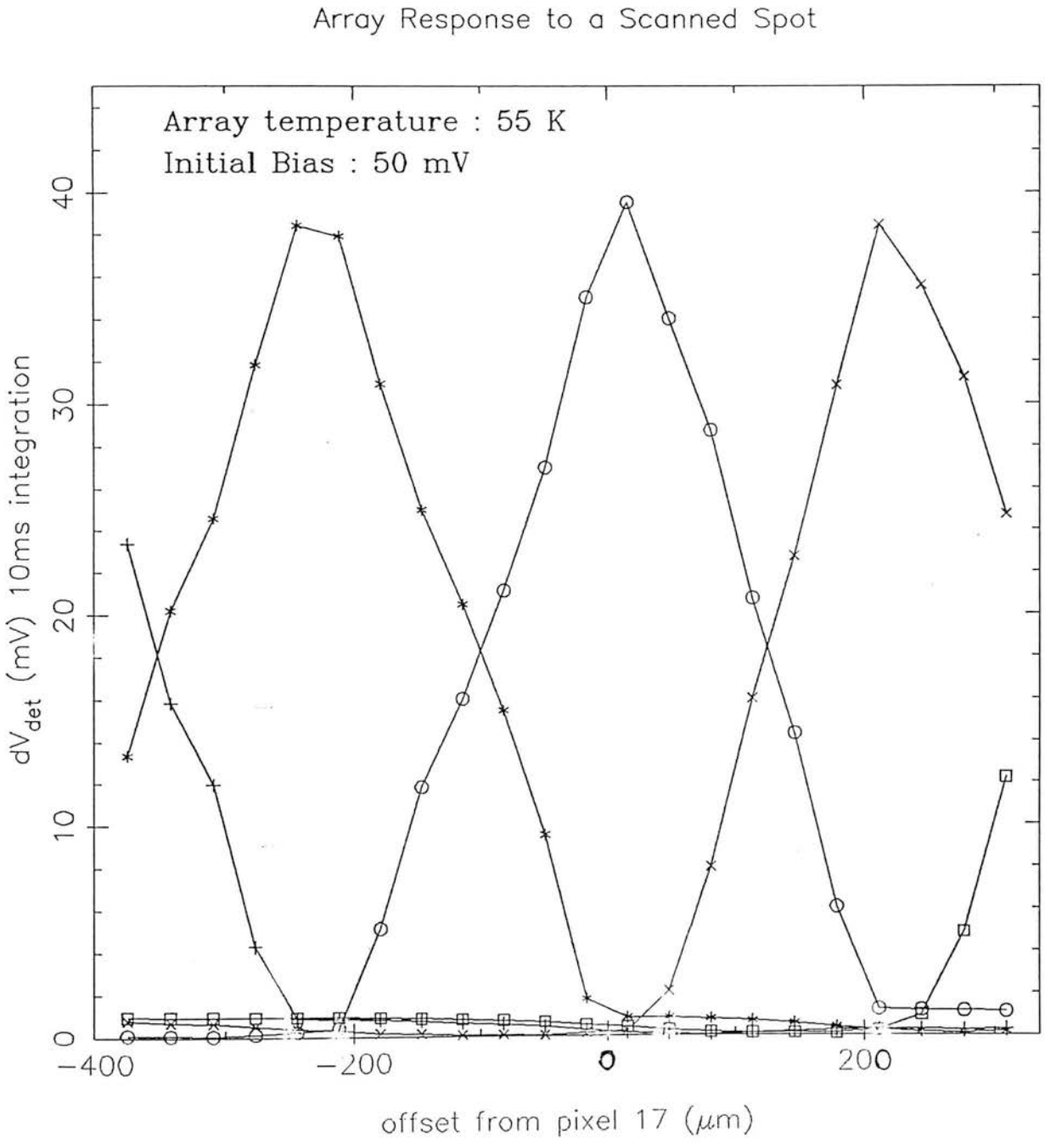
Array Response to a Scanned Spot
Array temperature : 55 K
Initial Bias : 50 mV
dV_det (mV) 10ms integration
0
10
20
30
40
−400
−200
0
200
offset from pixel 17 (μm)

Figure 5.5

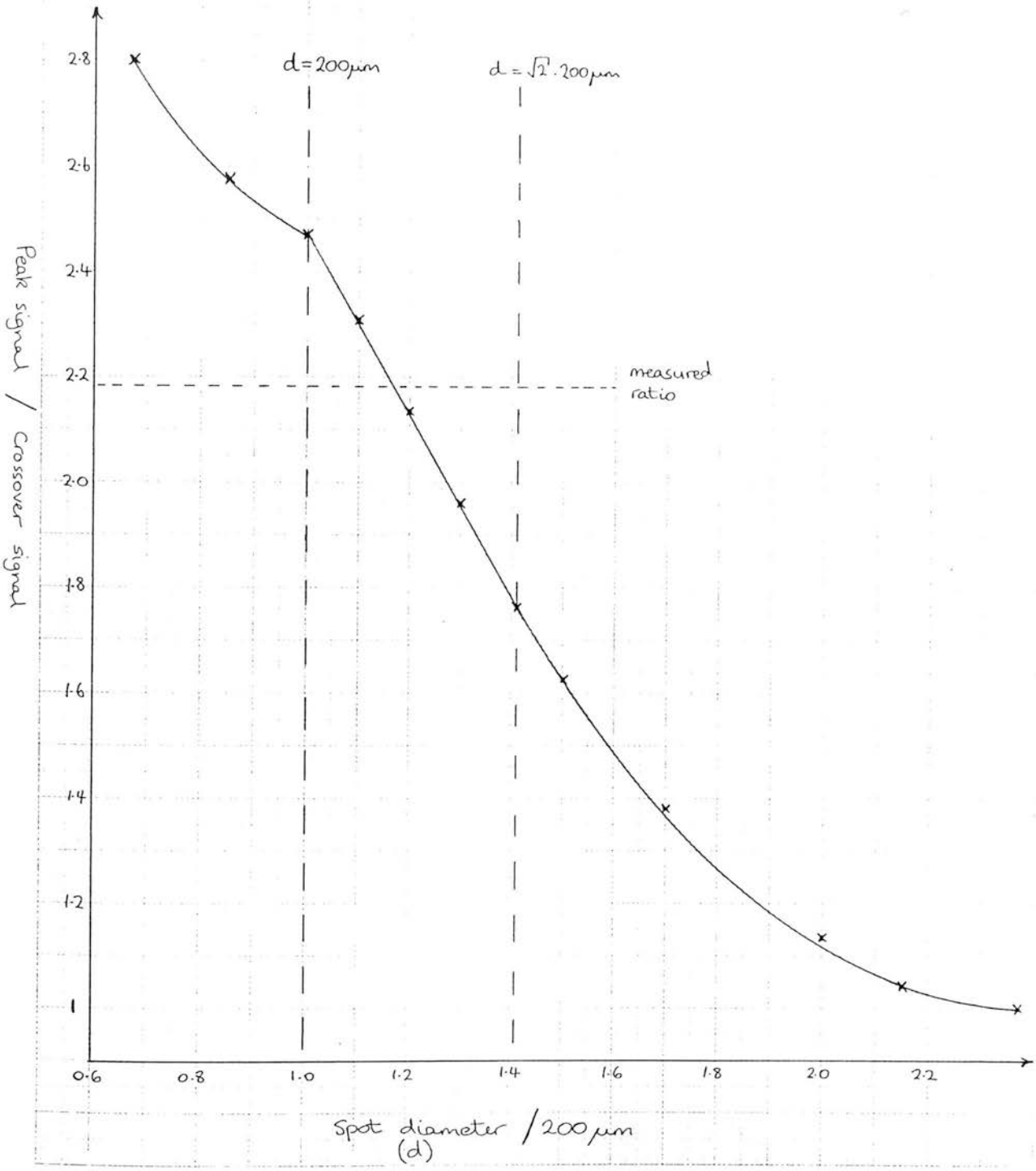

Figure 5.6
Estimation of illuminating spot diameter at array.

peaked reflects a reasonably low level of cross-talk, though the sensitivity to this particular measurement is poor, due to the large spot diameter and uncertainties in the background illumination.

5.2 Array Noise Behaviour

An understanding of the noise behavior of the detector is important for judging the most sensitive mode of operation of an infrared instrument.

An ideal detector would not add noise to the detected signal. A nearly ideal detector would contribute a readout noise (ie. kTC noise), which was independent of operational variables such as integration time and storage capacity (or bias). It would then be a simple matter of integrating charge on the detectors, until the shot noise of the object plus background was greater than the read noise, at which point the integration time is irrelevant, and the instrument is operating under high sensitivity, BLIP conditions.

In general, however, there are other sources of noise present which will affect the detector's ability to reach this state (see section 3.4).

Noise measurements were made by selecting a pixel, sampling the output a large number of times ($\geq$100), and taking the standard deviation of the signal level as being representative of the noise voltage.

Initially, different sampling arrangements were tried, to find the signal output with the lowest noise, using the post amplifier output, and these results were compared with the clamp output. It was found that;

(i) The noise on the signal and pedestal portions of the video output were twice as large as the noise on the difference (signal-pedestal), suggesting a strong correlation between these two levels (random noise would give an increase of $\sqrt{2}$).

(ii) Referencing the signal portion to its own pedestal produced a small increase in noise (13%), compared to referencing to the preceeding

pedestal. This result was reproducible, and may reflect removal of some of the kTC noise component.

(iii) The noise from the clamp output (set up to difference the signal and preceeding pedestal portions) was compared with the noise resulting from differencing the two levels in the software (by connecting the post amplifier signal directly to the A/D unit). It was found that the clamp was certainly no worse than the latter method and possibly slightly better. The clamp was therefore used for reasons already discussed and, in addition, to provide gain-sharing between the two operational amplifiers in order to keep the signal bandwidth large.

The readout noise, which represents the noise on the signal level for a quick, zero discharge, readout was measured to be stable, at around 2300 electrons rms, in time, and for the temperature range used (made in H gain mode, and using the value of C_e derived in section 4.2.2). A typical distribution of the signal level, from a large number of samples, is shown in figure 5.7. The Gaussian fit (which has a value of sigma in good agreement with the standard deviation returned by the Fortran statistics routine) shows that the noise is randomly distributed.

If a detector is illuminated and the signal level steadily increased, then the readout noise increases above that expected by the addition of shot noise. An example of this effect is shown in figure 5.8, where the top set of data represents the noise under illumination (no dark current) for different values of initial bias. The lower data, representing noise from dark current discharge only, does not seem to suffer from this excess noise. This seems to indicate that the excess noise originates externally with respect to the detector, even though the apparatus was mechanically stable, and the short term stability of the black body was excellent. The excess noise, which seems to be independent of bias and illumination level, but dependent on readout point, was always present when the array was not blanked off at the cold shield.

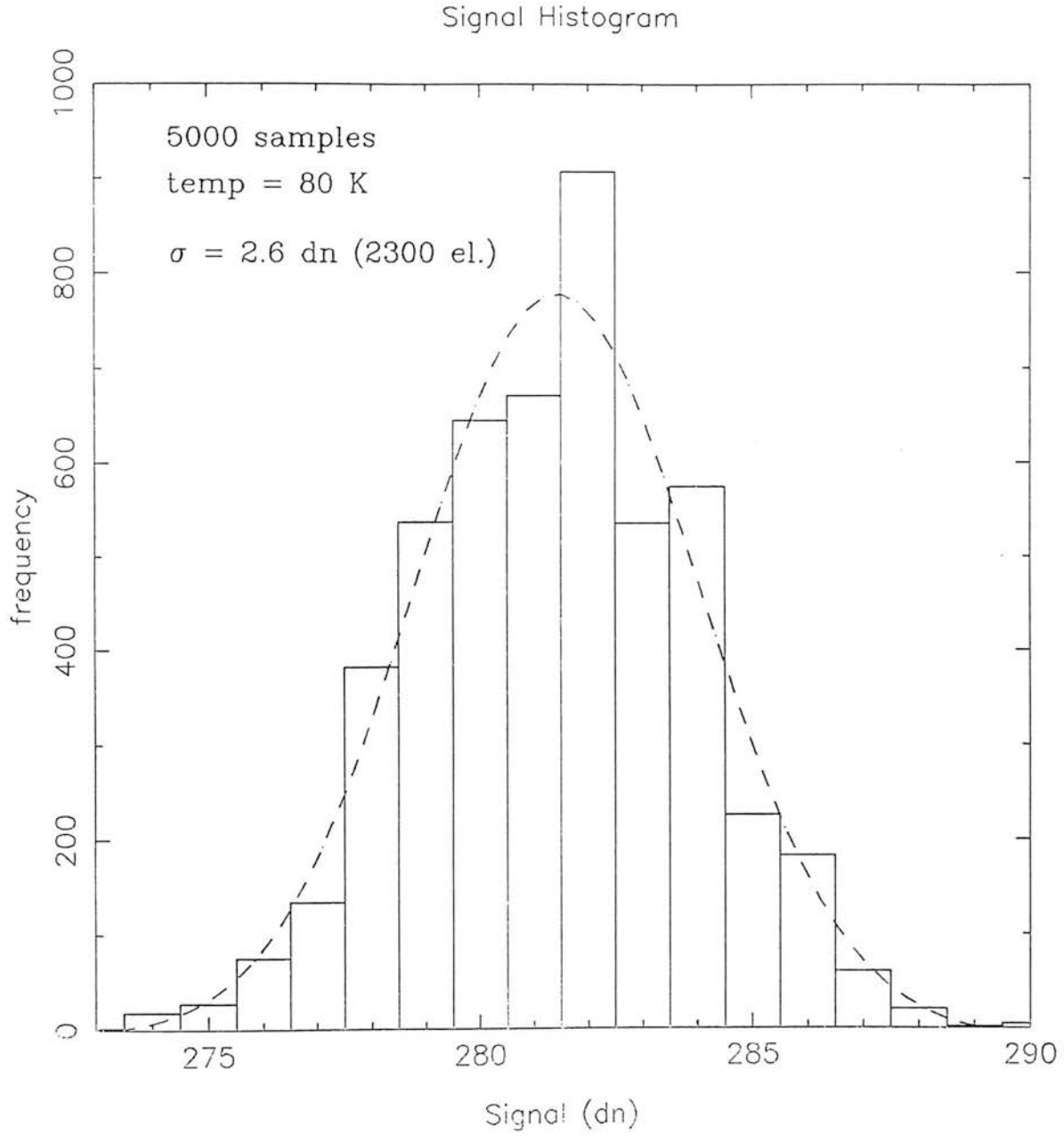
Signal Histogram
5000 samples
temp = 80 K
σ = 2.6 dn (2300 el.)
frequency
0
200
400
600
800
1000
275
280
285
290
Signal (dn)

Figure 5.7

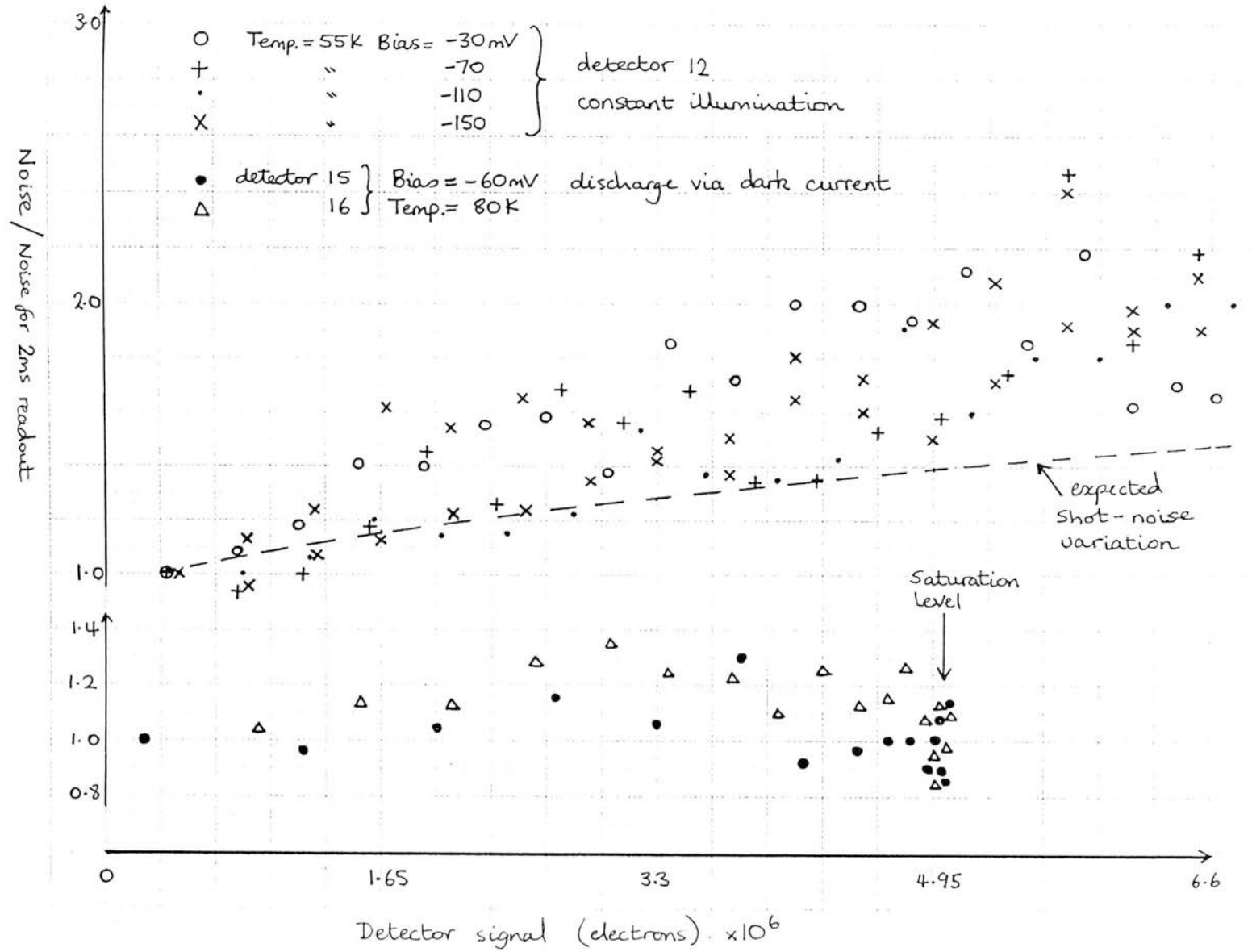

Figure 5.8
Observed readout noise under both dark and light conditions.

When the blanked-off detector is saturated (effectively short-circuit), the read noise falls, as expected, possibly leaving only the kTC contribution.

Finger et al. (Finger, 1987) found that the detector readout noise increased with increasing t_i and reverse bias, and for this reason operate the photodiodes at a bias of approximately -20 mV.

There is still a lot of work which needs to be done in order to characterise the noise behaviour of this device.

5.2.1 Lower Limit Determination of Detector Capacitance

Though knowledge of this quantity is not crucial for the normal running of the array, it is useful for indicating the Johnson noise limit of the detector. In this context it was felt that a measurement was justified, on the grounds that it would confirm the data supplied by CE, and would add weight to the modelling results of chapter 3.

A standard method for measuring the detector capacitance (or, more exactly, the conversion factor, C_e, of the system) is used frequently for CCDs (see Janesick, 1984) and involves measuring the shot noise of the output signal. This is easy to do with CCDs, where the read noise is very low (tens of electrons), and storage capacity large ($\approx 10^6$ electrons), but for infrared detectors the dynamic range is typically two orders of magnitude smaller, and shot noise is thus harder to observe.

If, at the output, the signal from a detector is S, the total noise N, and the readout noise R, each quantity being in data numbers, then, in terms of the number of incident photons in t_i, N_γ (and dark charges, N_d), the signal will be;

$$S = \frac{qe.N_\gamma + N_d}{C_e}$$

The total noise will be the sum of two independent contributions (read and shot noise);

$$N^2 = R^2 + \left[\frac{\sqrt{(qe.N_\gamma + N_d)}}{C_e} \right]^2$$

Combining these equations gives;

$$S = C_e (N^2 - R^2)$$

By altering the illumination level (at constant t_i), the relation between the signal and noise can be used to derive C_e. The noise values, N and R, can be determined accurately by creating a noise histogram at a constant signal. This is done by combining data from up to 500 runs, each run representing a large number of signal samples (typically fifty), and a single noise measurement. The mean error in the noise is reduced in proportion to the square root of the number of runs. The results from this procedure are shown in figure 5.9a for two different flux levels. The low signal represented 7% saturation and the high signal, 50%.

The results from several similar experiments, taken over a range of conditions, were normalised (to a noise measurement made for a small output signal) and combined, and are summarised in figure 5.9b.

Since the noise can only be greater than, or equal to, the read and shot noise combined, the results will give a lower limit to C_e and therefore to C_d. A least squares fit to the data implies a value of 4 pF, but from the appearance of the results the error is obviously large, due to variations in the excess noise observed.

5.3 Detector Linearity

The response of the detector to different incident flux levels was studied at 54 K, where the dark current is negligible in comparison to the photocurrent. (The lowest rate of detector discharge, achieved when the CaF_2 window/lens was covered with a reflecting surface, and due to imperfect baffling, was ≈ 0.6 V/sec. For a detector capacitance of 13 pF, this represents a photon flux through the K filter of 6×10^7 γ/sec or 5×10^{-12} W, and saturates a detector, at moderate bias, in about 100 ms.

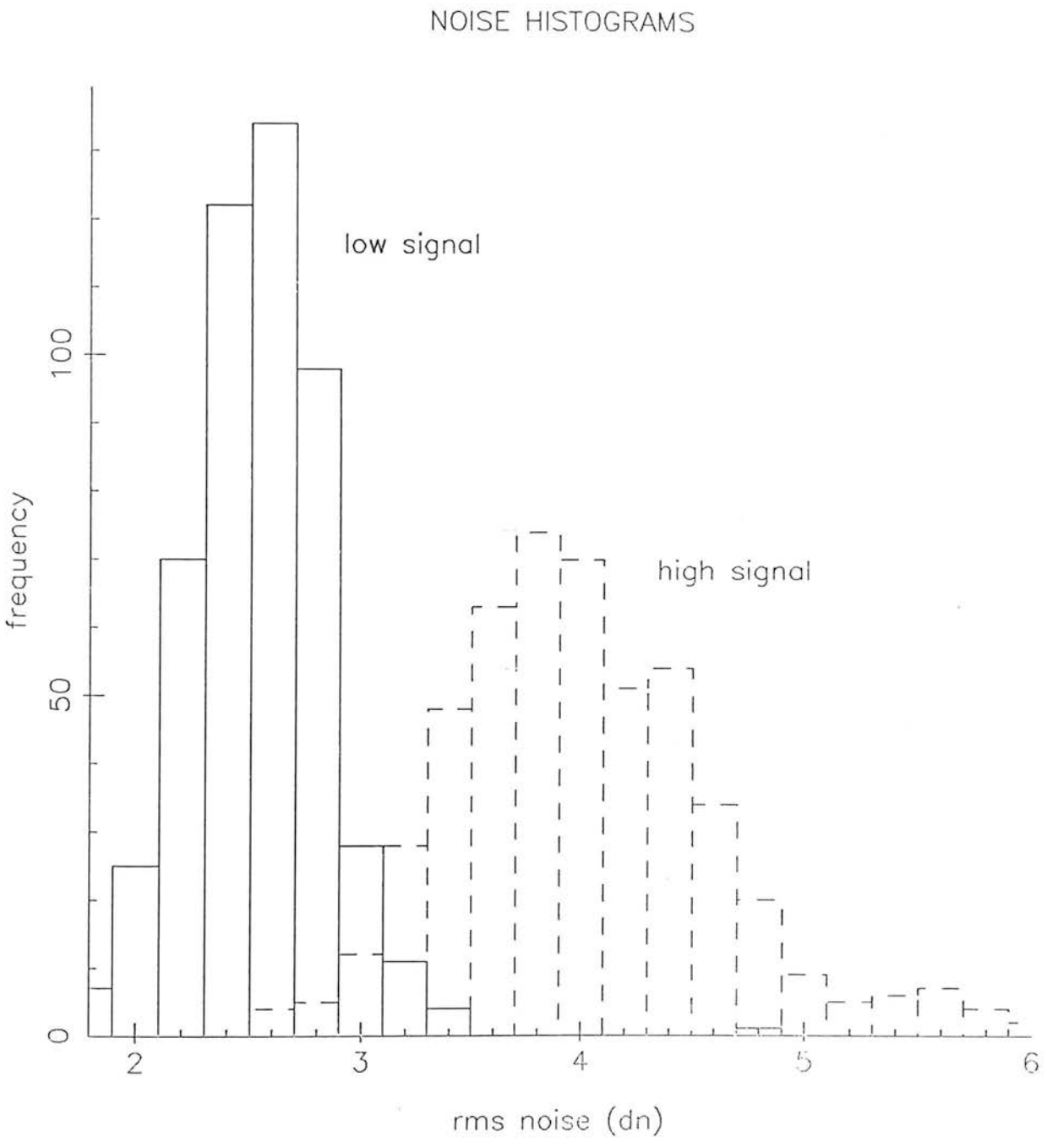

Figure 5.9a
Noise histograms (500 runs, where each run consists of 50 signal samples).

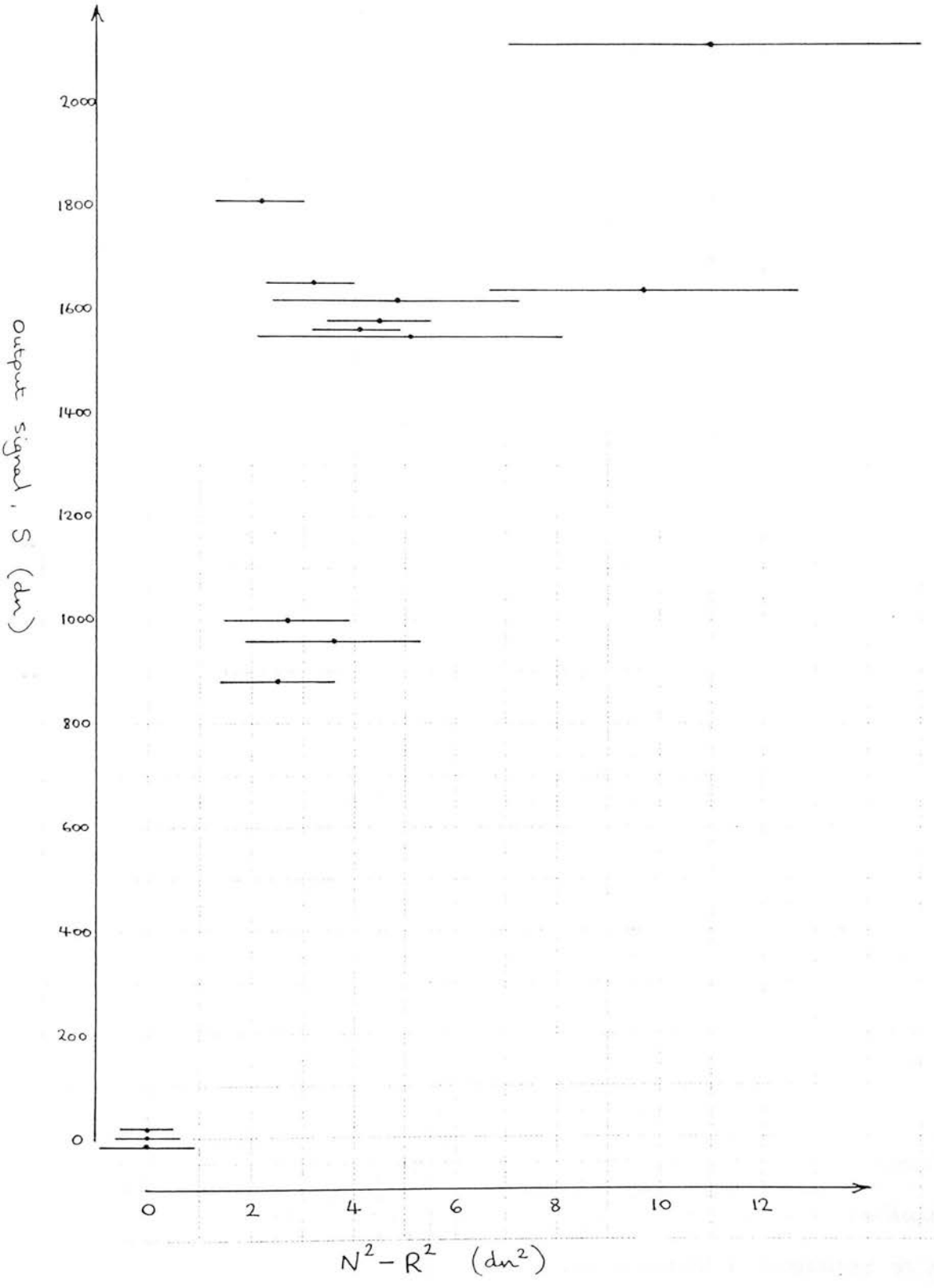

Figure 5.9b : Derivation of C_e.

The initial dark current at 54 K (and -80mV) was measured to be -24 fA, which implies a voltage discharge rate of 0.002 V/sec, in other words, three hundred times smaller than the minimum photocurrent.)

Two similar methods were used to investigate the linearity;

(i) The signal output from a detector was measured, at constant t_i, as a function of the flux (measured in arbitrary units). The relative illumination of two fluxes, F_1 and F_2, can be measured by varying the respective integration times, t_1 and t_2, until the output signals are equal, at which point $F_1.t_1 = F_2.t_2$, and F_2/F_1 is found.

The response curve for an initial bias of -80 mV is shown in figure 5.10. The solid line represents an ideal, or linear, response based on the assumption that for low output levels, the detector is linear. A more formal definition of non-linearity is;

$$\text{non-linearity} = 1 - \frac{\Delta V_{\text{actual}}}{\Delta V_{\text{ideal}}} \equiv 1 - \frac{CTE_{\text{actual}}}{CTE_{\text{ideal}}}$$

The ideal values refer to the initial response, as predicted by equation 3.8, when the CTE is at a maximum. ΔV refers to voltage changes at the device output.

As the output approaches saturation, it drops below the predicted ideal output, implying a fall in the charge transfer efficiency, and a positive value of non-linearity.

Even so, the actual response shows excellent linearity, with the saturation signal deviating from the ideal by only 1%.

The non-linearity, as defined above, describes a difference in 'gain' between actual and ideal (ie. linear) conditions, and was adopted because it relates directly to practical operation, where a signal is measured at a given discharge point, and must then be related to the brightness of the object under observation. This approach will be discussed and extended in section 6.3, when the additional influence of dark current is considered.

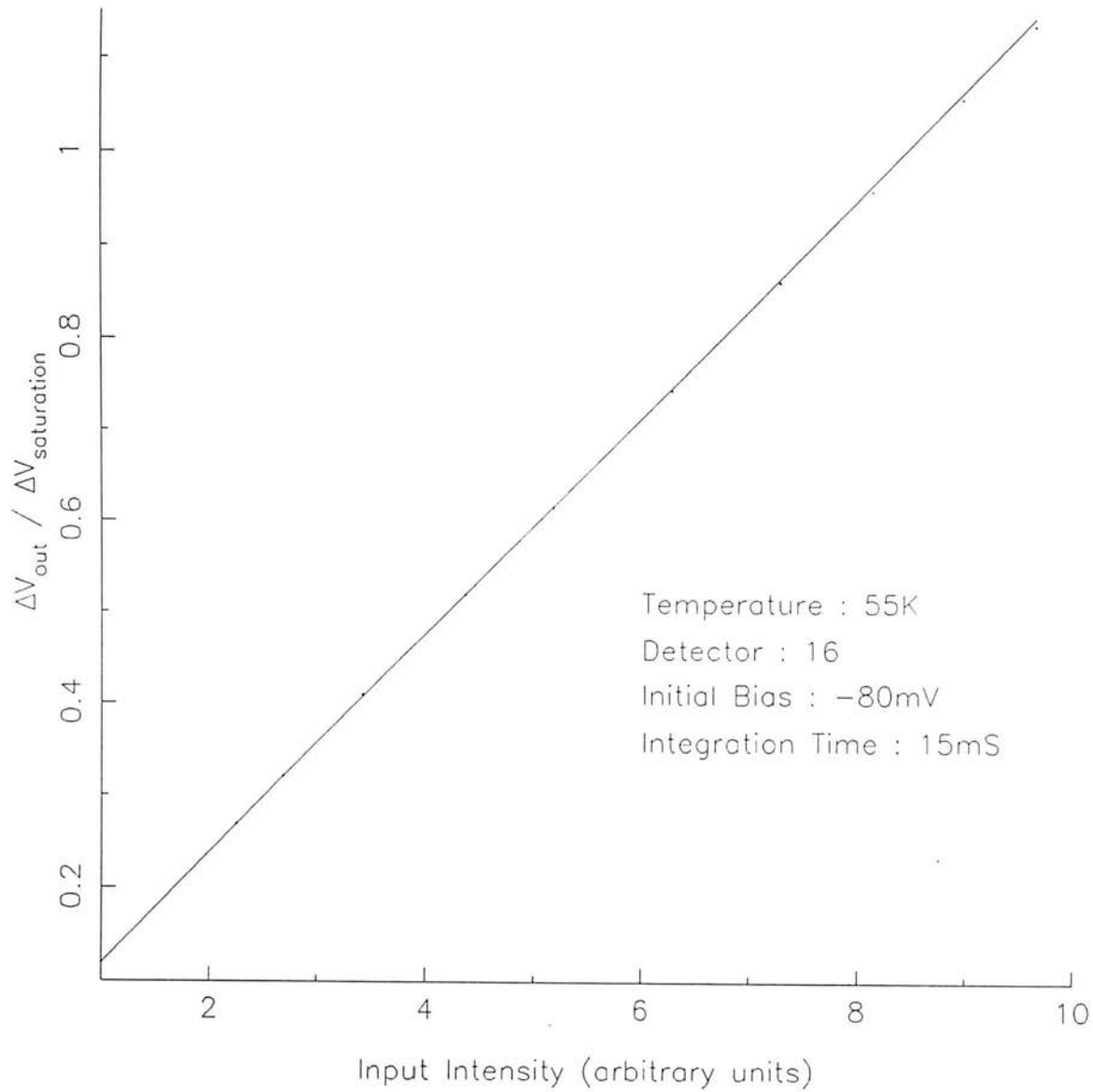

Figure 5.10 : Detector response to light (errors in points: $x \leqslant 0.02, y \leqslant 0.0005$).

(ii) The disadvantage with the method just described was the large time required to measure the relative fluxes. A simpler method was to set the flux at the detector to a constant level, vary the integration time, and record the signal variation. Again, the errors in the signal could be reduced by taking a large number of samples, and the software was set up to record signal curves automatically.

Once a signal curve was obtained, the non-linearity was derived by fitting the signal with a third order polynomial (rms residuals of the order of 0.1 to 0.5 mV), which was then differentiated. The gradient was found to decrease as saturation was approached, as expected. The initial slope was obtained from this curve, which was then used to derive a linear response starting from the first point of the actual signal curve. This was divided into the signal curve to give the quantity $\Delta V_{actual}/\Delta V_{ideal}$.

A typical set of results is shown in figure 5.11 for a range of initial biases, but the same flux level. From these and other results, there did not appear to be a significant difference between the bias values as predicted by the modelling. The reason for this could be due to the inaccuracy involved in the experimental derivation of the non-linearity, or an extra, bias dependent, non-linear contribution at the detector, not accounted for. In any case, the predicted differences between the initial bias range used are small, even close to saturation, at about 1%, and would therefore be difficult to measure.

An interesting aspect of these detectors is that they can also integrate signal in the forward bias direction, as already described. This effect is illustrated in figure 5.12, which represents data taken at a constant illumination.

The response past saturation is highly non-linear. The first two curves (0 and -20 mV) seem to be levelling out at a separation of roughly 20 mV, implying that the non-linearity is due more to high dark current

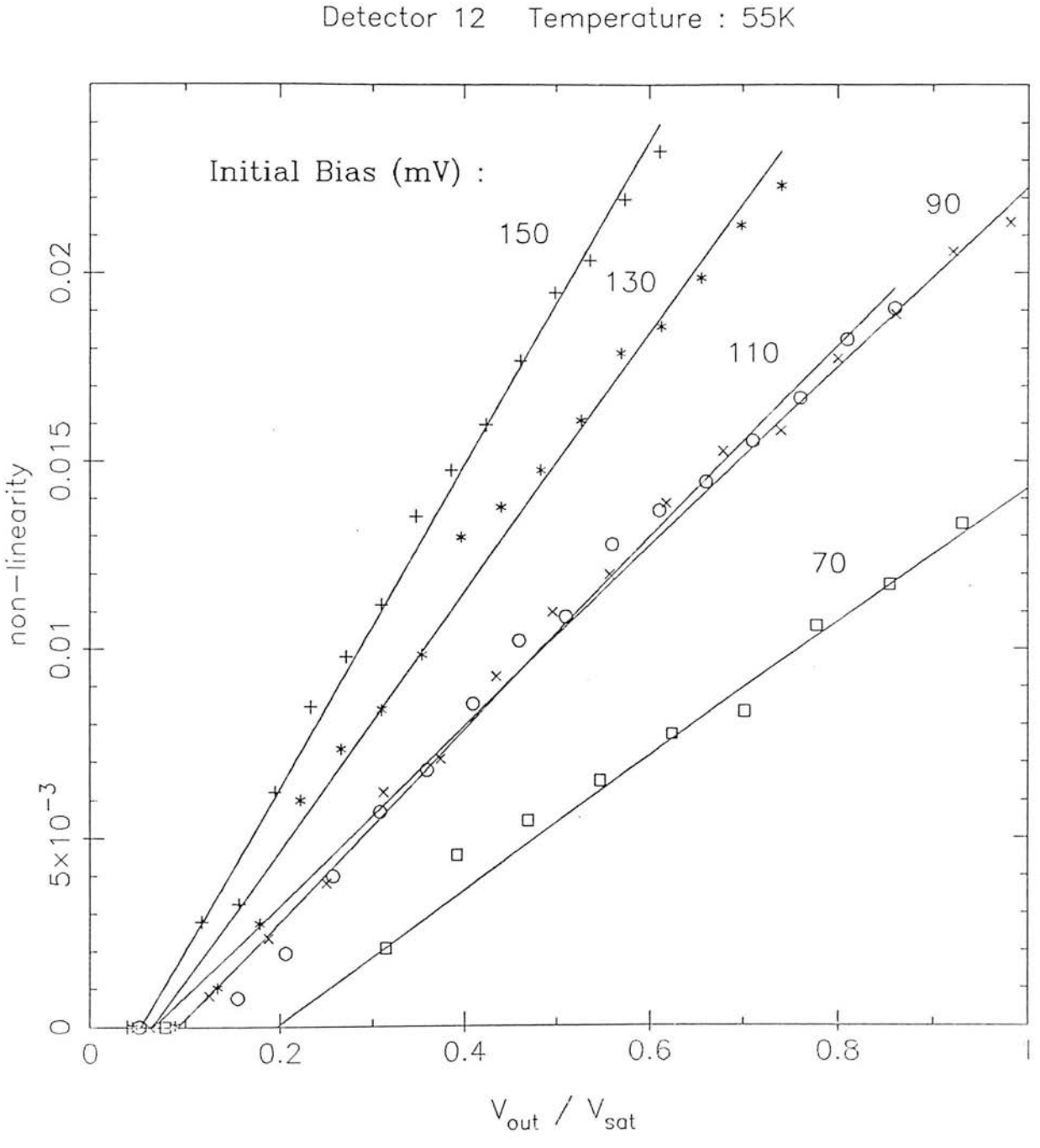

Figure 5.11 : Observed non-linearity.

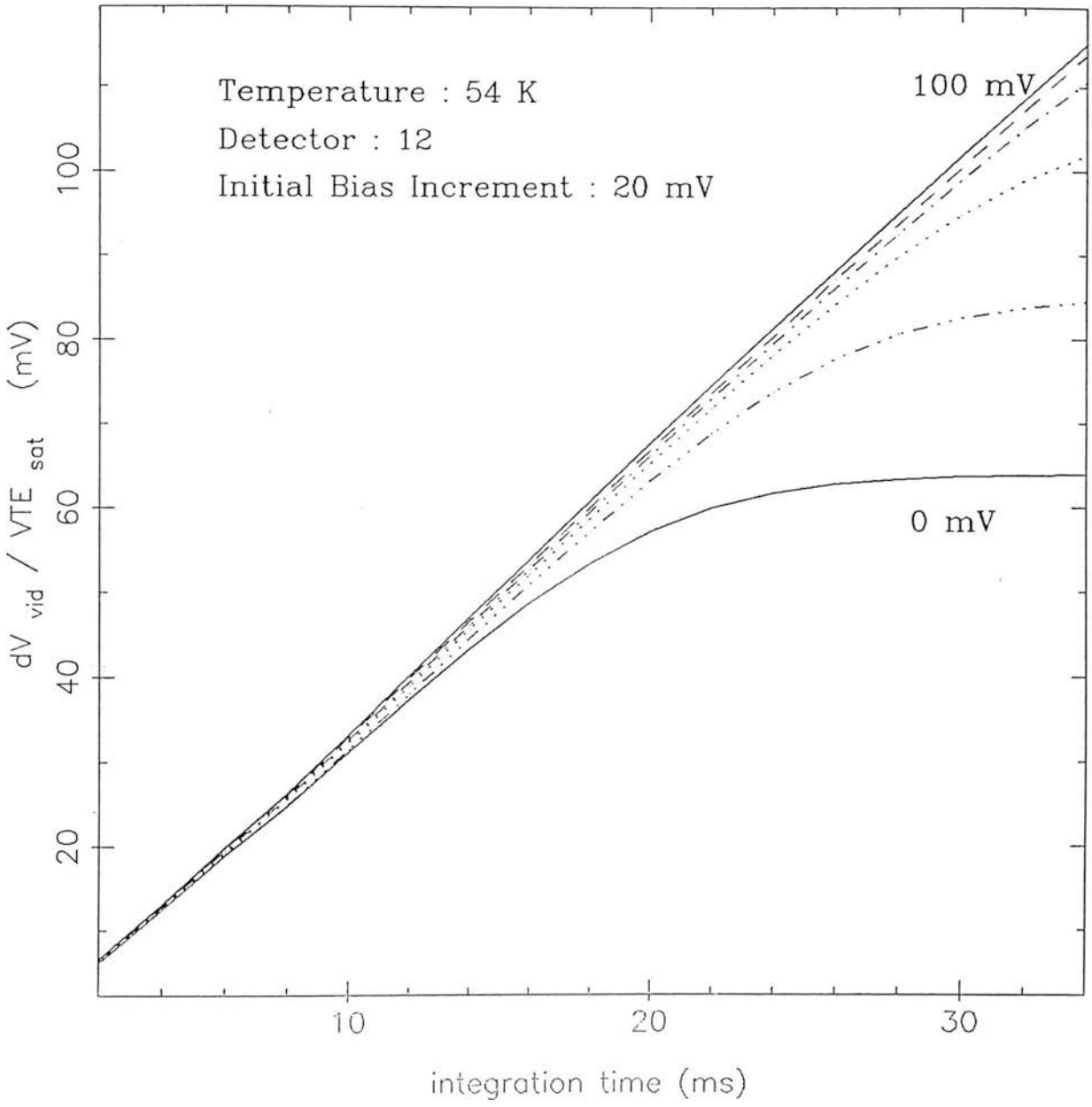

Figure 5.12 : Signal response to bright illuminating source.

than the CTE variation. This is because the final equilibrium state is the same in the two cases (V_f is equal), and the diode is at a single point on the I-V curve. This is a way of measuring the flux, since a larger flux will lead to a larger equilibrium dark current, displacing the diode to larger forward bias voltages.

5.4 Detector Capacitance - Upper Limit

An alternative means of measuring C_d to that described in section 5.2.1 is simply to calculate the number of photons incident on a detector and compare this with the output signal. If t_i and qe are known, and the voltage change at the detector can be inferred, then C_d can be calculated.

Using the set-up shown in figure 4.7, in the same arrangement used for the spot scanning experiment, and, assuming that the spot falls wholly within the area of a single detector, then the detection rate from the black body (ϵ=1) is;

$$N_{det} = A_{BB}.\Omega_{BB} \int_0^\infty \eta_{lens}(\lambda).\eta_{filter}(\lambda).qe(\lambda).BB\ (350\ ^\circ C,\lambda)\ d\lambda \quad el/s$$

$$BB\ (T,\lambda) = \frac{\lambda}{hc} \cdot L_\lambda\ (T)$$

The mean efficiencies adopted were, η_{lens}=0.9, η_{filter}=0.8 and qe=0.8, with the integral taken between λ=2.08μm and λ=2.37μm. This gives a detection rate of 1.5×10^8 el/sec.

The main uncertainty in this value is the transmission of the K filter, which was derived from a filter profile, of +/- 10%, and also an error introduced by the spot spilling over.

The background was measured by using a blank aperture at the black body, which is at room temperature (and for the same A.Ω product gives a detection rate of 1×10^3 el/sec). No other changes were made.

Similar results were obtained for three different pixels. The discharge

rates, at the detector, were measured to be 1.6 V/sec (BB plus background) and 0.9 V/sec (background). The high background is due to the large field of view, relative to the black body aperture, over which the detector sees room temperature emission.

Assuming that C_d is constant and there is negligible dark current, then the detector capacitance is given by;

$$C_d = q.N_{det} \left[\left. \frac{dV_d}{dt} \right|_{BB} - \left. \frac{dV_d}{dt} \right|_{Back.} \right]^{-1}$$

From this equation it can be seen that, if any of the black body flux is lost along the optical path (for example, if the spot over-spills), then the capacitance will be over-estimated. This method will therefore give an upper limit. The difference in the discharge rates implies a value for the detector capacitance of 34 pF.

5.5 Dark Current Behaviour

The detector dark current was investigated with the FOV restricted to the cold mounting directly over the detector, so that the background radiation was extremely low (<200 photons/sec at 80K, $<10^{-4}$ at 55K).

The method used was to accurately measure the detector discharge over a range of temperatures, but at the same initial bias ($\approx$ -60 mV $\equiv$ $5x10^6$ electrons), for a single pixel.

A typical dark response (figure 5.13), taken at 54K, saturated the detector in one and a half minutes. As can be seen the discharge rate is initially rapid, decreasing as zero voltage is approached. From figure 5.14, the normalised dark response appears very similar for the whole temperature range, suggesting that the I-V form remains constant.

All the dark current data were reduced in the following way;

(i) Each signal curve was expressed in terms of detector voltage, by dividing by the system gain. The t=0 offset was removed by fitting the first few points (typically three).

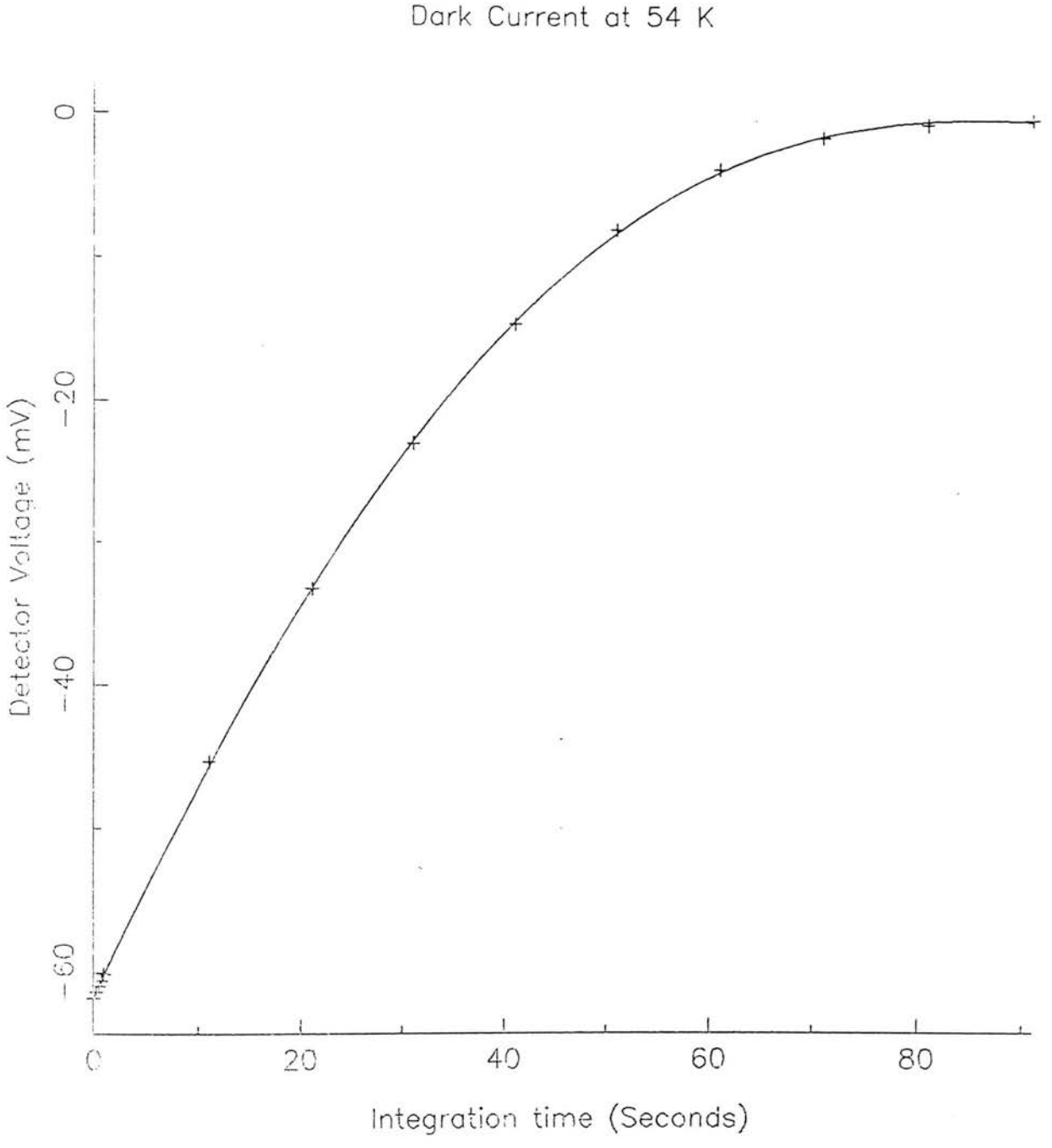
Dark Current at 54 K
Detector Voltage (mV)
0
-20
-40
-60
0
20
40
60
80
Integration time (Seconds)

Figure 5.13

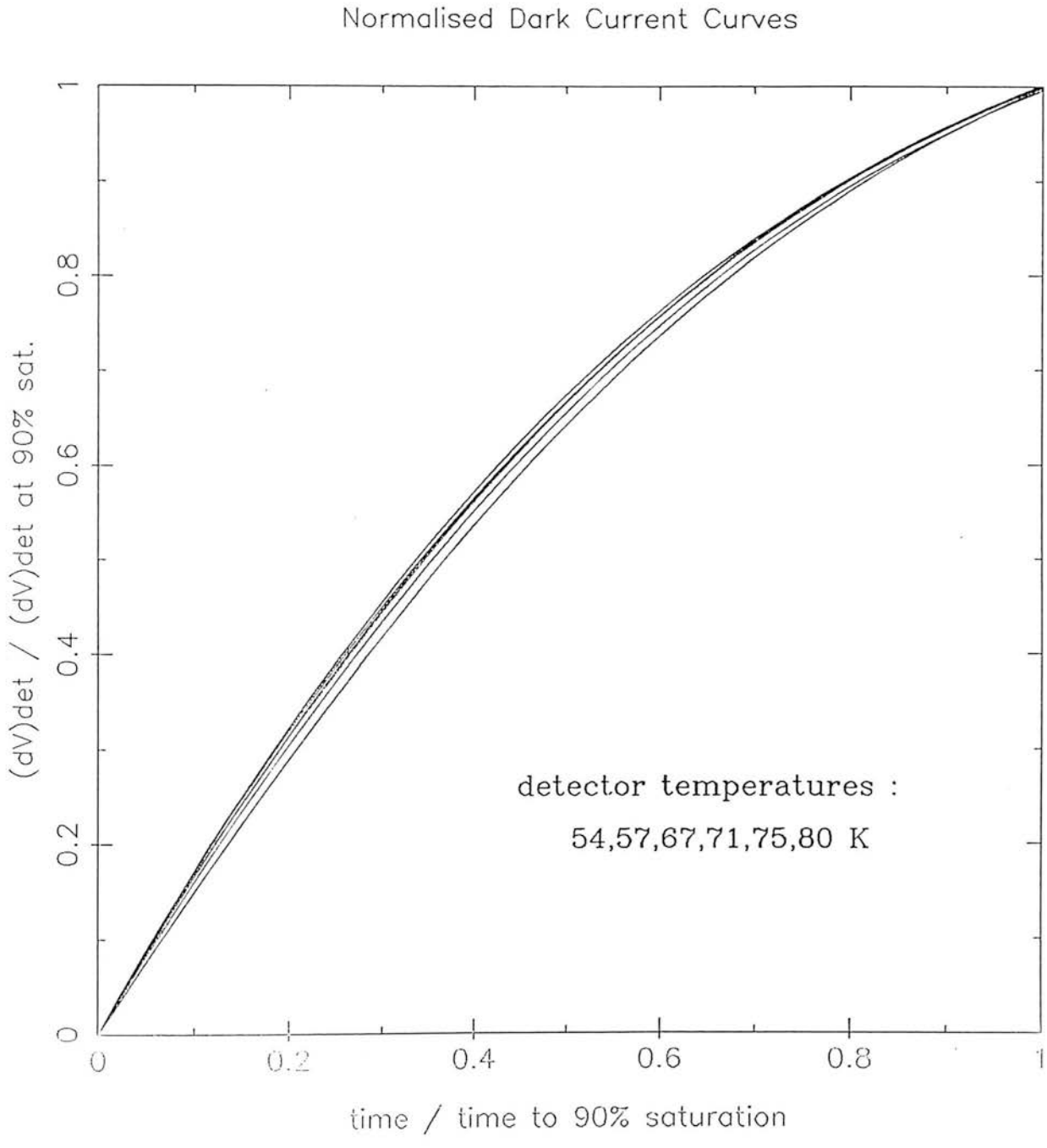
Normalised Dark Current Curves
(dV)det / (dV)det at 90% sat.
time / time to 90% saturation
0
0.2
0.4
0.6
0.8
1
detector temperatures :
54,57,67,71,75,80 K

Figure 5.14

(ii) The data were fitted, outside the saturation region, with a polynomial of degree three or four (giving rms residuals of ≈0.1-0.2mV, compared with typical mean errors in the data of 0.01-0.1mV).

(iii) The fitted curve was then differentiated to obtain dV_d/dt as a function of t_i. Since, as has been demonstrated, the response to detector charge is very linear, this is proportional to the detector current. The constant of proportionality being the detector capacitance. Since the detector voltage is derived from the quantity $\Delta V_v/VTE_{sat}$ and, at saturation, equations 3.5 and 3.8 can be combined to give

$$\frac{VTE_{sat}}{CTE_{sat}} = C_d(V_i) ,$$

the dark current is given by;

$$I_d = \frac{d}{dt}\left[\frac{\Delta V_v}{CTE_{sat}} \right] = C_d(V_i) . \frac{dV_d}{dt}$$

For these tests, therefore, $C_d \approx 13$ pF.

(iv) The $I_d(t)$ values were then matched up with the $V_d(t)$ values from the original fit, to give the I-V response.

The results of this procedure are shown in figure 5.15, for a temperature of 54K. The I-V curve is not accurate close to V_d=0 because of detector saturation, which prevents I_d from becoming positive, as well as errors in the detector voltage at this point (ie. if the bias offset is not calculated correctly). A way of getting a smooth transition through V=0,I=0 is to force the detector into the forward bias region by illuminating it (see section 6.1).

The detector impedance is given by;

$$R(V_d) = \left[\frac{dI_d(V_d)}{dV_d} \right]^{-1}$$

R_o was derived by extrapolating to V_d=0. The form of the $R_o.A(T)$ dependence is shown in figure 5.16. Also shown is R(-30mV).A. The R_oA value at 77K agrees reasonably well with previous data (Wimmers, 1983),

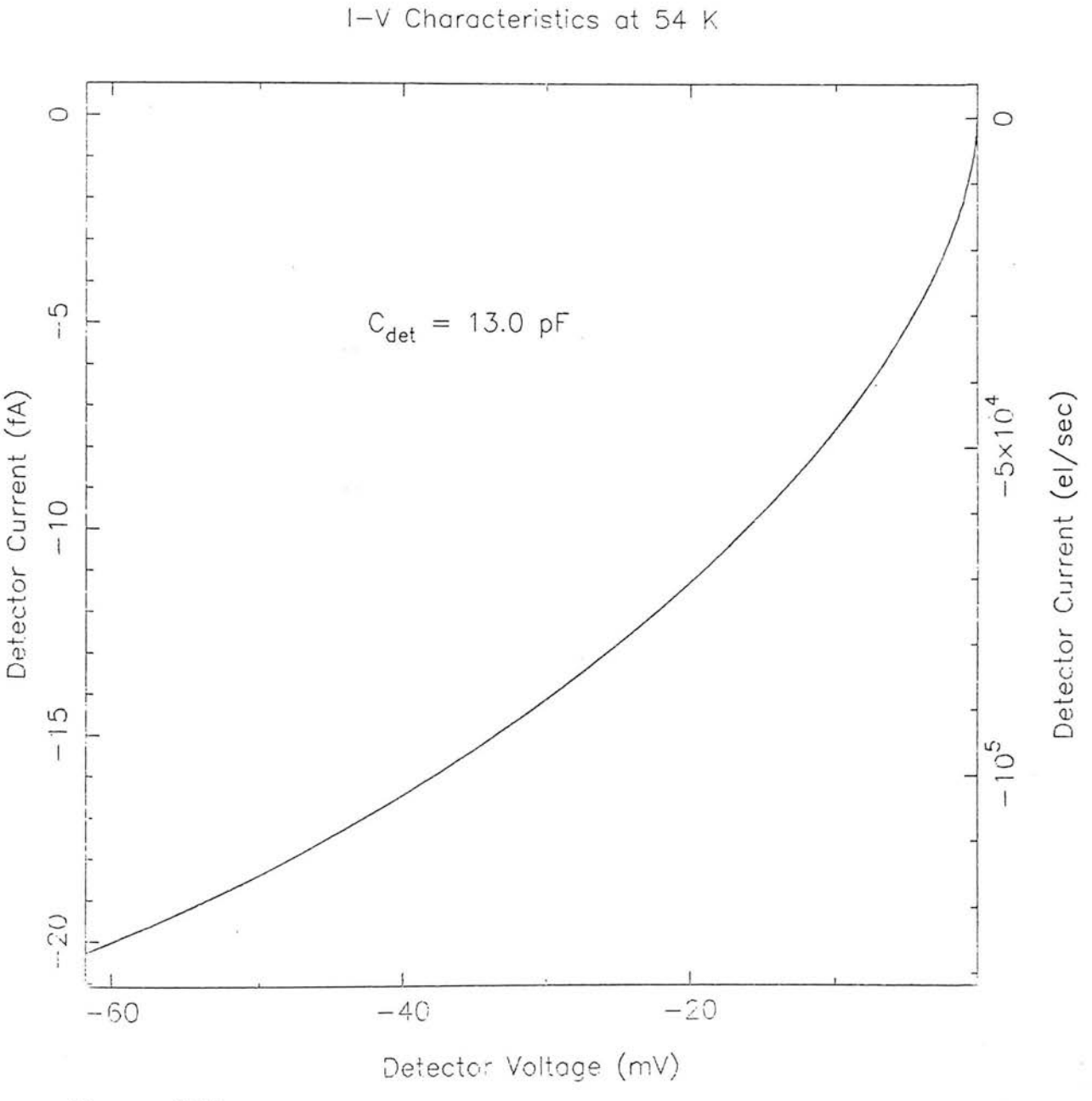
I–V Characteristics at 54 K
C_{det} = 13.0 pF
Detector Current (fA)
0
-5
-10
-15
-20
Detector Current (el/sec)
0
-5×10^4
-10^5
-60
-40
-20
Detector Voltage (mV)

Figure 5.15

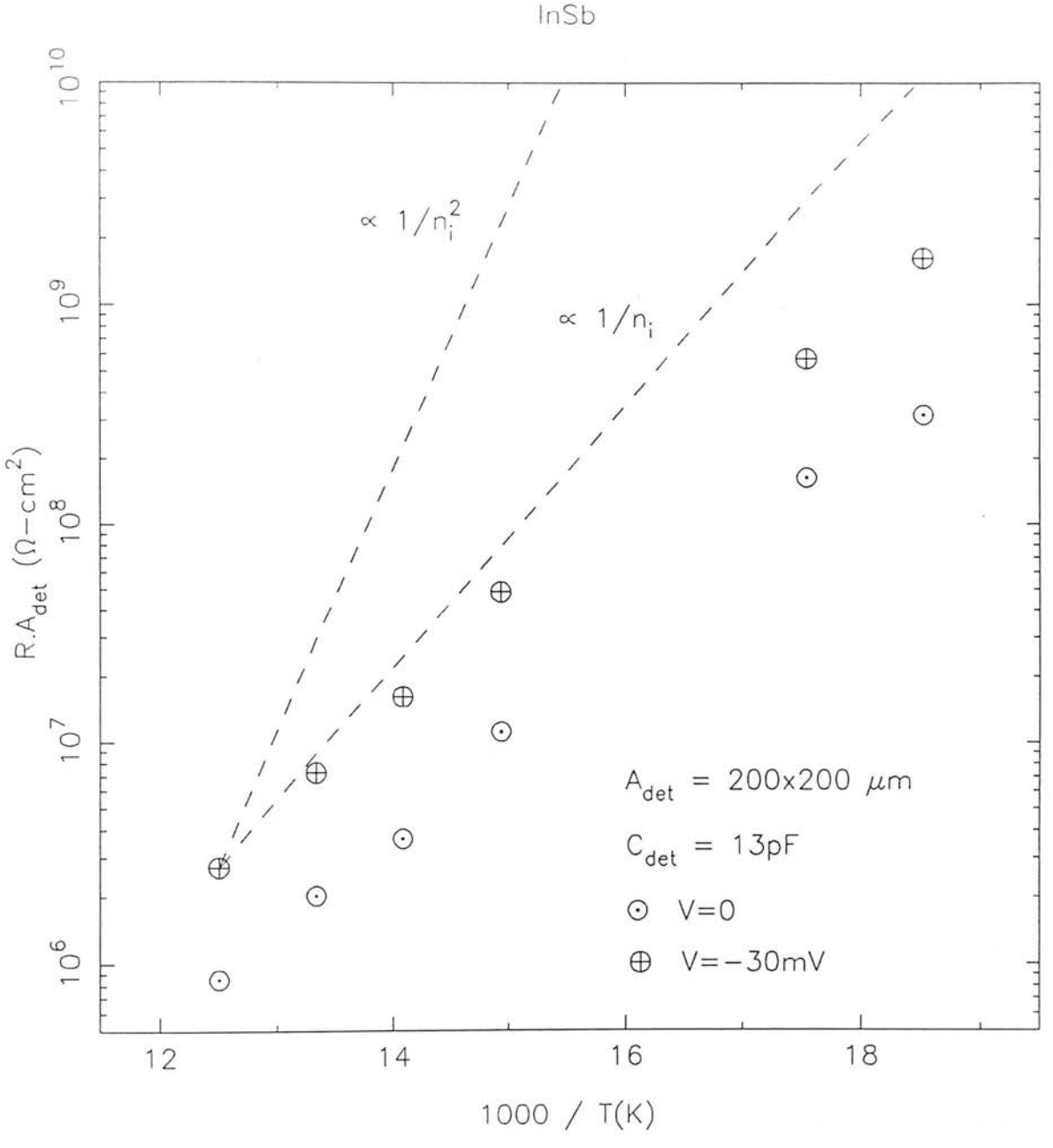

Figure 5.16 : Measured R.A temperature variation.

but, as can be seen, the temperature variation does not follow the g-r line ($\propto 1/n_i$). This could be due to errors in the assumed values of the capacitance or the initial bias, which have an effect on the form of the I-V curve. It is also possible that there is another current mechanism present (for instance, a parallel ohmic resistance could offset the resistance increase expected from g-r current).

The fall in dark current with decreasing temperature in this region (54-80K) is approximately exponential, so that the temperature drop which leads to a factor of two reduction in I_d, $\Delta T_{1/2}$, can be measured. The accuracy is dependent on the variation of C_d with temperature, which is not large, and the VTE non-linearity. Around 80K, $\Delta T_{1/2}$=3.3K and at 55K, $\Delta T_{1/2}$=2.0K. Extrapolated to 35K, this implies dark current as low as 10^3 el/sec and very large integration times (up to 1 1/2 hours). In practice, it is likely that below 40K surface effects (and possibly tunneling) will begin to dominate the dark current, so that the fall off will not be as dramatic as predicted.

The true I-V response was derived using the 80K data. Two corrections were applied; Firstly, the detector voltage scale was multiplied by a scaling factor, to allow for the true internal bias, and the current was obtained by differentiating this curve. Secondly, the detector voltage was multiplied by an additional factor, $VTE_{sat}/VTE(\Delta V_d)$, which was derived from the theoretical response and corrects for the VTE variation.

The resultant curve is shown in figure 5.17. For comparison, the g-r current (equation 2.3) for two values of V_{bi} is shown. There is quite a discrepancy between the curve and the expected response (V_{bi}=-160mV, see section 3.1.1). Again, this could be due to an additional current mechanism, or possibly errors involved in working back from the JFET output to the detector. This, perhaps, illustrates the difficulties in obtaining intrinsic detector characteristics when the device is 'hidden' in a switched-readout circuit.

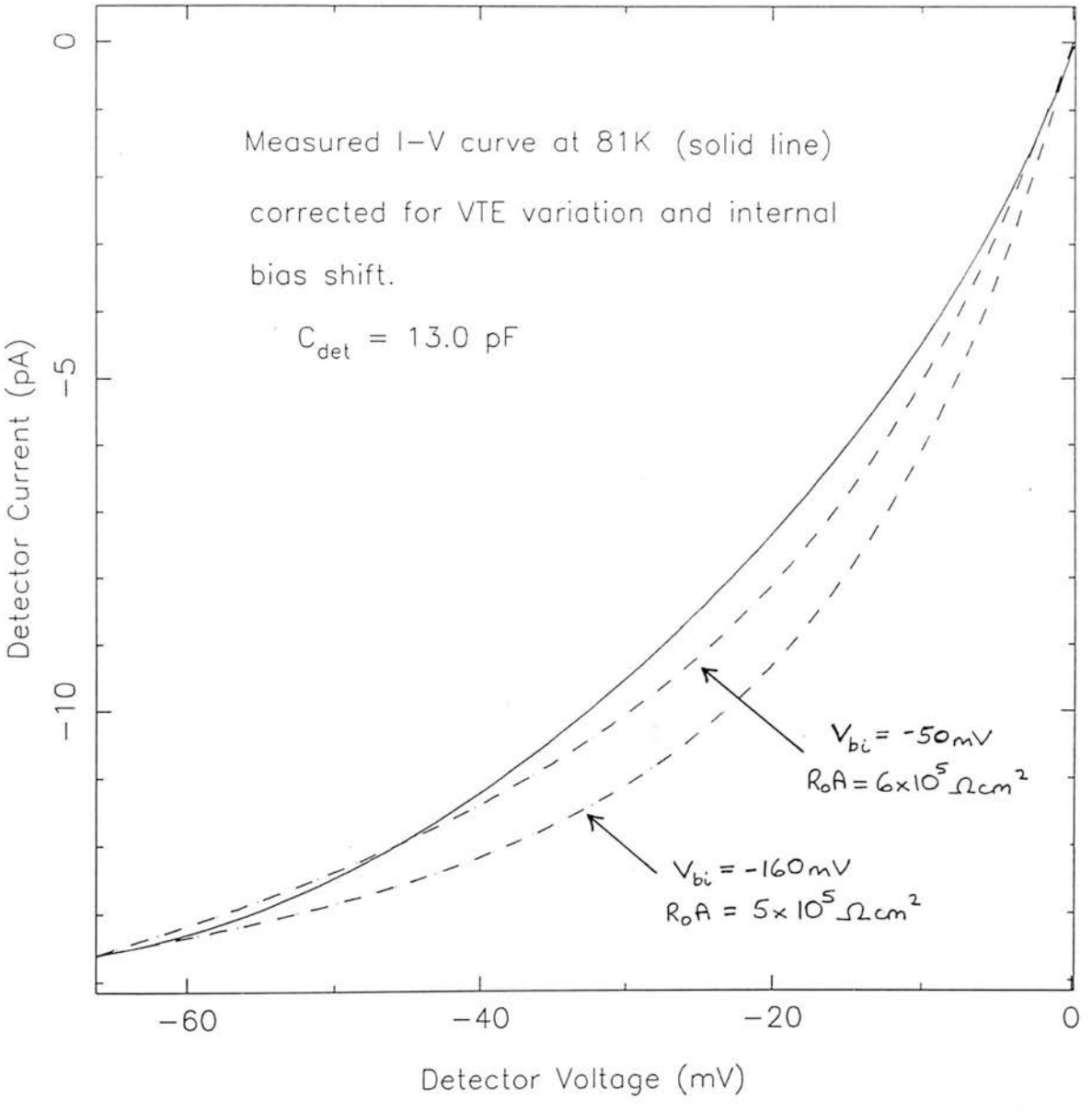

Figure 5.17
Detector I-V curve at 81K with two g-r current curves for comparison.

The maximum integration times which can be achieved with these detectors, derived from the discharge data, are shown in figure 5.18. There is a rapid increase in the available integration time for a relatively small drop in detector temperature, and this trend is controlled by the value of $\Delta T_{1/2}$ mentioned above.

The potential integration time also increases with increasing reverse bias since, although the initial dark current is greater, the detector follows the same I-V curve as it discharges and therefore has further to go to reach zero bias.

The advantages of long integration times for spectroscopy have already been described; whether they are employed will depend on the stability of the background flux and that of the system electronics.

Forward bias I-V data was obtained at 55K using data obtained from illuminated pixels. If it is assumed that the CTE variation is a smooth continuation from reverse to forward polarity (see response curve of figure 5.10) which is probably true for small forward voltages, then the response curves can be fitted and differentiated as before to give the current. The results from four signal curves at different flux levels, and low initial bias, are shown in figure 5.19, and appear very similar.

For C_d=13pF, the current at +60mV is 13.0 +/- 1.4 pA, which is six hundred times larger than the -60mV current. At 80K, this would correspond to 7nA.

The hot pixel was observed to have an approximately constant slope on an I-V plot (figure 5.20) suggesting leakage via an ohmic resistance (or short). Pixels fifteen and sixteen are shown for comparison.

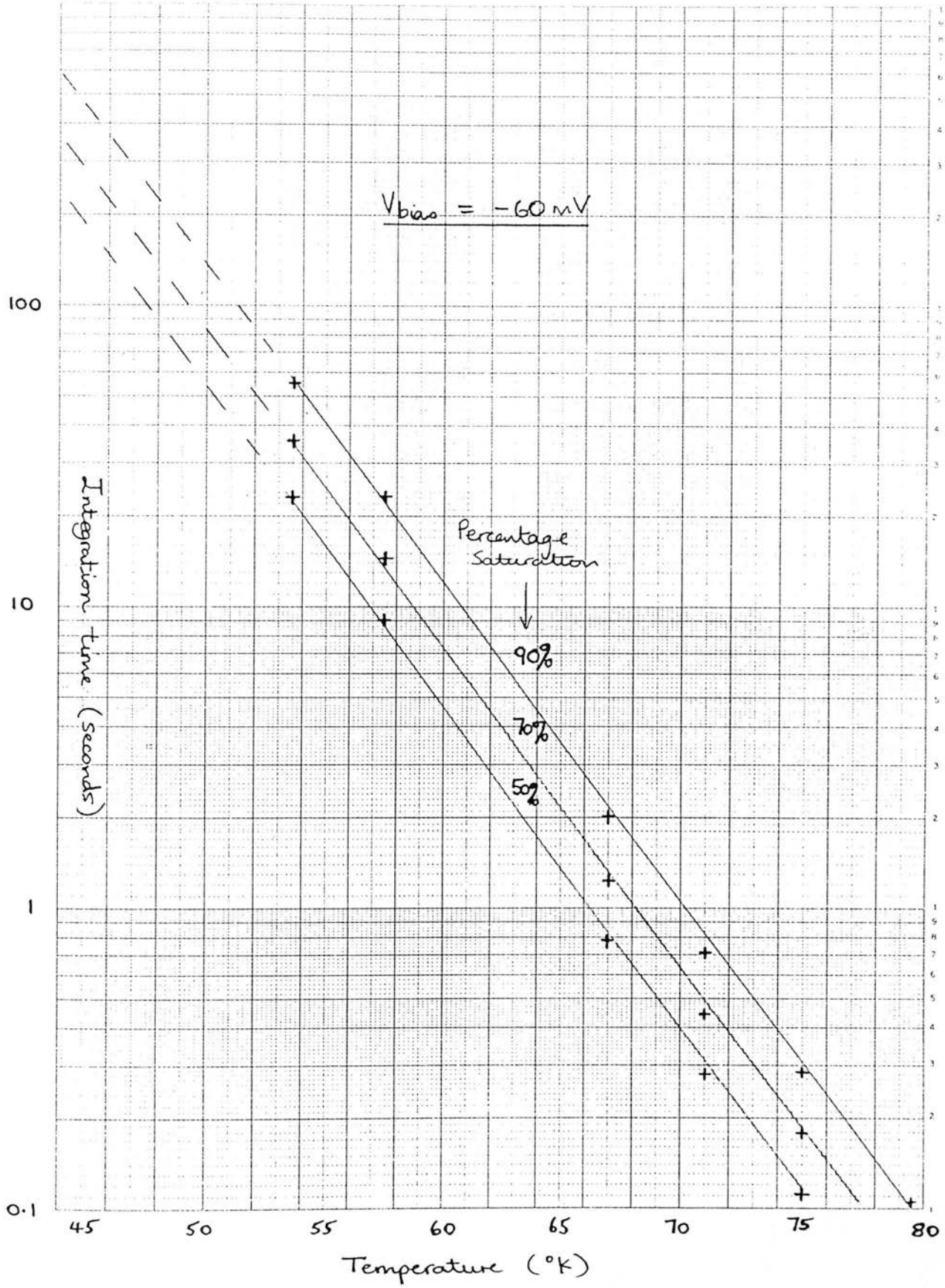

Figure 5.18
Potential on-chip integration times as a function of temperature and readout point.

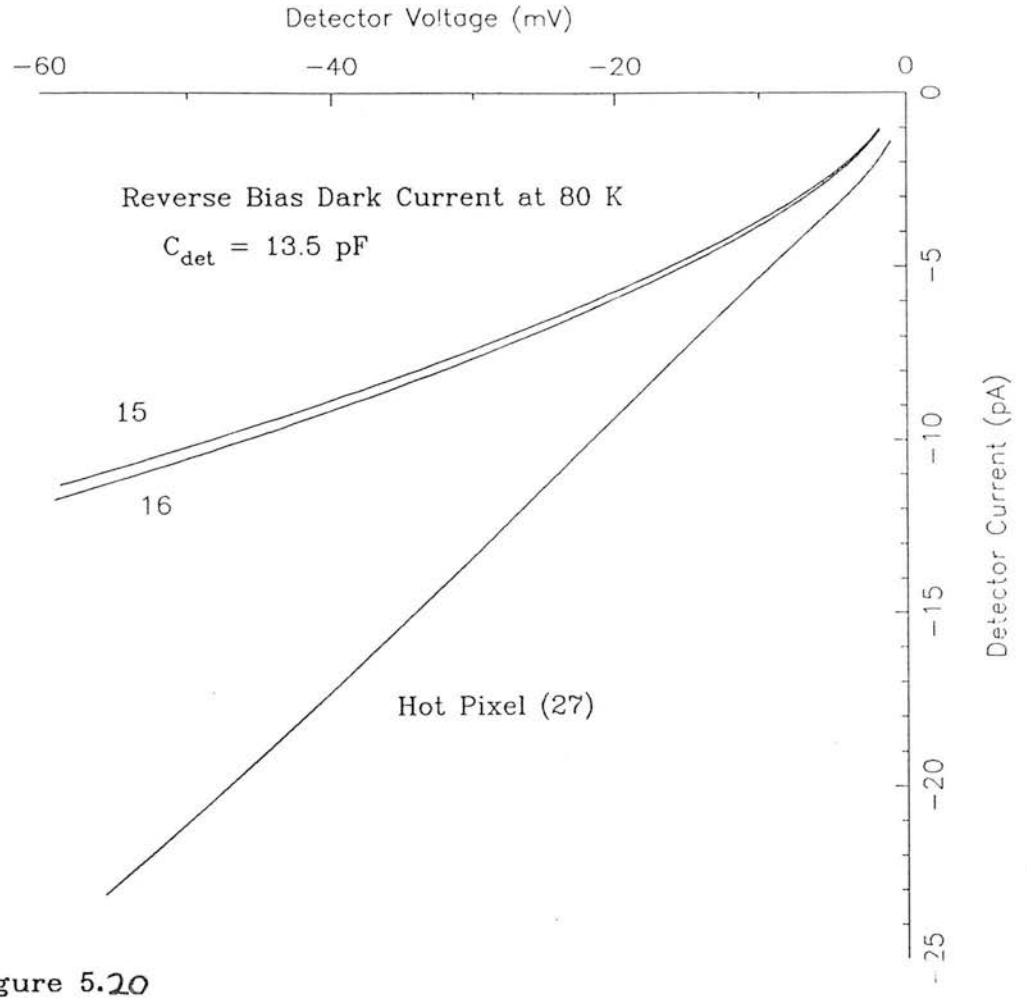

Figure 5.20

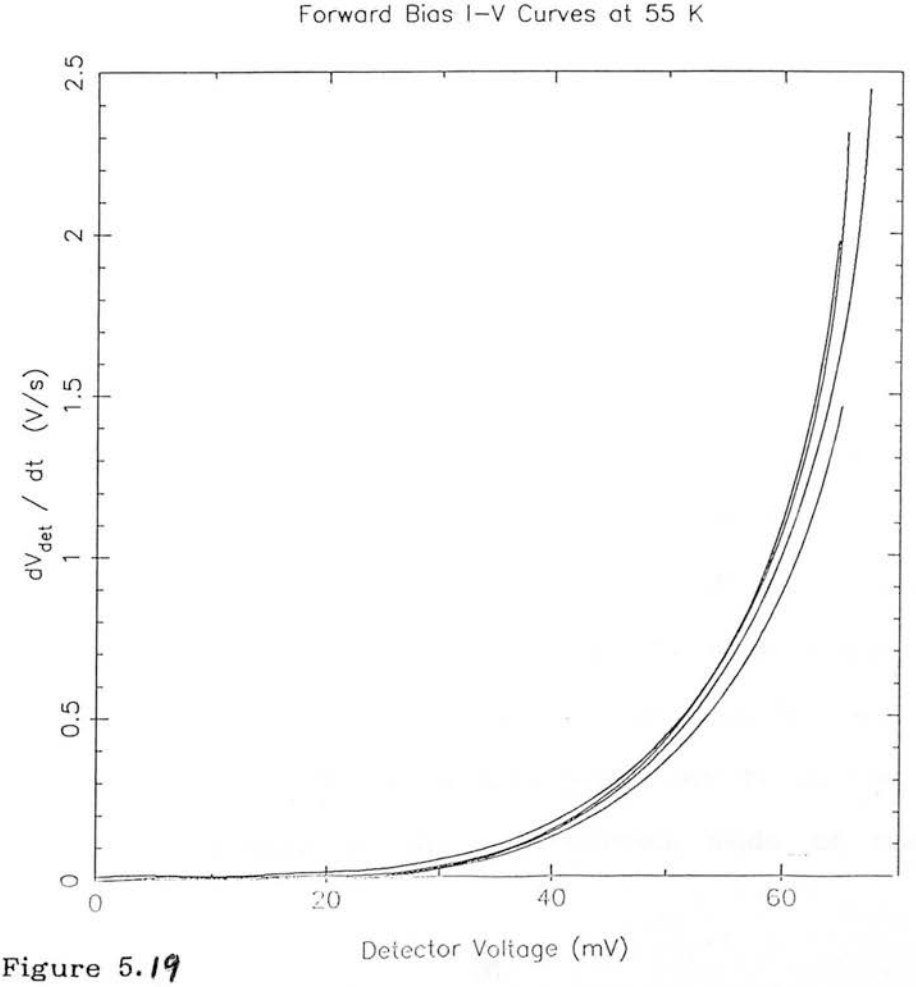

Figure 5.19

CHAPTER SIX

THE SIGNAL BEHAVIOUR OF INTEGRATING DETECTORS IN THE PRESENCE OF DARK CURRENT

Introduction

In a well baffled spectrometer, operating at high resolution and short wavelengths, the background can be so low that, even with the array cooled below 40K there may still be a significant dark current contribution, in addition to the photogenerated charge. The complicated interaction between these two processes has already been commented on. In order to investigate in detail how this influences signal response, and to test methods of extracting the photocurrent contribution, a single pixel was illuminated with the array at a temperature of 81K.

6.1 Illumination Tests at 81K

Pixel fifteen was used for this experiment (pixel sixteen, when compared, gave a nearly identical response), which involved obtaining the variation of discharge with integration time for six flux levels, and a constant initial bias. The signal curves are shown in figure 6.1. As can be seen, the presence of dark current introduces curvature into the signal response, which is greatest at the lowest illumination level. Four of the curves were followed to saturation (not shown in figure).

In order to display the detector current-voltage relation, the data were reduced in the same way as the dark current data of section 5.5, and the results are shown in figure 6.2a. Each curve has the form of the dark I-V characteristic, translated in the current direction by an amount equal to the photocurrent, which is a constant for each curve.

Since the dark current is zero at zero bias, the flux level, which is directly proportional to dV_d/dt at this point, can be derived from the figure. This corresponds to the short-circuit mode of operation of

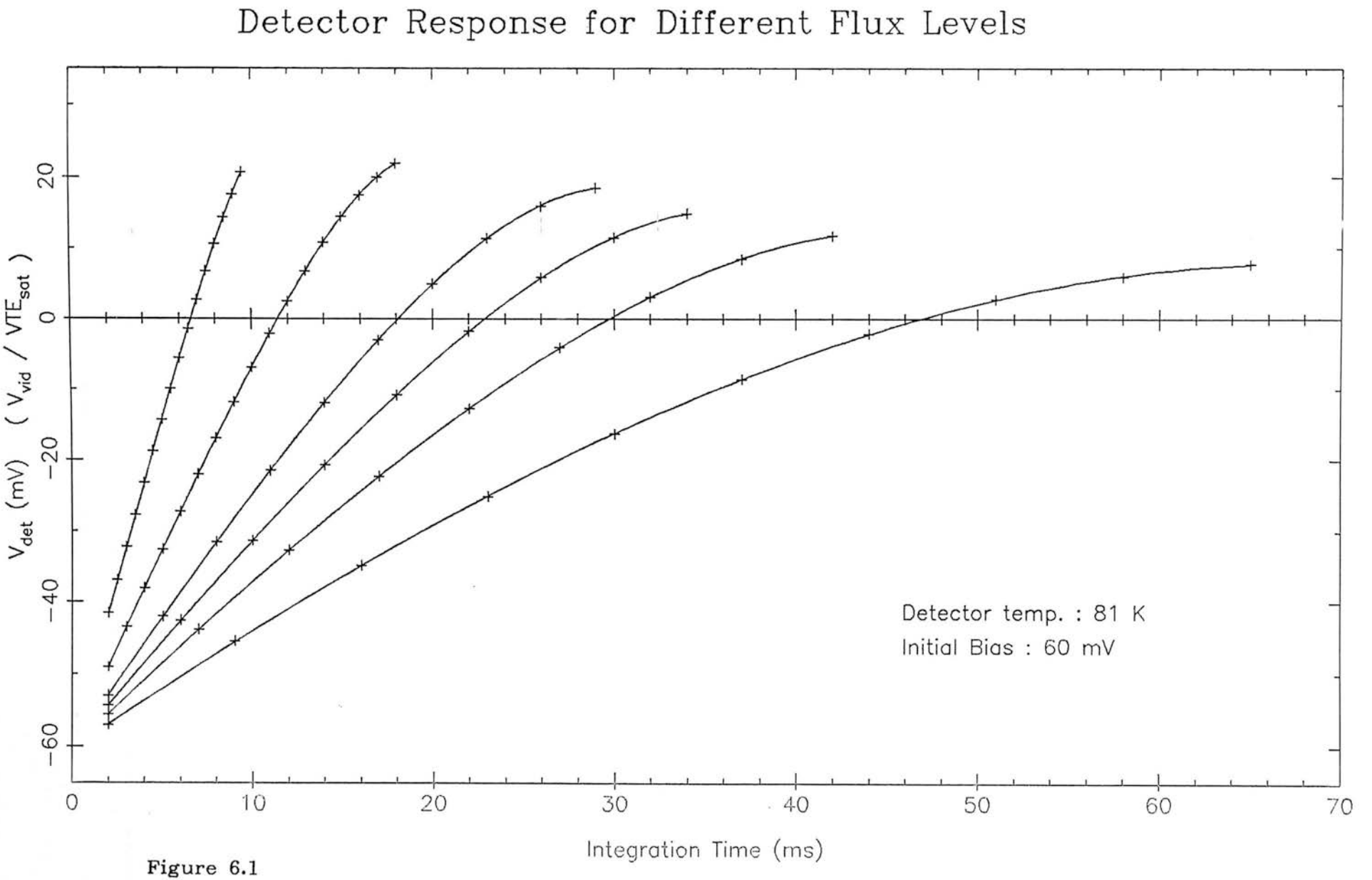
Detector Response for Different Flux Levels
V_{det} (mV) (V_{vid} / VTE_{sat})
20
0
−20
−40
−60
0
10
20
30
40
50
60
70
Integration Time (ms)
Detector temp. : 81 K
Initial Bias : 60 mV

Figure 6.1

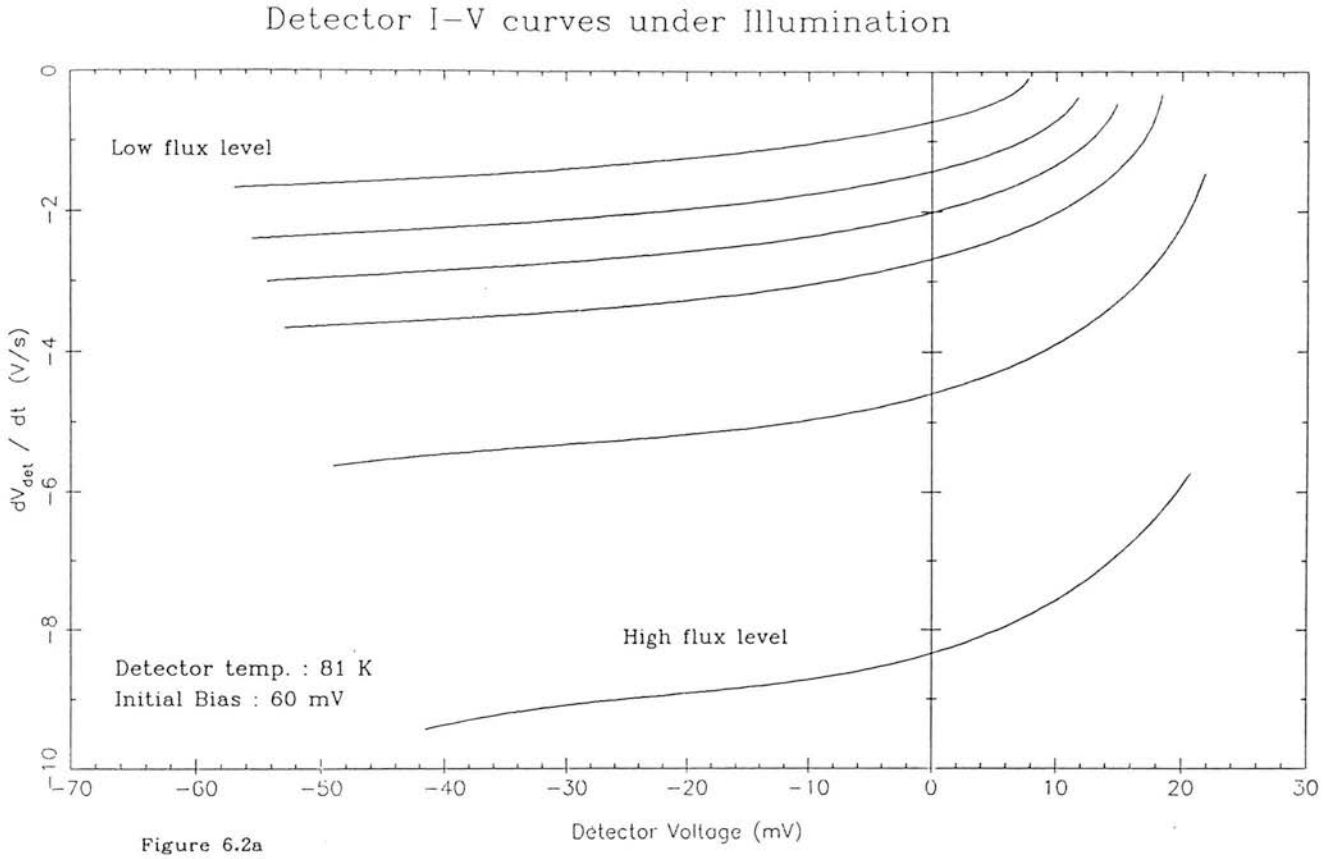

Figure 6.2a

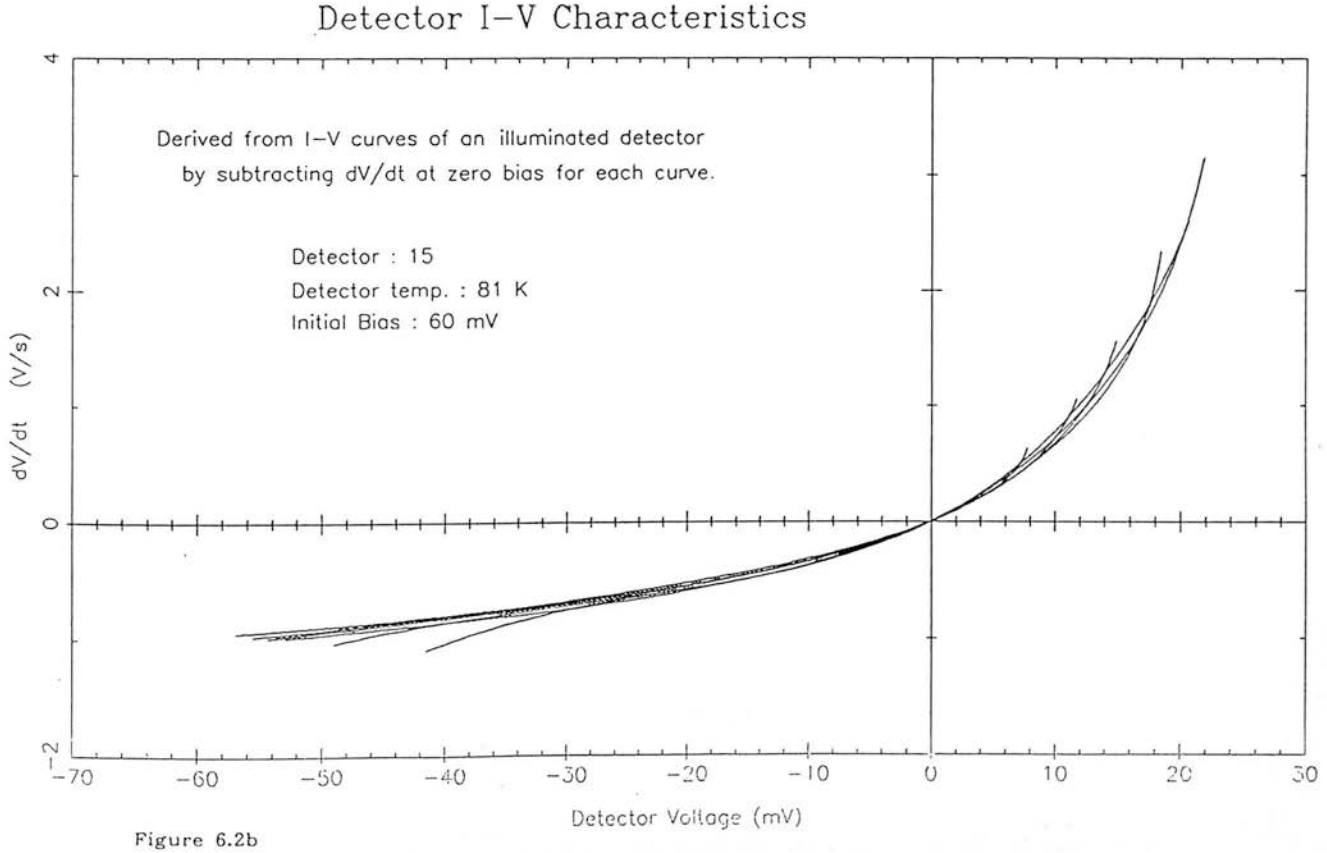

Figure 6.2b

non-integrating PV detectors.

By stacking the curves so that each passes through the point V=0,I=0 (figure 6.2b), the similarity of the I-V response, in each instance, is demonstrated. The discrepancies are due to poor fitting at the ends of the signal curves.

The saturation level was measured for the four lowest fluxes. At this point, the total detector current is zero (which is the maximum, ie. most positive, current that can be obtained from a reverse biased integrating detector), and the photocurrent is thus equal and opposite to the dark current. This is similar to the open-circuit operation of a PV detector. As expected, the saturation voltage gives a non-linear measure of relative flux level, due to the exponential relationship between forward bias voltage and current.

Table 6.1 lists the initial results from the I-V analysis. The ratio of detected flux to initial dark current, Φ/I_{d0} (where both quantities are measured in terms of dV_d/dt, so that the ratio is dimensionless), was derived using the dark current data from section 5.5.

Table 6.1

Flux	$\lvert dV_d/dt \rvert$ at $V_d=0$ (V/sec)	Φ/I_{d0} [1]	V_d at saturation (mV)
#1	0.69 [2]	0.71	9.6
#2	1.39	1.43	14.7
#3	1.97	2.03	17.6
#4	2.63	2.71	20.5
#5	4.55	4.69	–
#6	8.28	8.54	–

1 I_{d0} = 12.6 pA (C_d=13 pF), therefore dV_d/dt = 0.97 V/sec

2 For qe=0.8, this flux corresponds to $\approx 7 \times 10^7$ photons/sec

6.2 Detector Calibration - First Attempt

Once Φ/I_{d0} is known it is possible to separate the signal into photo- and dark current components (assuming for the moment that the CTE is constant). This is shown for a single flux level (figure 6.3a) and the dark current contribution for each flux is shown in figure 6.3b.

As far as a simple dark current correction is concerned, this figure presents two results; Firstly, up to saturation (the peak of the curve where $I_d = -I_\Phi$), the dark current has a non-linear time dependence in each case. This means that a correction which involves measuring the initial dark current, I_{d0}, and then subtracting an amount $I_{d0}.t_i$ from the signal, will be ineffective. Secondly, it is obvious that the dark contribution is a strong function of the illumination level. Thus a correction using the signal from a dark (blanked off) discharge for the same integration time, would also give incorrect results.

These two corrections are mentioned because they are frequently used for optical CCDs.

What is required is a method which takes account of the initial and final detector states, as well as t_i, and uses this information to derive an average dark current for the exposure. This quantity can be derived in the following way;

Since the CTE non-linearity is small, the rate of change of the output signal with time is proportional to the rate of change of detector charge (from equation 3.7). This is given by the sum of the dark current, I_d, which is a function of detector voltage (and therefore time, t), and the photocurrent, I_Φ;

$$\frac{dS}{dt} \propto I_d(t) + I_\Phi \qquad (6.1)$$

The signal change, ΔS, in an integration of duration t_i is;

$$\Delta S(t_i) \propto \int_0^{t_i} I_d(t)\, dt + I_\Phi.t_i \qquad (6.2)$$

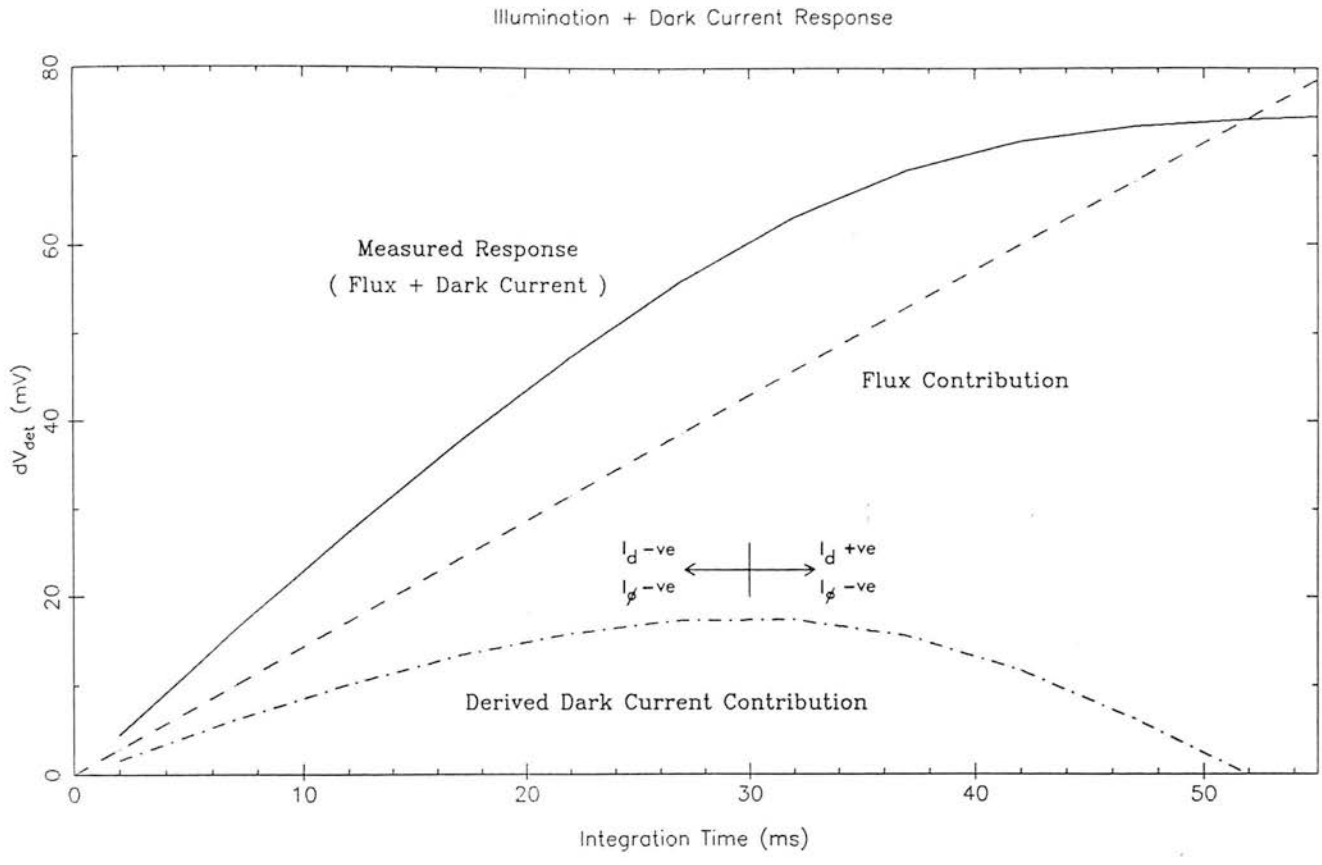

Figure 6.3a

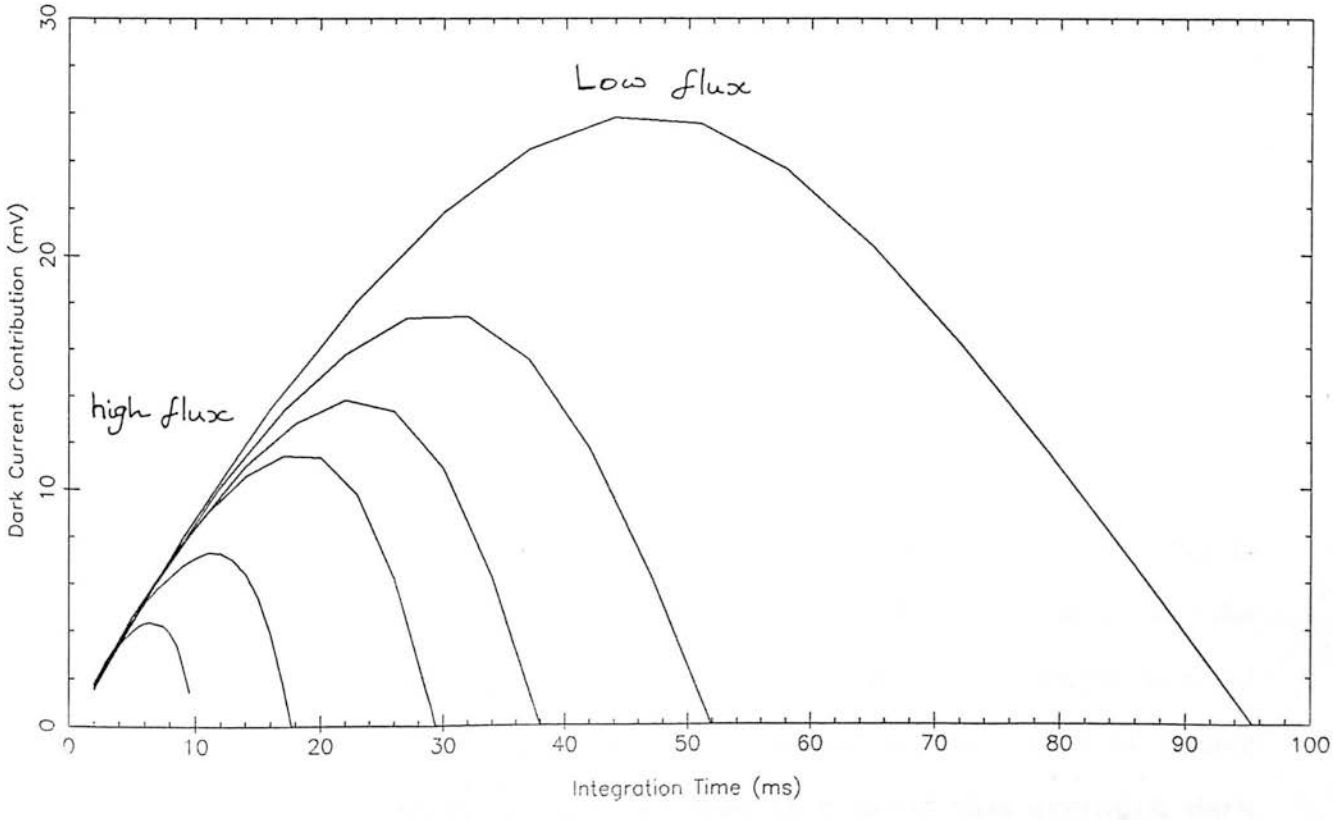

Figure 6.3b : Dark current contributions.

If we assume that the detector voltage approaches zero bias uniformly with time (from figure 6.1, this becomes true for larger fluxes), then;

$$\int_0^{t_i} I_d(t)\, dt \;=\; \frac{t_i}{V_f - V_i} \int_{V_i}^{V_f} I_d(V)\, dV \;=\; \overline{I_d(V_i, V_f)}.t_i$$

The mean dark current (dc) between initial and final states is related to the output signal by;

$$\overline{\left[\frac{dS}{dt}\right]_{dc}} \;=\; A_s \cdot \overline{\left[\frac{dV_d}{dt}\right]_{dc}} \;=\; \frac{A_s}{C_d} \cdot \overline{I_d(V_i, V_f)} \qquad (6.3)$$

The variation of the mean dark current as a function of V_f is shown in figure 6.4, which was derived from 81K dark current data at an initial bias of -61mV.

Finally, by combining equations 6.2 and 6.3, the photon contribution to the signal, ΔS_ϕ, can be found;

$$\Delta S_\phi \;=\; \Delta S(t_i) \;-\; \overline{\left[\frac{dS}{dt}\right]_{dc}} \cdot t_i \qquad (6.4)$$

For a fixed initial bias and temperature, the right-hand term could be derived using the actual signal output level together with a look-up table of a similar form to figure 6.4.

The accuracy of this method was tested by comparing the observed dark current with a discharge curve derived from equation 6.4, with ΔS_ϕ=0. This is a worst case situation, since for zero flux, the detector response has a maximum non-linearity. Figure 6.5a shows the result, from which it can be seen that the model predicts the dark current well up to about 50% saturation, but then diverges considerably. The reason for the subsequent over-estimate is that the detector spends a longer time at smaller reverse voltages where the dark current is small than at larger biases where the current is high, resulting in a lower time-averaged dark current than predicted by the model.

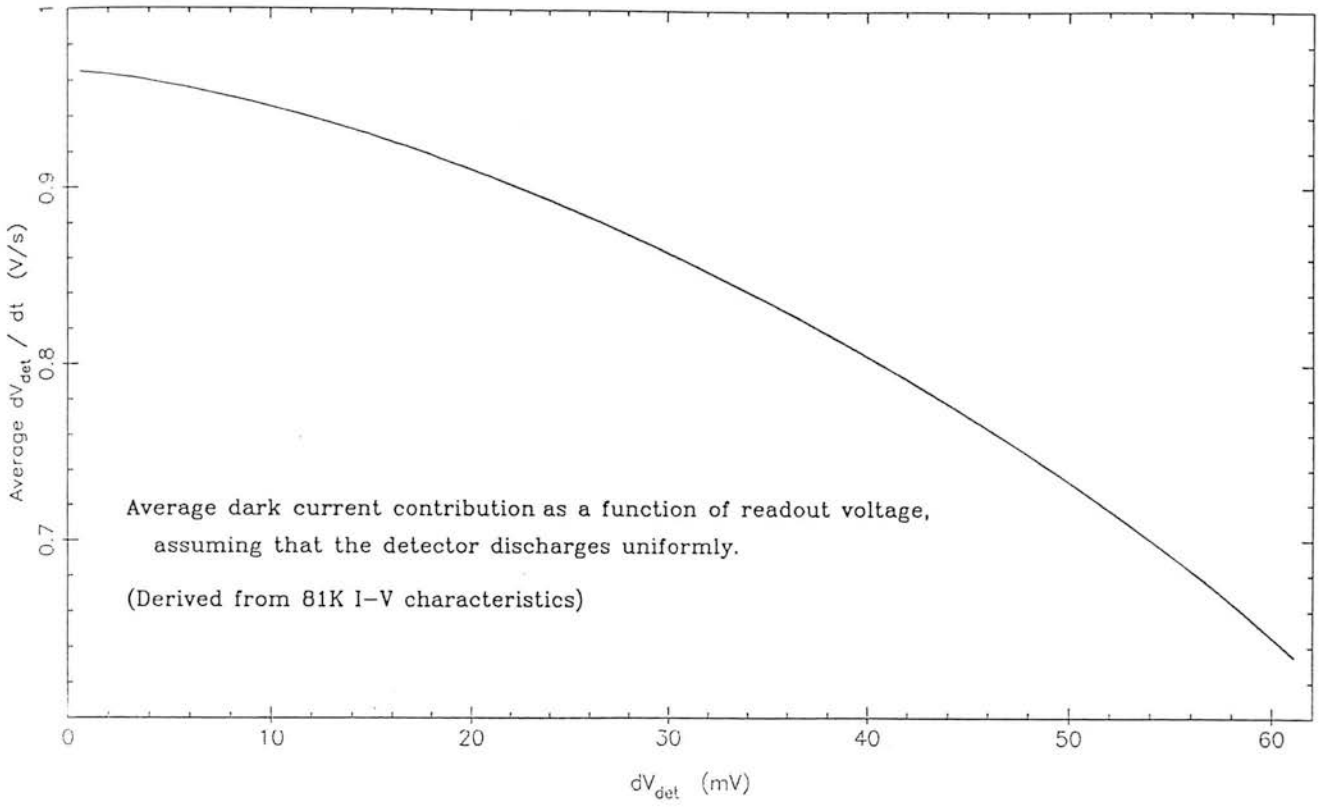

Figure 6.4

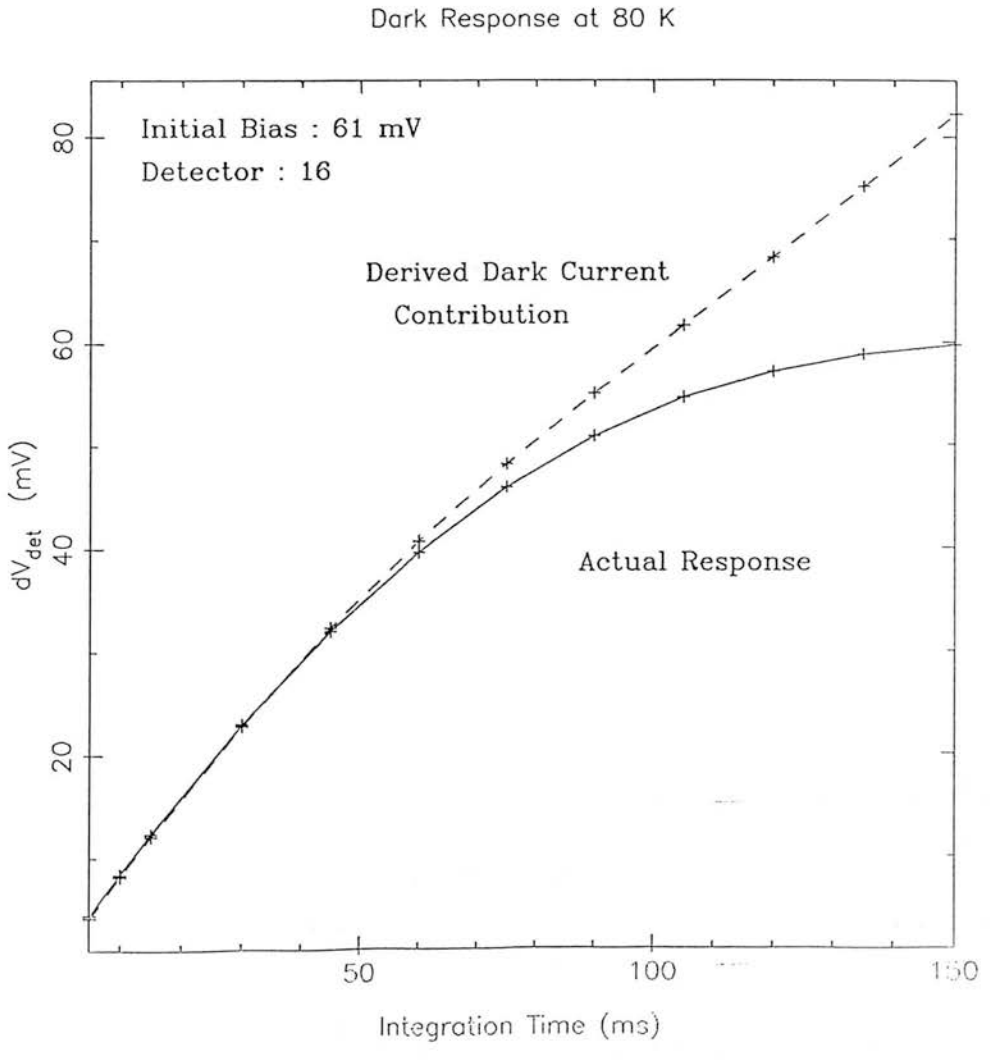

Figure 6.5a

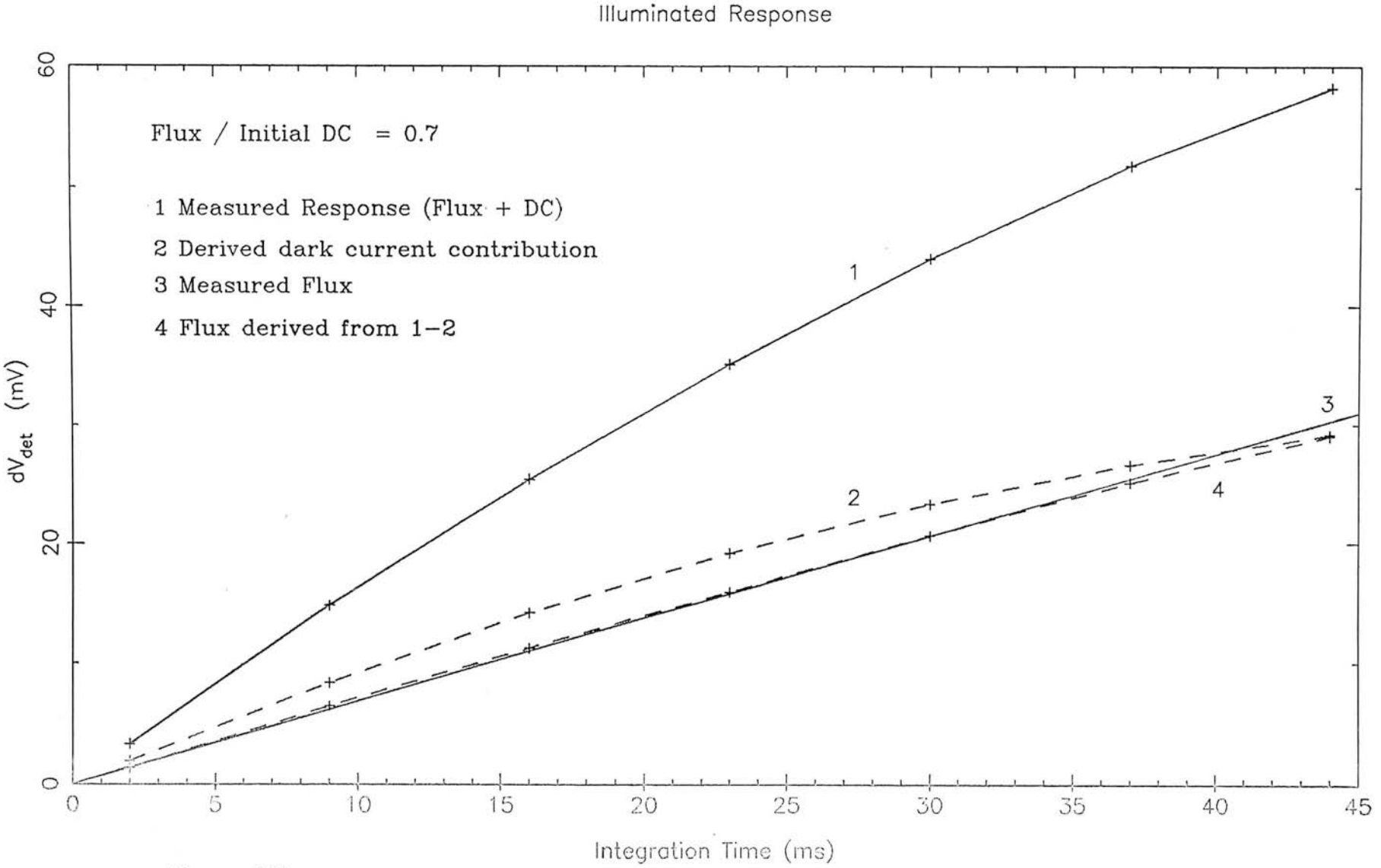
Illuminated Response
Flux / Initial DC = 0.7
1 Measured Response (Flux + DC)
2 Derived dark current contribution
3 Measured Flux
4 Flux derived from 1−2
dV_det (mV)
Integration Time (ms)
0
20
40
60
0
5
10
15
20
25
30
35
40
45
1
2
3
4

Figure 6.5b

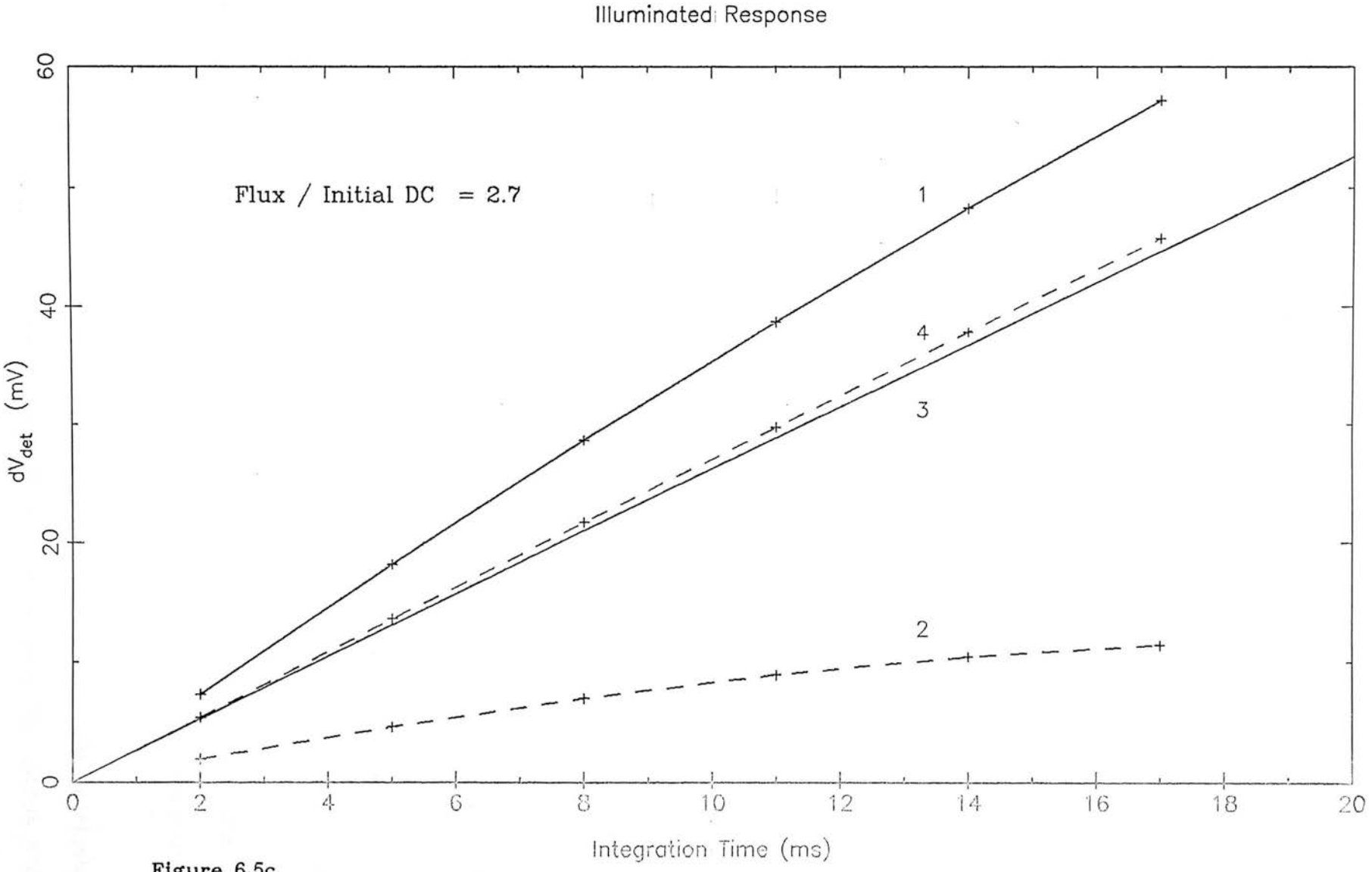
Illuminated Response
Flux / Initial DC = 2.7
1
2
3
4
dV_{det} (mV)
Integration Time (ms)
0
20
40
60
0
2
4
6
8
10
12
14
16
18
20

Figure 6.5c

Applying equation 6.4 to two of the illuminated response curves gave the results shown in figures 6.5 b,c. When the detected flux rate is less than the initial dark current, there is significant curvature in the derived photocurrent contribution, which leads to a 10% deviation from the initial slope.

For $\Phi/I_{d0}=2.7$, however, the derived flux contribution is reasonably linear. Note that there is a difference in the flux derived from the model and that given in table 6.1 of 3%. The majority of this discrepancy arises from an uncertainty in the position of the V=0 axis, which in turn is due to the uncertainty in the value of the initial bias.

The model was found to work effectively for $\Phi/I_{d0} \geqslant 2$, in that the error approaches the limiting error due to the CTE non-linearity.

The disadvantage of this model, however, is that it is only worthwhile applying it over a narrow illumination range. For $\Phi/I_{d0} \geqslant 10$, the dark current will be such a small fraction of the total signal that a simpler correction will be just as accurate.

6.3 Response of a Simple Integrating Detector

Dark current can have a strong influence on the response of integrating detectors. The purpose of this section is to study what effect this will have on how observations are made, for example, with an array spectrometer. Some insight to this problem can be gained by using a simple model for a detector, designed to behave in a similar manner to a 'real' device. In the next section these results will be compared with a method of correcting all the non-linear processes present in integrating arrays.

In the situation where an array is employed to measure the intrinsic brightness across the spectrum of an astronomical object, the output will consist of an array of signal levels derived from a constant integration time. The signal rate (ie. signal divided by t_i, and hence in units of

volts/second) measured for a single pixel, will be $R_O=k_O\eta(\lambda)\Phi_O(\lambda)$, where $\eta(\lambda)$ is the combined throughput of the atmosphere, telescope and instrument at the observing wavelength, Φ_O is the apparent object flux above the atmosphere, and k_O is the post-detection system gain. k_O includes contributions from the CTE and amplifier gains. To measure Φ_O, a calibration source is observed under similar conditions. For a broadband camera, the sky can be used, whereas in a high resolution spectrometer it may be too faint. Alternatively a bright star, whose spectral shape is known, can be used. The calibration signal rate will be $R_C=k_C\eta(\lambda)\Phi_C(\lambda)$. If, for some reason, $k_O \neq k_C$ there will be a fractional error in the derived relative flux, $R_O/R_C = k_O\Phi_O/k_C\Phi_C$, of $1 - k_O/k_C$ (cf. the definition of non-linearity).

At this stage the signals have not had the dark current subtracted (this will be considered shortly). Thus, if the signals are derived as above, the dark current will somehow be incorporated into the k values, since η and Φ are pre-determined. An obvious instance in which k_O will differ from k_C is where a faint object is observed with a large t_i, so that the dark charge is large. If, on the other hand, the calibration object is bright, and observed for a shorter t_i, there will be little dark charge influencing the value of k_C.

In order to investigate the behaviour of the gain term (ie. k_O or k_C) further, it is useful to simulate the detector signal response by assuming a simple form for the dark current. Firstly, consider a generalized form of equation 6.1;

$$\frac{dS}{dt} = h(S) + g(S).\Phi \qquad (6.5)$$

h(S) represents the dark current discharge rate, which is dependent only on the output signal (this is analogous to the I-V characteristic at the detector). $g(S).\Phi$ is the discharge rate resulting from a flux level Φ, and g(S) describes amplifier non-linearities as well as any CTE variation.

For the model, $g(S)=g$ is assumed to be constant (ie. linear) over the signal range.

A simple form for $h(S)$ is;

$$h(S) = I_{d0} \left(1 - S/S_{sat} \right) \qquad (6.6)$$

I_{d0} is the initial dark current and S_{sat} the saturation signal in the absence of illumination. This function implies a uniform drop in dark current with increasing output, until saturation is reached, when $h(S)=0$.

Substituting equation 6.6 into 6.5 and solving gives the time variation of the output signal as a function of the illumination and the initial dark current;

$$S(t) = S_{sat} \left(1 + \frac{g\Phi}{I_{d0}} \right) \left(1 - e^{-I_{d0} \cdot t/S_{sat}} \right) \qquad (6.7)$$

where t represents the on-chip integration time.

Even though $h(S)$ was chosen for its simplicity, the above form for $S(t)$ when $\Phi=0$, which is a decaying exponential approaching S_{sat} at large t, does resemble the observed data (cf. figure 5.13).

The post-detection gain is proportional to the change in output signal per unit change of input flux, which is given by;

$$\left. \frac{dS}{d\Phi} \right|_{const.t} = \frac{g.S_{sat}}{I_{d0}} \left(1 - e^{-I_{d0} \cdot t/S_{sat}} \right) \qquad (6.8)$$

In the region where illumination induced discharge dominates, $g\Phi >> I_{d0}$ and the integration time is $t \leqslant S_{sat}/g\Phi$. This gives the condition $I_{d0} \cdot t << S_{sat}$, so that equation 6.8 reduces to $dS/d\Phi \approx g.t$.

For convenience the effective gain, g', defined as the output signal per unit time per unit flux input, is set to unity in this region. Hence, $g' = 1/gt \; . \; dS/d\Phi$.

The quantities described at the beginning of the section, k_o and k_c, are directly proportional to the effective gain, g'.

The values of I_{d0} and S_{sat} are chosen arbitrarily, since they merely affect the time to reach a given discharge point, $x = S/S_{sat}$. Equation 6.8

can be simplified if t is substituted from equation 6.7, and is then expressed in terms of the effective gain. Further, setting g equal to I_{d0} will imply that a unit flux input will give rise to the same discharge rate as I_{d0}. The quantity $g\Phi/I_{d0} = \Phi$ is also a convenient measure of the relative amounts of illumination and dark current present. These considerations lead to the following form for the effective gain of the detector;

$$g' = - \frac{x}{1 + \Phi} \cdot \frac{1}{\log_e [1 - (x/(1+\Phi))]}$$

The variation of g' with Φ for three readout points is shown in figure 6.6, which shows that there is a drop in g' as the proportion of dark current increases (object becoming fainter), and also splitting in the region $\Phi<1$, according to the value of x.

Consequently, the error in the flux, derived by ratioing a faint object with a bright standard, can approach 50%, and the object's brightness will be under-estimated, since

$$R_o/R_c = g'_o/g'_c \cdot \Phi_o/\Phi_c < \Phi_o/\Phi_c.$$

Figure 6.7 shows the magnitude of the gain variation with x for $\Phi=10^{-3}$.

The photon gain, g, is constant; what is causing g' to vary is the influence of dark current, as this has not been removed from the signal. The problem is to subtract the correct amount of dark charge so that g' approaches g for all Φ and x.

Subtracting a dark frame at the same t will remove the offset term, $S(t,\Phi=0)$, but will not alter the perceived gain. Another alternative is to difference the faint object with an adjacent piece of empty sky. The gain terms will be approximately the same in each case, and the offsets will be removed, but the object flux will still be modified by the effective gain ($S=g'\Phi_o t$).

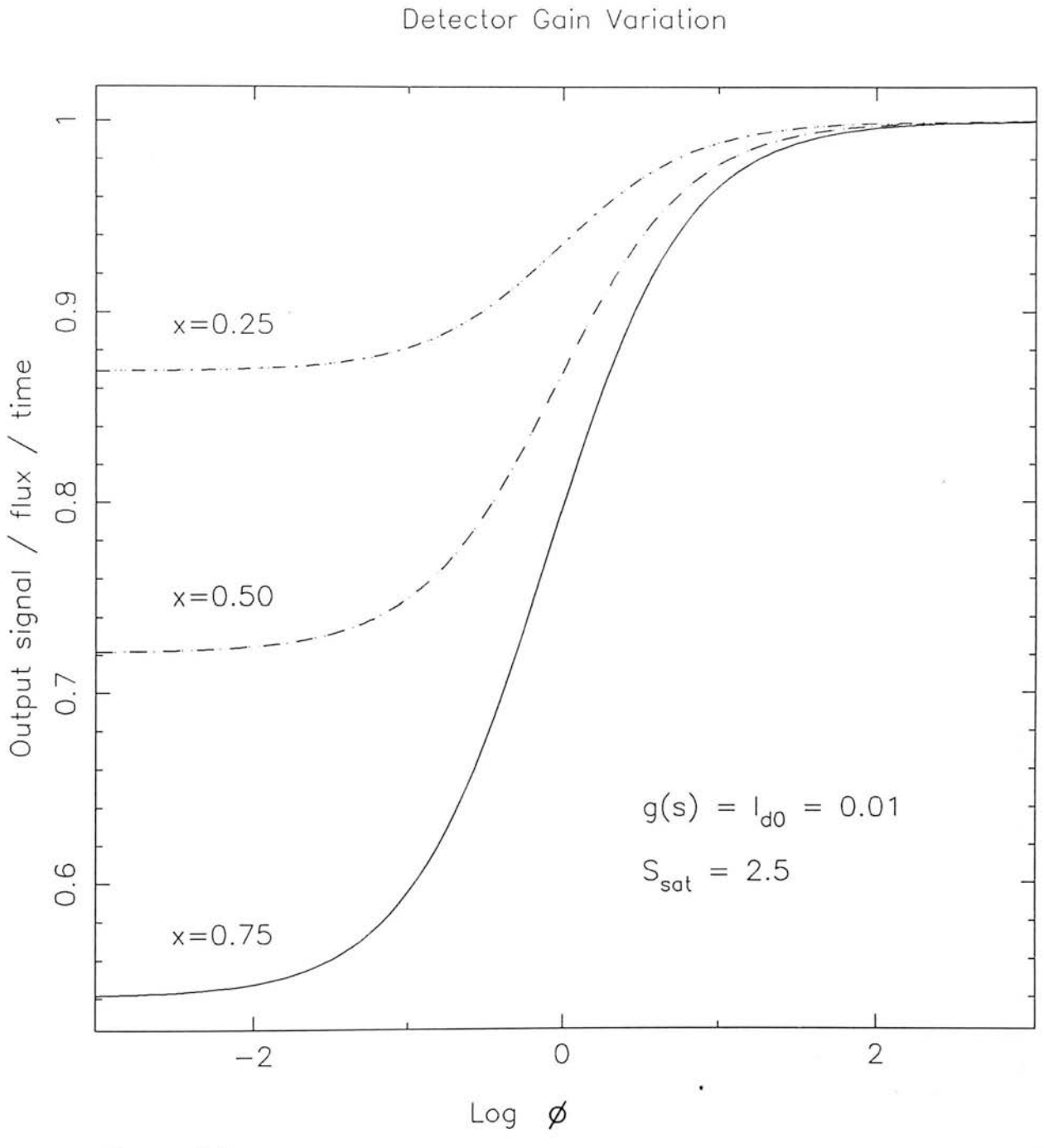
Detector Gain Variation
Output signal / flux / time
0.6
0.7
0.8
0.9
1
x=0.25
x=0.50
x=0.75
g(s) = I_d0 = 0.01
S_sat = 2.5
−2
0
2
Log ∅

Figure 6.6

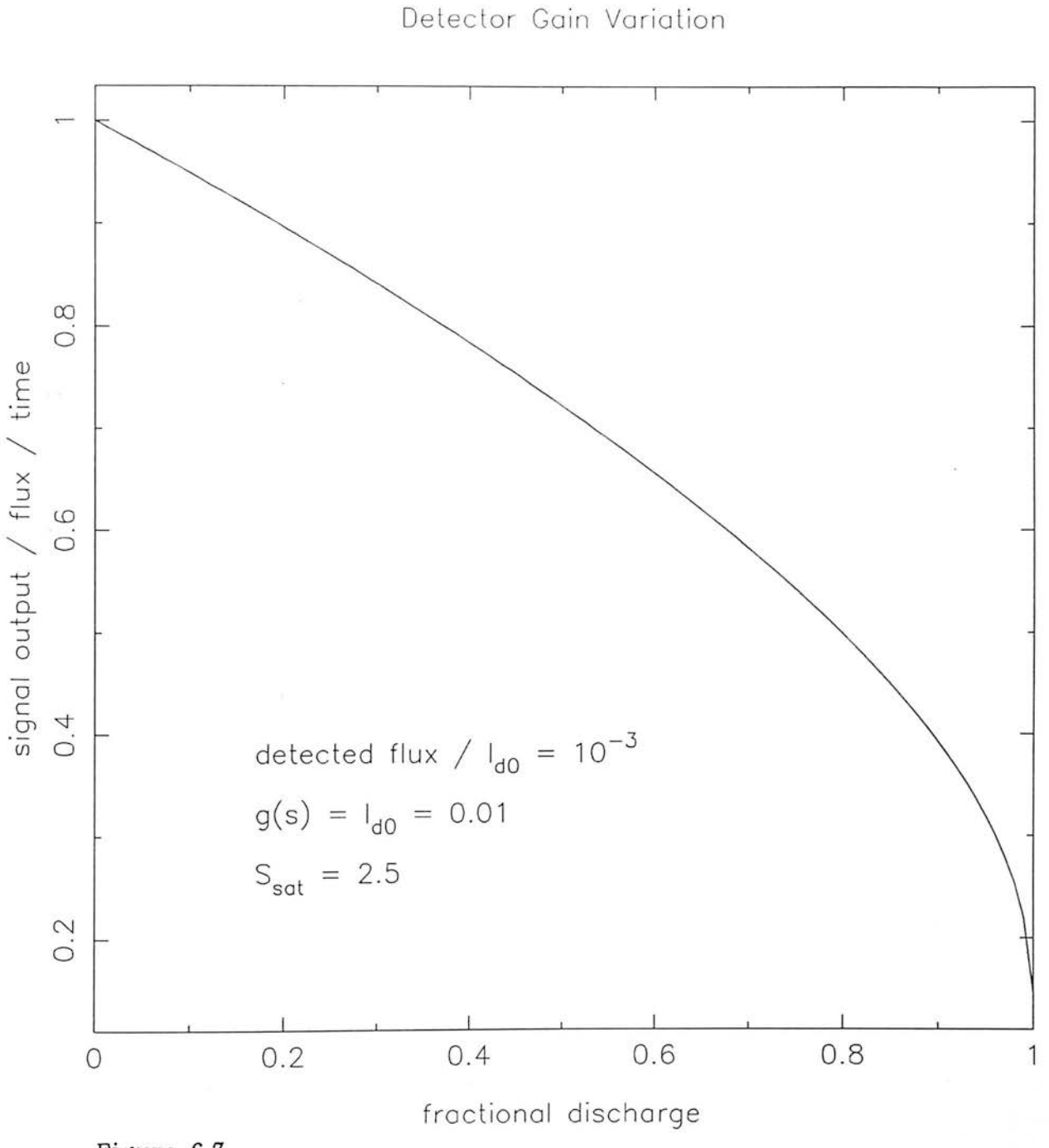
Detector Gain Variation
signal output / flux / time
fractional discharge
detected flux / I_{d0} = 10^{-3}
g(s) = I_{d0} = 0.01
S_{sat} = 2.5
0
0.2
0.4
0.6
0.8
1

Figure 6.7

Accurately removing the dark current in the region $\Phi<<1$ may not be possible given that; (a) The majority of the signal is due to dark current, with the photogenerated charge present as a small perturbation. (b) The dark current cannot be measured directly at the time of the observation so that small electrical and temperature drifts may have a significant effect on the calculated flux.

A further consequence of these results is that if the dynamic range across the array is large, there will be an extra pixel to pixel gain variation present (in addition to intrinsic pixel differences), which will remain after flat-fielding, if the calibration object's effective gain is less dependent on x (ie. if $\Phi>>1$) than that of the object being studied.

The explanation for the drop in g′ can easily be demonstrated by calculating the variation of the signal with flux at a constant integration time. The results for $\Phi\approx10^{-3}$ are shown in figure 6.8. The flux contribution is given by $S_\Phi(t) = g\Phi.t$ and the total signal is obtained from equation 6.7. The offset is simply the dark signal at t for $\Phi=0$ and is equal to $S_{sat}/2$.

The plot clearly shows that the drop in g′ is caused by a steadily decreasing amount of dark current, which reduces the signal slope and therefore the perceived flux. This behaviour will be present in integrating detectors where the I-V relation is more complex in form, since it is related to the fundamental fact that the dark discharge rate drops as saturation is approached.

The plot also demonstrates the linear relation between flux level and signal in this operating region.

6.4 Calibration of Integrating Detectors

A method of predicting the response of a detector, which takes into account both the dark current and the CTE non-linearity, has been proposed by A. Hoffman (1985 and 1987), and is discussed briefly in this

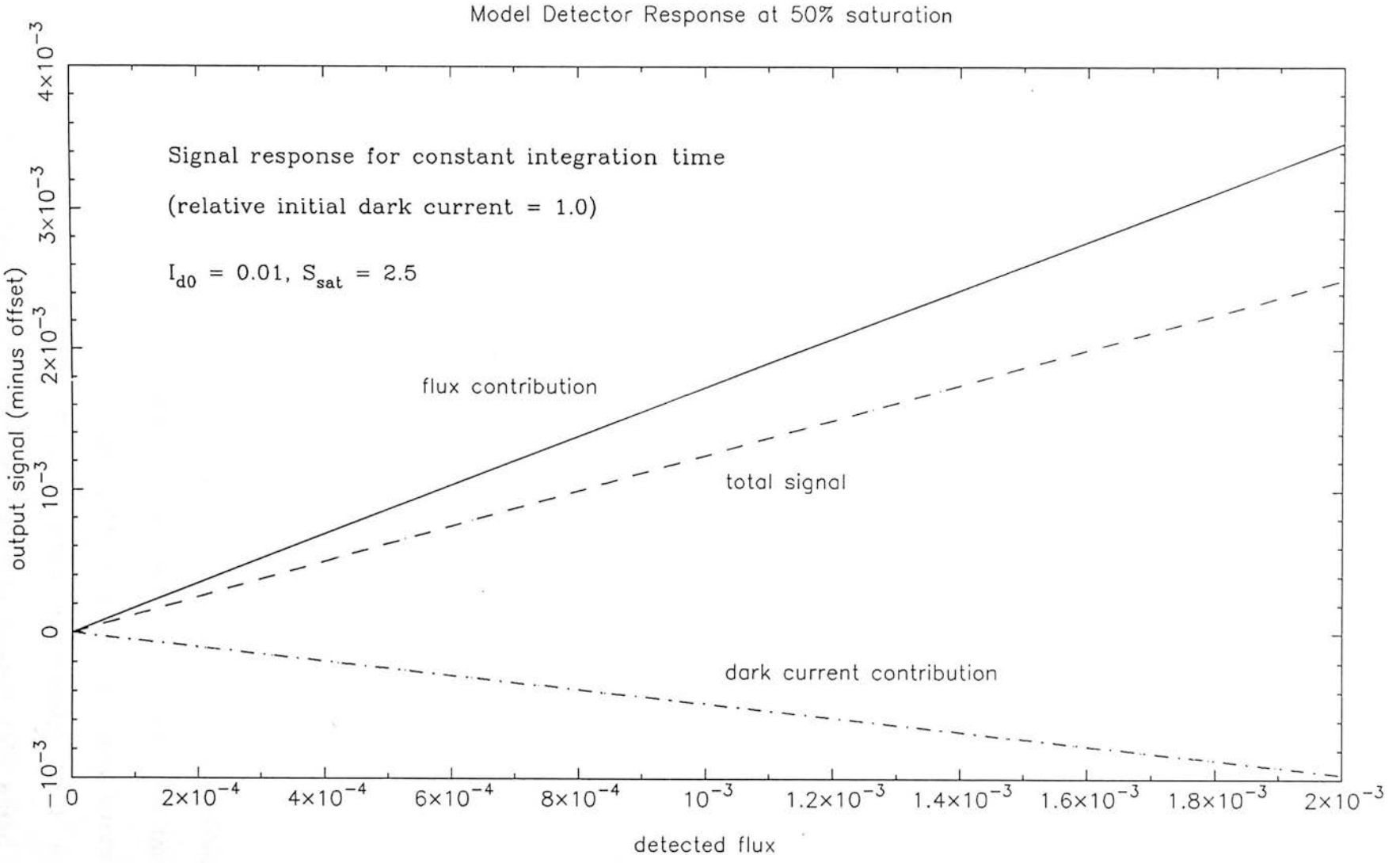
Model Detector Response at 50% saturation
Signal response for constant integration time
(relative initial dark current = 1.0)
I_{d0} = 0.01, S_{sat} = 2.5
flux contribution
total signal
dark current contribution
output signal (minus offset)
detected flux
4×10^{-3}
3×10^{-3}
2×10^{-3}
10^{-3}
0
-10^{-3}
0
2×10^{-4}
4×10^{-4}
6×10^{-4}
8×10^{-4}
10^{-3}
1.2×10^{-3}
1.4×10^{-3}
1.6×10^{-3}
1.8×10^{-3}
2×10^{-3}

Figure 6.8

section.

At a given point during the discharge, the discharge rate is the sum of a dark current component, which is a function of the voltage and the temperature, and a photocurrent contribution, which is a function of the voltage. Thus, at the detector;

$$\frac{dV_d}{dt} = -\frac{V_d}{R(V_d).C_d(V_d)} + \frac{I_\Phi}{C_d(V_d)}$$

At the output, this has the general form of equation 6.5. h(S) and g(S) can be found by measuring signal curves at two fluxes, F_1 and F_2 and using the relations;

$$h(S) = \frac{1}{F_2 - F_1}\left[F_2.\left.\frac{dS}{dt}\right|_{F_2} - F_1.\left.\frac{dS}{dt}\right|_{F_2} \right] \qquad (6.9a)$$

$$g(S) = \frac{1}{F_2 - F_1}\left[\left.\frac{dS}{dt}\right|_{F_2} - \left.\frac{dS}{dt}\right|_{F_2} \right] \qquad (6.9b)$$

The detector output, for a certain flux level and constant integration time, can then be found by numerical integration of equation 6.5. By repeating for different fluxes, a calibration curve can be constructed, where the flux is measured relative to F_2-F_1.

To avoid the difficulty of knowing the relative fluxes F_1 and F_2, it is easier to measure only the dark current for one frame (F_1=0), so that h(S) is simply $(dS/dt)_{dc}$, and use a suitable flat-field for the other (F_2). The calibration curve would give fluxes relative to the flat-field which would, at some point, need to be calibrated against a field of known brightness.

In order to test the model against illuminated data, h(S) was obtained from equation 6.9a using two of the flux curves (#1 and #2, see table 6.1), and g(S) was derived from a high illumination, zero dark current curve, in order to measure the CTE variation accurately. g(S) was normalised so that a flux input, Φ=1, would give an output rate equal to the initial dark current of 0.97 V/sec. The two functions are shown in

figure 6.9a. The model was then used to predict the output for another flux level (#4) in the following way;

(i) A calibration curve was created for t_i = 17mS.

(ii) For the voltage change from flux #4 in this time, the corresponding flux level was recorded.

(iii) For the same flux, the voltage change was measured from calibration curves at different t_i's, in order to reproduce the discharge curve.

The results are shown in figure 6.9b, and agree well with the original data, shown as crosses. The flux measured from the calibration curve agrees to within 0.5% with the value in table 6.1 of 2.63 V/sec.

Unfortunately, the model could not be tested over a wider range of fluxes due to constraints on the minimum detector illumination (dictated by the baffling arrangement), and, at the other extreme, the minimum readout time, which sets a limit on the maximum flux which can be recorded.

Using the forms for h(S) and g(S) derived from the experimental data, the effective gain variation for the InSb detector was calculated at x=75% (figure 6.10). This was achieved by measuring the gradient of the calibration curve at the point x for a number of curves, derived by numerical integration of equation 6.5, at different values of Φ/I_{d0}. The form is similar to that obtained with the 'simple' detector model of section 6.3, though the splitting is not as large, being 0.35 compared with 0.54, across a wide range of Φ/I_{d0}.

The disadvantages of using this method of calibration are;

(i) The calibration curve must be re-derived for different integration times and initial biases.

(ii) The procedure outlined for constructing this curve, in order to allow for pixel variations, must be repeated for each detector (2-D arrays may have more than 10^3 pixels), which requires a large amount of

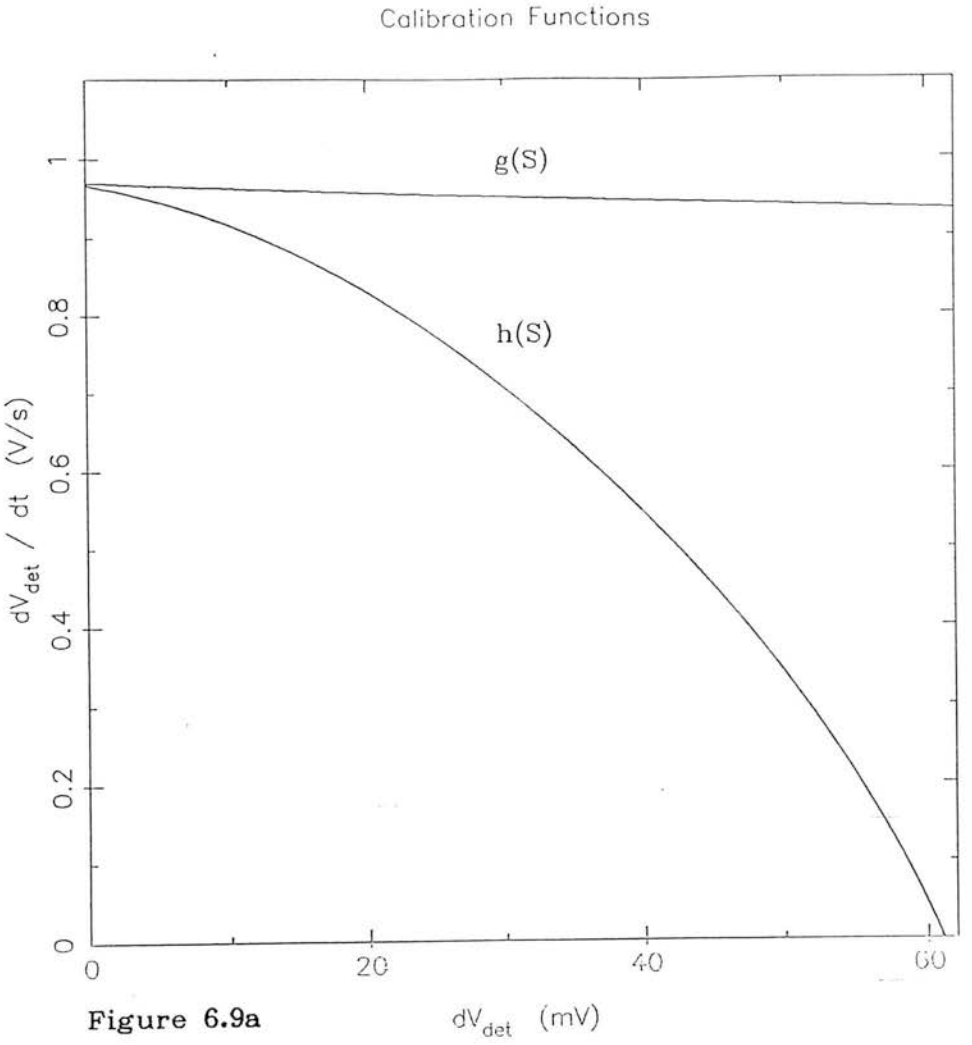

Figure 6.9a

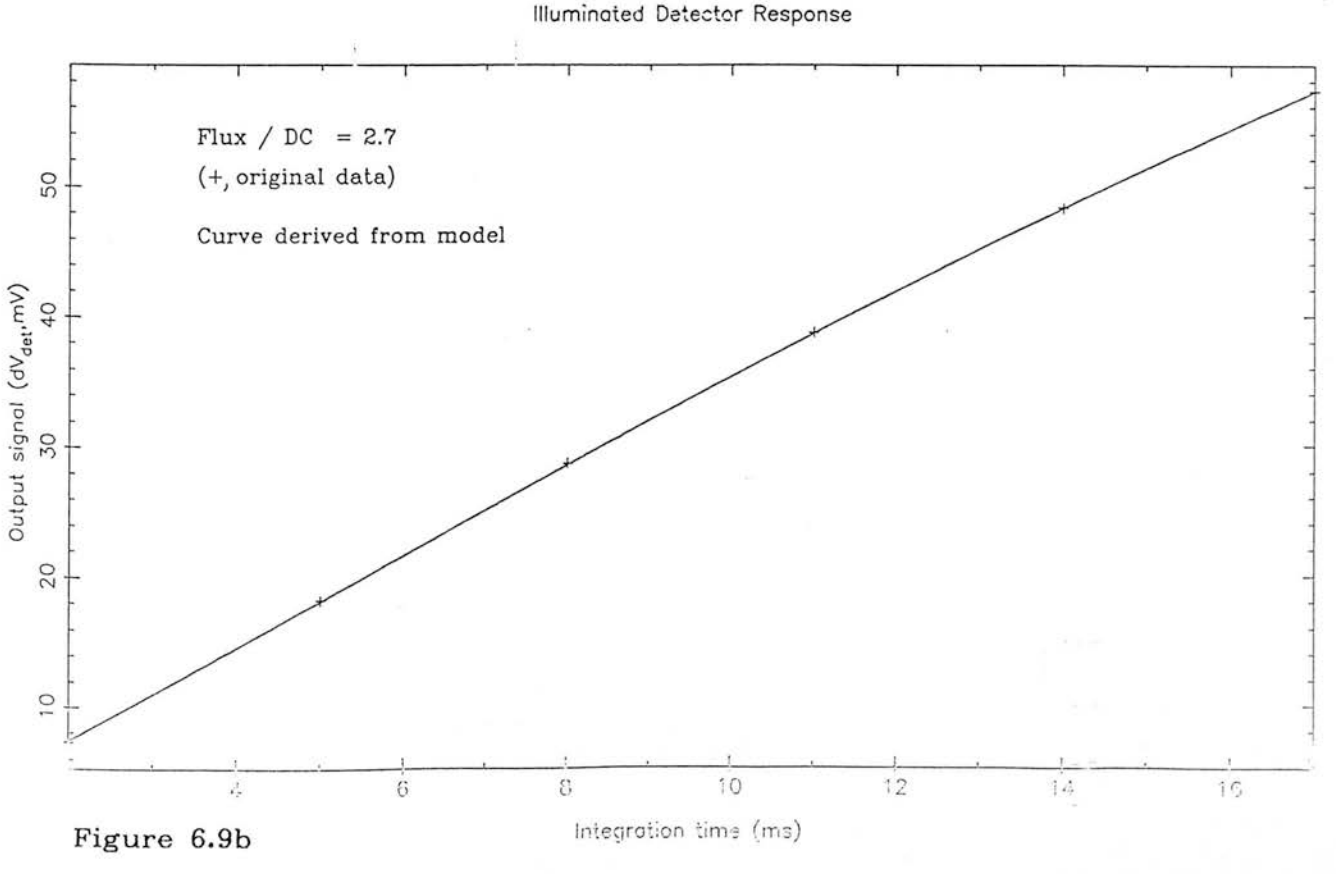

Figure 6.9b

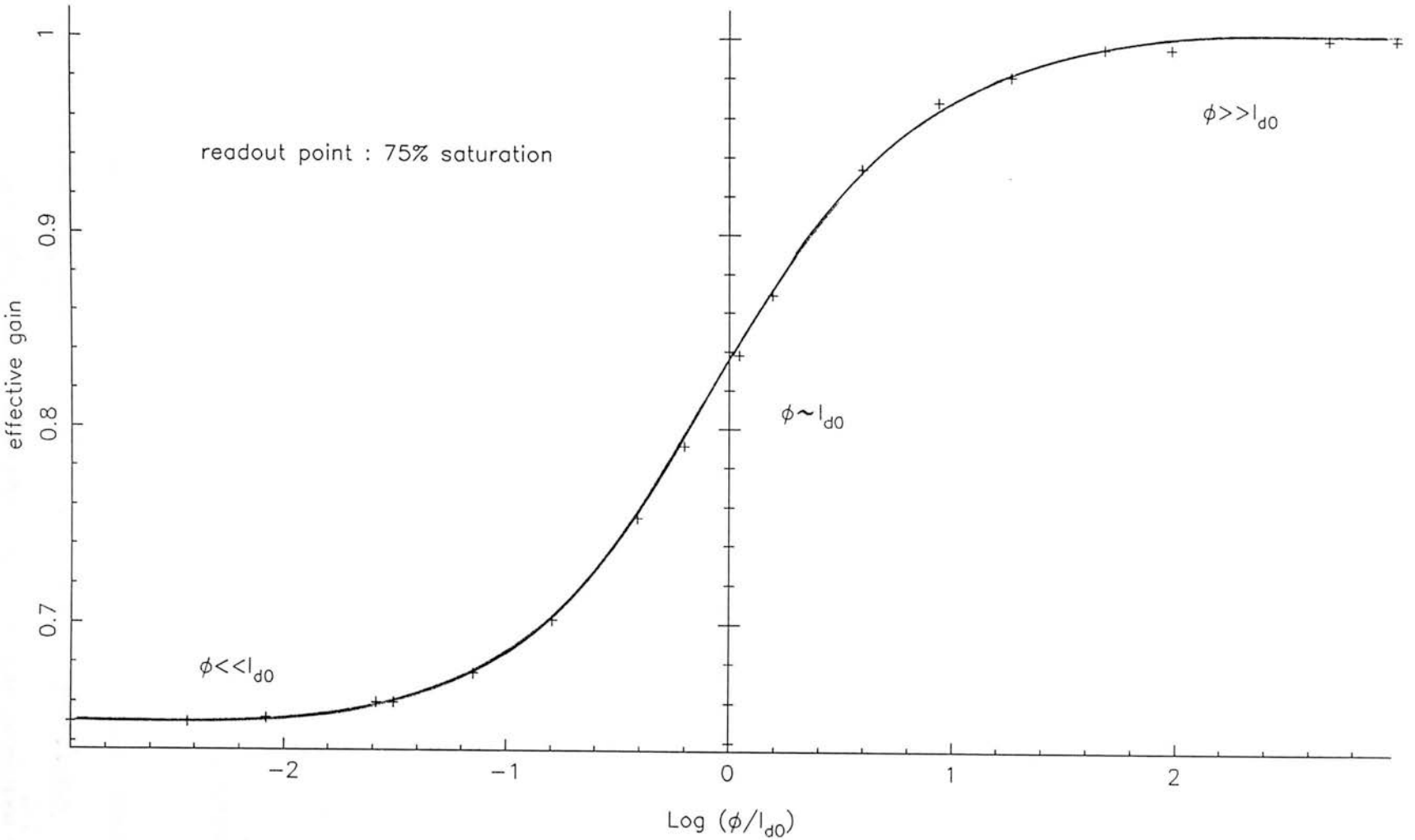

Figure 6.10 : Gain variation of InSb detector at 81K.

computer processing time. However, it may be possible to reduce the complexity by employing a small number of calibration curves, and somehow referring a given pixel, possibly by its position on an initial bias histogram, to the most applicable curve.

(iii) Though this model works well for the present data, further testing is necessary to confirm that it will be effective in the region $\Phi << I_{d0}$, where the flux signals are small (figure 6.8). This testing could best be performed in the low background environment of a spectrometer attached to a dedicated infrared telescope, where faint sources could be observed.

6.5 Conclusion

From the experimental results of the previous chapter, the following conclusions can be made concerning the performance of the CE linear array;

(a) From the point of view of capacitance, the pixel to pixel uniformity is good (the uniformity of radiation response was not investigated due to lack of time), suggesting that the pixel geometry and doping are also uniform.

(b) The detector responds linearly to illumination for both varying input levels at a constant integration time, and constant illumination with variable integration time. For reasonable values of reverse bias (less than 100mV) and discharge up to saturation, the signal response did not deviate by more than a few percent from the ideal. This response was better than initially expected from a consideration of the bias dependence of the detector capacitance, and is primarily due to the arrangement of the multiplexed readout circuit.

(c) The form of the dark current remains constant over the temperature range studied (54-80K) and implies potentially large integration times (>10 minutes) for moderate biases at temperatures which

can be achieved by cooling with solid nitrogen.

The dark current across the array was also found to be uniform (except for the hot pixel), and this is a direct consequence of (a).

(d) A way of sampling the signal was found that minimized the readout noise (analogue differencing of signal level and preceeding pedestal), though it was not possible to maintain the noise at the low level of a fast, low-discharge readout when the detector accumulated photo-generated charge. Excess noise was also observed when large values of bias (>100mV) were applied.

The minimum readout noise observed was 2300 electrons rms (at 80K, though this value was fairly independent of operating temperature), compared to an expected kTC noise limit at 80K of 2000 electrons rms.

In the light of results presented in this chapter, the following comments can be made about the calibration of integrating detectors;

(a) Objects which appear bright at the detector do not pose serious problems as far as photometric calibration is concerned.

(b) As the proportion of dark current relative to photocharge increases, so do the difficulties of accurately measuring the source brightness, though up to a certain point, correction techniques such as those described (sections 6.2 and 6.4) can be employed to recover the desired signal.

(c) If possible, since this will simplify data reduction, the array should be operated outwith the region $\Phi << I_{d0}$.

In a spectrometer, given that infrared flux levels from the telescope, sky and spectrometer itself can be simulated (see, for example, McCaughrean, 1987, which presents figures for the sky + telescope emission, as a function of wavelength, for UKIRT), the sort of conditions that will provide a low detector background, and therefore a small Φ/I_{d0} ratio, are; high wavelength resolution ($\lambda/\Delta\lambda > 10^3$), a cold spectrometer

optics temperature ($\lesssim$80K), wavelengths shorter than 2.5μm (where atmospheric OH emission dominates the telescope's thermal emission), and a small detector field of view projected onto the sky (which will be determined by the f-number of the spectrometer camera as well as the detector and telescope primary sizes, d and D, since FOV$\propto$(d/D).f-num^{-1}).

(d) It may be possible to increase Φ/I_{d0} in a number of ways;

(i) A constant low level of illumination could be applied artificially across the array.

(ii) The detector could be cooled to reduce I_{d0}. If the I-V relation changes, the change in the form of the effective gain may have to be considered, though the general trend will be to reduce the magnitude of the problem.

(iii) Instead of using InSb, which because of its large bandwidth (1-5.5μm), exhibits high dark current (the lowest values reported are of the order of 10^3 el/sec at 35K for 200μm square pixels), materials such as short-wavelength HgCdTe (dark currents of the order of 10^2 el/sec have been achieved at 77K for moderately sized elements) could be used.

(e) Calibration of data where $\Phi << I_{d0}$ could be performed using similarly faint standards, so that nearly equivalent effective gains are sampled in the two instances, and these will cancel out during ratioing. The overall sensitivity, however, will be degraded by the poor S/N ratio of the standard.

(f) In section 6.3, from an analysis of the response of a simple detector, it was stated that a spectrum output from an array with a large dynamic signal range, would exhibit an extra pixel to pixel non-uniformity in addition to the standard variations of qe, responsive area, vignetting etc. This arises from a modification to the perceived gain caused by the dark charge contribution to the signal, the variation from normal 'photon' gain being greatest for low values of Φ/I_{d0}.

A large variation in the effective gain across the array is obviously

undesirable because it will alter the intrinsic shape of the spectrum, and, as noted above, may be difficult to correct. This situation would most likely occur in the case of an array exhibiting non-uniform dark current (see results of observations made with an integrating array installed in a spectrometer, section 7.4).

In other words, dark current uniformity, as well as low levels of dark current, are important criteria in integrating arrays for effective flat-fielding of faint objects.

CHAPTER SEVEN

ASTRONOMICAL SPECTROSCOPY IN THE NEAR-INFRARED

Introduction

The 'atmospheric windows' in the electromagnetic spectrum between the wavelengths of one and five microns (the near-infrared) contain a large number of spectroscopic features of use in the study of a wide range of astronomical objects. These features include vibrational - rotational transitions of gaseous molecules such as H_2 and CO, recombination emission lines from the abundant elements hydrogen and helium, fine structure lines from ions, and broader solid-state features due to substances such as H_2O (ice), solid CO and silicates. The diagnostic uses are many, ranging from temperature and density measurements (from line ratios of different transitions) to luminosities (line intensities) and velocity structure (line profiles). Some areas of infrared astronomy where spectroscopy has been applied are described briefly below;

The process of star formation occurs in a complex environment within dense molecular clouds, where optical extinction prohibits detailed study, whilst infrared extinction is negligible in comparison. The cold gaseous constituents of the clouds can be studied through the presence of CO absorption towards obscured infrared sources, which provide the back-illumination. This technique can also disclose the nature of dust grains, which can accrete many different molecules.

Associated with some obscured sources, which are believed to be newly formed, or forming, stars, are the phenomena of high velocity, sometimes bipolar, outflows of gas. These winds can result in shock excitation, and subsequent emission from H_2 in the cooling gas, which has many vibrational - rotational (v-r) transitions in the infrared. CO

emission near 5μm has also been detected in shocked gas.

Other objects in which molecular hydrogen emission has been detected include planetary nebulae, supernova remnants, the Galactic Centre, and interacting and active galaxies. Molecular hydrogen can also be excited radiatively by UV photons, leading to different line ratios from the collisionally excited case.

HII regions are found close to or within molecular cloud complexes, and contain gas photoionized by recently formed OB stellar associations. The UV excitation within these regions can be inferred by observing the bright hydrogen recombination lines emitted.

The spatial mapping of recombination and fine structure lines can provide details on the state of excitation of the gas and the location of the ionizing sources. An even more powerful tool is the ability to study the gas motions by analysing Doppler shifts and broadening of the emission (and absorption) lines. In cases where the line of sight intersects severals clouds of gas, the line profiles may contain detailed velocity structure. High resolution is then necessary to resolve the various components. The Galactic Centre is a good example of a region where these methods of mapping have been applied successfully.

Apart from the above example, there are a number of other instances where high wavelength resolution is desirable; firstly as a means of separating closely spaced lines, such as the H_2 Q-branch or the line pair, HeI (1.083μm) and Pγ (1.094μm). Secondly, for a bright continuum, increasing the resolution until the line is just resolved, will improve the contrast, and thus the detection sensitivity.

In many situations it is necessary to know the amount of reddening of the observed radiation, in order to determine the intrinsic source properties, such as luminosity. One way of obtaining the extinction to the emitting gas is to measure line ratios of a single species, and ideally involving common upper levels (ie. Pβ and Brα), so that the result is

independent of temperature.

Finally, infrared lines are observed in a number of stellar environments, for example; Wolf-Rayet stars, which exhibit strong stellar winds; Stars with circumstellar dust shells; Planetary nebulae, where a shell of gas is ejected, and photoionized by the hot core to create a bright emission line nebula. An example of the abundance of spectral features in the near-infrared is illustrated by a 1.0-2.3μm spectrum of the unusual star η-Carinae (Allen, 1985), in which more than thirty-five lines were detected.

The observations presented in the first three sections of this chapter, of the Galactic Centre, the Orion molecular cloud, and a sample of Seyfert galaxies, were all obtained using a cooled, grating spectrometer (CGS 2) on UKIRT. For this reason a brief description of the instrument is given here (see Wade, 1983, for a detailed description).

The spectrometer receives a collimated beam from the telescope (17mm diameter, providing the option of inserting a Fabry-Perot etalon), which is first focussed at the entrance aperture, passed through a blocking filter, then re-collimated onto a grating operated in the Littrow configuration. A number of gratings are available to provide high efficiency from 1-5μm and a resolution, R ($=\lambda/\Delta\lambda$) in the range 200-800. The wavelength is scanned by rotating the grating with a stepping motor.

The dispersed radiation is focussed onto a linear array of seven InSb PV detectors, which define the exit apertures, giving a maximum sky FOV of 5.4". Each detector is connected to its own in-situ preamplifier, with the outputs connected to external programmeable amplifiers, voltage-to-frequency converters and up/down counters, where the phase-sensitive detection is performed. The counters are in phase with the chopping telescope secondary mirror, which is normally oscillated at 10Hz.

A twin vessel cryostat houses the spectrometer, so that the detector

can be cooled by solid nitrogen (≈50K), and the optics and preamplifier circuits by LN_2.

The final section of this chapter presents some data obtained with a similar spectrometer, which has been fitted with an integrating array. Part of the aim was to judge the array performance in this special environment.

7.1 The Central Ten Parsecs of The Galactic Centre Region

The Galactic Centre has mainly been studied in the infrared and radio parts of the spectrum, as these wavelengths can penetrate the interstellar matter lying in the Galactic plane along the line of sight, a distance of approximately 10kpc. The visual extinction is of the order of thirty magnitudes.

The central region shows detailed structure over a range of scale sizes (see Genzel, 1987, for a recent review of this topic). At moderate distances from the centre of between two and ten parsecs (where 1pc corresponds to an angle of 21" on the sky), there is a neutral disk of warm (300K) gas orbiting in the general sense of galactic rotation.

Far-infrared mapping (Becklin, 1982) showed that there was a ring of dust surrounding the centre and lying in the galactic plane, with an inner radius of 1.7pc, within which the density was found to be significantly lower, and that the sources heating the dust were centrally concentrated.

Within this ring is the HII region, Sgr A West. The ionized gas distribution has been mapped at high spatial resolution using the Very Large Array at 6cm (Genzel, 1987, figure 2). At this wavelength free-free continuum emission predominates. Several spiral-like filaments are seen, one of which, the 'Western arc', closely follows the inner edge of the dust ring. From velocity studies of the [NeII] 12.8μm line (Serabyn, 1985), the arc is interpreted as gas in a Keplerian orbit about the Galactic

centre with an orbital velocity of 110 kms^{-1}. A similar analysis of another filament, the 'Northern arm', showed that it passes closer to the centre, and may represent a stream of gas approaching it. Gravitational considerations of the observed gas motions imply a mass $\gtrsim 3.5 \times 10^6 M_\odot$ within a radius of 0.5pc.

To account for all the ionizing luminosity observed within the central 3pc requires a source with an effective temperature of 35,000K (this relatively low value for an HII region was determined from the observed ionization state of the gas) and a bolometric luminosity of $10^7 L_\odot$.

At the centre of the 6cm map, linking the filaments, is a bright bar which is coincident with the Galactic Centre, as defined by the peak of the 2μm intensity distribution (which traces the stellar density peak through the K and M giants, which dominate the emission at this wavelength). Also in the bar is the unusual compact radio source, Sgr A*, whose nature is similar to radio sources seen in the nuclei of galaxies, ie. a non-thermal spectrum and rapid time variability (Brown, 1984).

The area in and around the bar, representing the central few parsecs has been continuum mapped at 2.2 and 10μm (Becklin, 1975). A number of compact infrared sources are seen, many of which show 2.3μm CO absorption, suggestive of clusters of late-type stars. IRS16, which has been resolved into a number of components, lies closest to the centre and Sgr A*. This object is unusual in several respects. Firstly, the CO feature is weak. Secondly, the HeI 2.06μm and Brα 4.05μm lines are unusually broad in this direction (FWZI$\approx$1400kms^{-1}). This high velocity gas, which is localized, with a FWHM extent of only three arcseconds (0.14pc), may best be explained dynamically by the presence of a wind (Geballe, 1987). This is supported by the detection of shock excited H_2 along the inner edge of the dust ring (Gatley, 1986).

The source of energy for this wind, as well as the nature of the central mass, remains to be identified.

The present observations (which were obtained by Dr Wade and Dr Geballe in July 1984), were concerned with investigating the extinction uniformity towards a number of sources (IRS1,2,4,5,6,9,16, see maps in Becklin, 1975). This information will enable comparison of the properties of these and other Galactic Centre sources. The method was to measure the ratio of Brα to Brγ (2.17μm) emission and assume an intrinsic ratio from case B recombination theory ($n_e=10^4 cm^{-3}, T_e=7500K$) of 2.9.

By also observing the He 2.06μm line, the location of the ionizing sources can be inferred from the He/Brγ ratio, since the ionization potentials for hydrogen and helium are different. These lines are well suited, as there is minimal differential extinction between them.

The spectra were reduced in the standard way, by ratioing the raw object spectrum with an F or G stellar spectrum, and multiplying by a black body of the effective temperature of this star. This process corrects for wavelength variations in atmospheric transmission, transmission through the telescope and spectrometer optics, and detector qe, since the object is divided by a spectrum deemed to be 'flat' above the atmosphere.

The resultant spectra were flux calibrated by comparison with standard stars of known magnitude, and, finally, a small correction was made to the Brackett line intensities because of corresponding faint absorption in the ratio stars.

Some of the reduced spectra are shown in figure 7.1. The total integration time per point was of the order of 1 minute, through a 5'' aperture, and the resolution at 2 and 4μm was measured as 470 and 560 respectively.

IRS16 has the brightest He emission, but the ratio He/Brγ shows little tendency to fall off with distance from this object.

The reddening between 2.17 and 4.05μm was found to be spatially uniform, within the uncertainties, at 1.9+/-0.2 magnitudes, corresponding

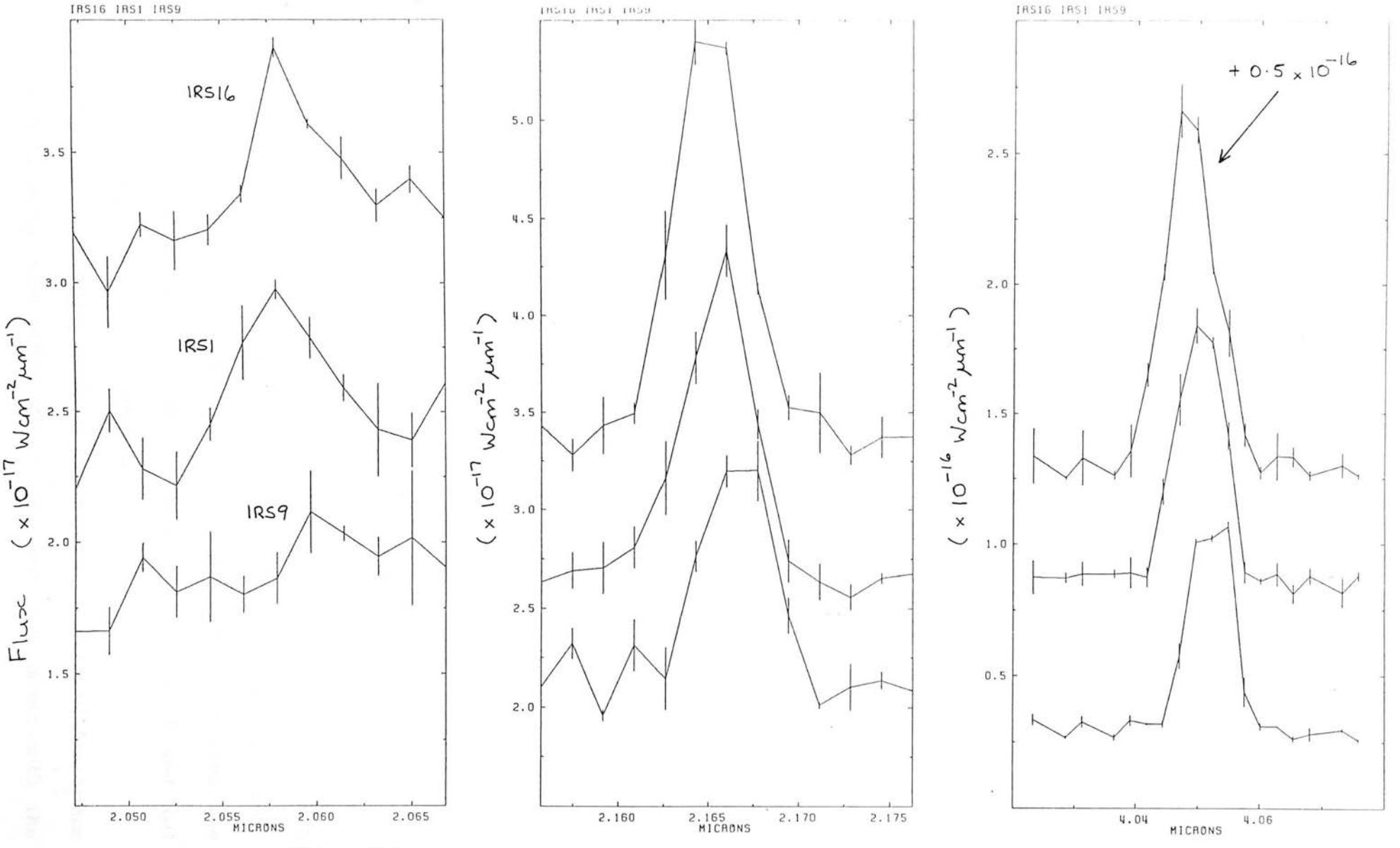

Figure 7.1
He 2.06μm, Brγ and Brα line spectra for three Galactic Centre sources.

to a visual extinction of 27 magnitudes (assuming the reddening curve of Rieke, 1985). The reddening of the ionized gas is similar to that measured to the stars there, and its uniformity implies an interstellar origin. Wade, 1987, contains a full discussion of the results.

7.2 H_2 Spectroscopy of the Orion Molecular Cloud, OMC-1

The proximity of the Orion nebula (500pc) has made it the most intensively studied region of active star formation. It is also the brightest source of H_2 emission in the sky.

A very brief outline of Orion's morphology is as follows; The optical nebula, an HII region photoionized by an OB association, the Trapezium cluster, lies immediately in front of a giant molecular cloud. Within this cloud is a dense molecular core containing a cluster of infrared sources (the Becklin-Neugebauer source (BN) and the Kleinmann-Low nebula), which, as projected on the sky, lie about an arcminute N-W of the Trapezium cluster. Several of the sources (eg. BN and IRc2) have been shown to be self-luminous. Evidence for large optical depths is provided by the presence of deep ice (3.1μm) and silicate absorption features toward BN, which are not seen in the interstellar medium (ISM). Brα and Brγ emission has been detected from BN indicating the presence of a compact HII region, photoionized by a young star whose luminosity is $1\text{-}2\text{x}10^4 L_\odot$.

IRc2 is of interest since it is thought to be surrounded by a dust disk, seen edge on, which collimates gas and radiation outflow from the source through the poles. Evidence for this comes from 3.8μm polarization maps, which indicate large amounts of scattered radiation from the direction of IRc2, and from the trajectories of low velocity OH and H_2O masers, which trace the molecular outflow.

Finally, the whole region emits large amounts of infrared continuum radiation from warm dust within OMC-2, and hot dust mixed with the

ionized gas.

At ambient molecular cloud temperatures, H_2 is in the ground-state. A situation in which the temperature can be raised, so that the v-r levels become populated, can occur when highly supersonic gas collides with dense, cool gas so that a shock front develops. Heat is dissipated behind the front, primarily via emission from a cascade of the H_2 v-r levels.

Shock fronts are observed in bipolar outflow sources, which in turn are associated with early stages of stellar evolution. Studies of the H_2 emission can provide information about the shock waves, such as the kinetic energies involved, outflow motions, and temperature structure of the shocked region.

In OMC-1, the H_2 emission extends over a few tenths of a parsec, centred on the infrared cluster, with a bright peak (Peak 1) 15"N and 7.5"W of BN. The observed lines are broad, with FWZI$\approx$100kms^{-1}, and their velocity structure suggests radial outflow.

A 3-4μm spectrum of Peak 1 in a 5" aperture shows a profusion of H_2 transitions (figure 7.2), with levels populated up to E/k=26,000K, as well as the 3.3μm emission feature and the broad dip of ice absorption around 3.1μm. This data was obtained and flux calibrated by Dr Tom Geballe.

If the cooling gas is in LTE then the H_2 energy levels will be populated according to the Boltzmann distribution. For the densities encountered, the line emission is optically thin, so that the observed intensities are proportional to;

$$I_{v,j} \propto hc/\lambda \; . \; A_{v,j} \; . \; N(v,j) \; . \; 10^{-A_\lambda/2.5}$$

A_λ is the extinction at the observed wavelength, N(v,j) the column density of molecules in a given upper state with vibrational and rotational quantum numbers, v and j respectively, and $A_{v,j}$ is the spontaneous decay rate (s^{-1}). N(v,j) is given by;

$$N(v,j) = N \; . \; g(j)/Z(T) \; . \; \exp(-E_{vj}/kT)$$

$$g(j) = 3\,(2j+1) \quad j \text{ odd} \quad \text{(ortho-state)}$$

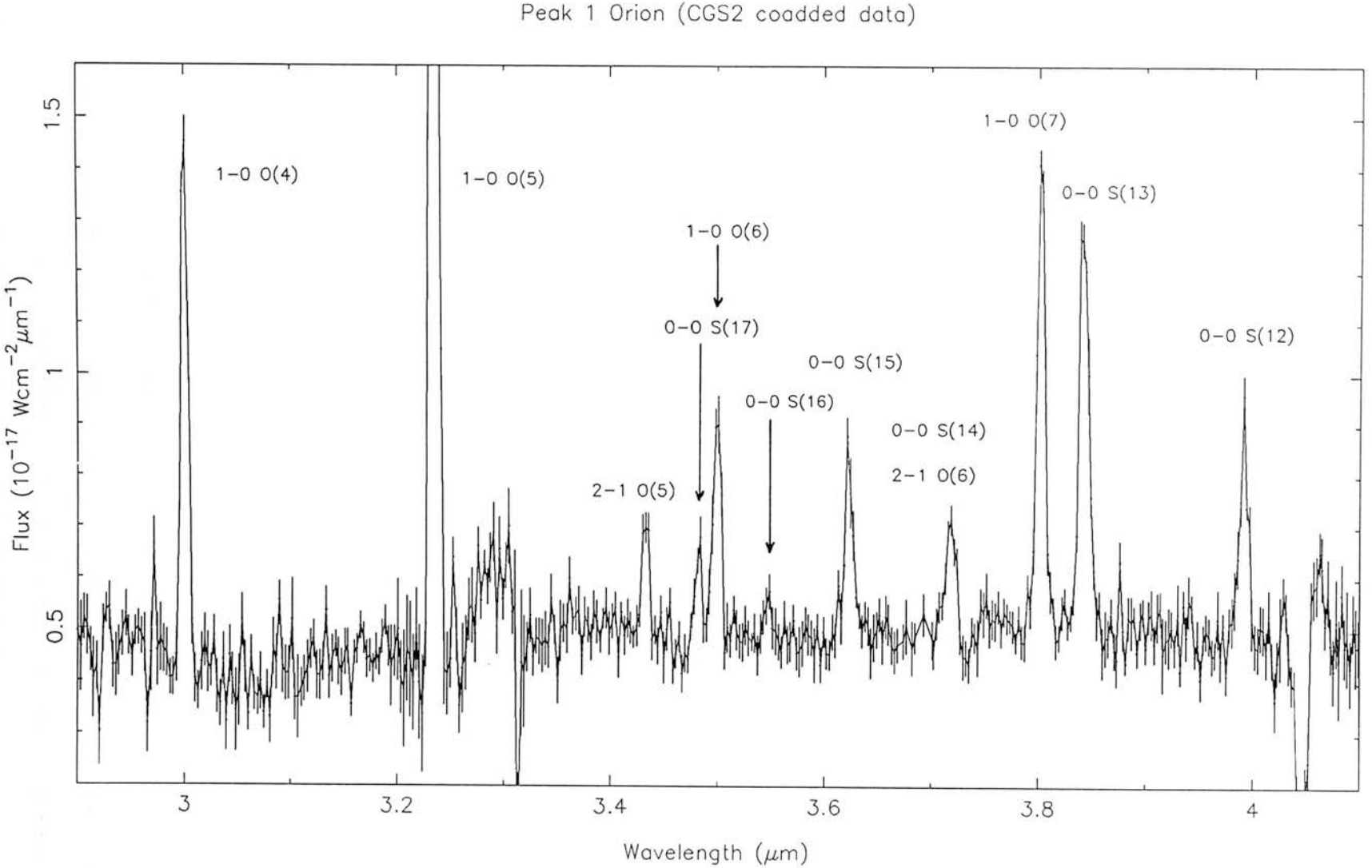

Figure 7.2
Spectrum of Peak 1 in Orion, showing prominent H_2 emission lines.

$= 2j + 1$ j even (para-state)

where N is the total column density, g(j) the upper level degeneracy and E_{vj} its energy. The partition function, Z(T), for a given molecule and ionization state, is only a function of temperature, T.

A plot of log[N(vj)/g(j)], obtained from the observed fluxes, versus the upper level temperature is shown in figure 7.3 for the lines detected. The error bars represent +/-1σ uncertainties in the fluxes. The dereddened points are also shown and were derived assuming a $1/\lambda$ extinction law (no correction was made for enhanced extinction at 3μm), and an absolute extinction to Peak 1 of $A_{2.122\mu m}$=2mag.. This value is taken from Beckwith, 1983, and although the error could be as large as +/-50%, the differential extinction across the spectrum is only 0.35mag., so that uncertainties in $A_{2.122\mu m}$ will not have a dramatic effect on the appearance of the plot.

The H_2 temperature can be derived from the slope. Treating the left hand (5 points) and right hand (7 points) straight-line regions independently, yields 1900+/-400K and 2900+/-600K for the low and high excitation states respectively. This could be interpreted physically as a temperature gradient in the cooling material.

Brand, 1988, incorporates these line measurements, using a different foreground extinction, in order to support a cooling flow model for the shocked gas. A problem at present, however, is that the model for the shocked region predicts that the H_2 will become dissociated at shock velocities greater than 25kms^{-1}. From the observed broad emission lines, this figure does seem to be exceeded.

7.3 Line Emission from Seyfert Galaxies

Seyfert galaxies are a class of active galaxies which appear optically as a bright, blue, unresolved nucleus. The nucleus is invariably associated with an underlying, extended spiral structure.

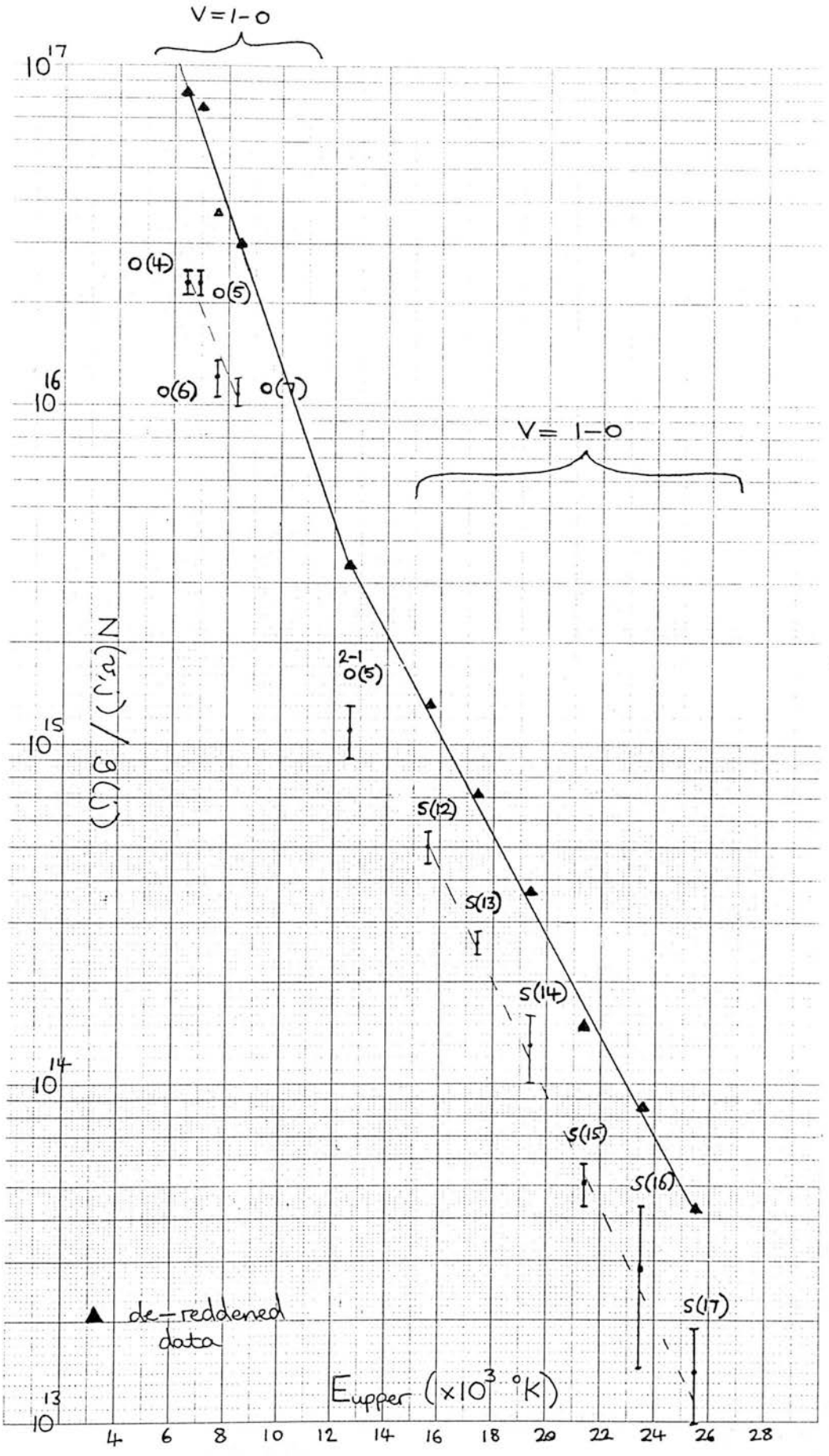
V=1-0
V= 1-0
O(4)
O(5)
O(6)
O(7)
2-1
O(5)
S(12)
S(13)
S(14)
S(15)
S(16)
S(17)
de-reddened data
N(v,J) / g(J)
E upper (×10^3 °K)
10^17
10^16
10^15
10^14
10^13
4
6
8
10
12
14
16
18
20
22
24
26
28

Figure 7.3

Spectroscopically these objects are characterized by strong emission lines and, in the case of type I Seyferts, by the presence of two components; (i) A compact broad line region (BLR), where permitted lines are observed with widths $\gtrsim 10^4 kms^{-1}$, containing fast moving, high density gas clouds. (ii) A more extended narrow line region (NLR), where forbidden lines with widths $\lesssim 10^3 kms^{-1}$ are observed, indicative of lower densities. Gas motion in the NLR is predominantly radial. From optical spectroscopy of forbidden transitions of atoms in various ionization states, there seems to be a smooth transition from NLR to BLR, whilst the variation of line width with ionization potential supports the view of a centrally concentrated ionizing source.

Type II Seyferts have permitted and forbidden lines with comparable widths (similar to those seen in the type I NLR), suggesting a common place of origin. From recent evidence, the BLR may be hidden by dust in the form of a disk seen edge-on.

A correlation between permitted line strengths and continuum level, suggests that the gas is photoionized, a proportion of this continuum being non-thermal radiation, which, in the case of type I dominates the stellar contribution. Seyfert galaxies are strong infrared emitters, and in type II, this seems to be primarily thermal radiation from dust. A number of Seyferts mapped at radio wavelengths have bright lobes extending over a large part of the galaxy, possibly the result of high velocity, collimated outflow of gas from the nucleus.

The energy source within Seyfert nuclei, giving rise to the high velocities, and intense luminosity (in some instances the bolometric luminosity within the central parsec is of the order of $10^{12} L_{\odot}$, see Weedman, 1977), remains to be identified, but seems to have a lot in common with our own Galactic centre, the latter possibly displaying a quiescent phase of the former.

Observations of a small sample (five) of Seyferts were made in

January, 1986 at UKIRT, where the aim was, principally, to measure the intensities of the recombination lines HeI 2^3P-2^3S (1.083μm) and Pβ (1.282μm).

The He line when compared with the 3^3D-2^3P (587.6nm) transition, can provide information on the optical depth (and hence density) to the emitting gas. This is because, in a high density medium, optically thick in the 1.083μm line (caused by a large population of the metastable 2^3S state), the 587.6nm line will be collisionally enhanced. As the optical depth increases, the ratio λ10830/λ5876 will decrease, whereas the opposite trend would be expected from increasing dust extinction (Davidson, 1979).

Using Pβ it should be possible to de-redden the line fluxes, and also correct the He intensity for contamination from Pγ.

The fully-sampled spectra of NGC1068 (possibly type II, z=0.0036, total integration time per point of 24s) and MCG 8-11-11 (type I, z=0.02, integration time per point of 2 minutes), calibrated in observed wavelength, are shown in figure 7.4. The error bars represent the rms deviations of a number ($\gtrsim$10) of coadded spectra. R was approximately 250.

In this study the Seyfert redshifts are advantageous in that they move the He line away from the edge of the filter cut-off, where, as can be seen, the noise is large. The presence of Pγ appears in both spectra as an asymmetric broadening of the He line. The spectrum of NGC1068 also contains a merge of HeI (1.253μm) and [FeII] (1.257μm).

An idea of the sensitivity of the instrument can be judged by the faint Pβ line of MCG 8-11-11, with a flux of $(1.3+/-0.3)\times10^{-20}$Wcm^{-2}.

7.4 CGAS Observations of White Dwarf Stars

In September, 1987, an opportunity arose to take part in an observing run involving the use of a cooled, grating array spectrometer (called CGAS) on the 3m NASA Infrared Telescope Facility (IRTF). The proposed aim was to search for pressure broadened H_2 absorption in the

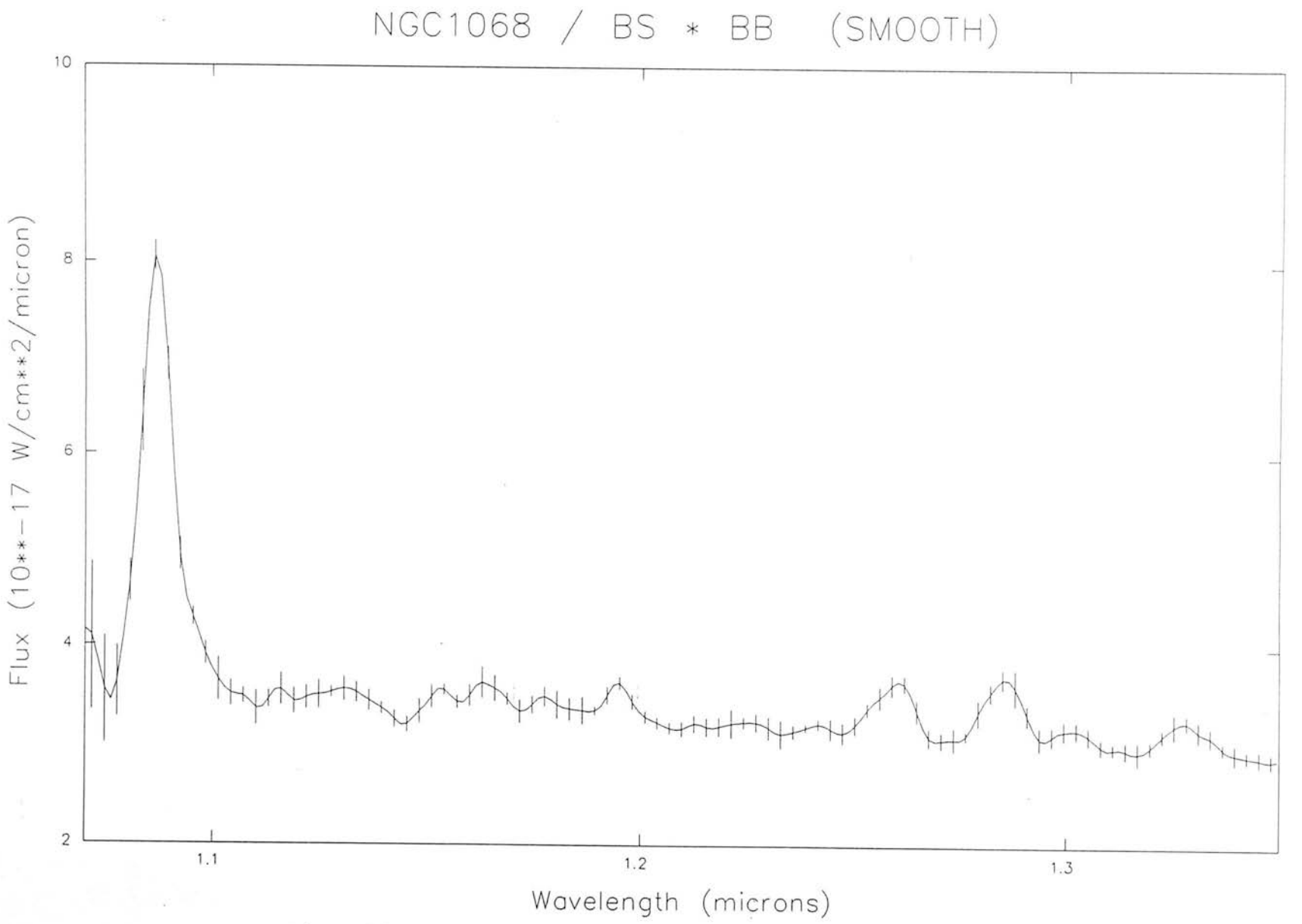

Figure 7.4
Infrared spectra of the Seyferts NGC1068 (above) and MCG 8-11-11 (over).

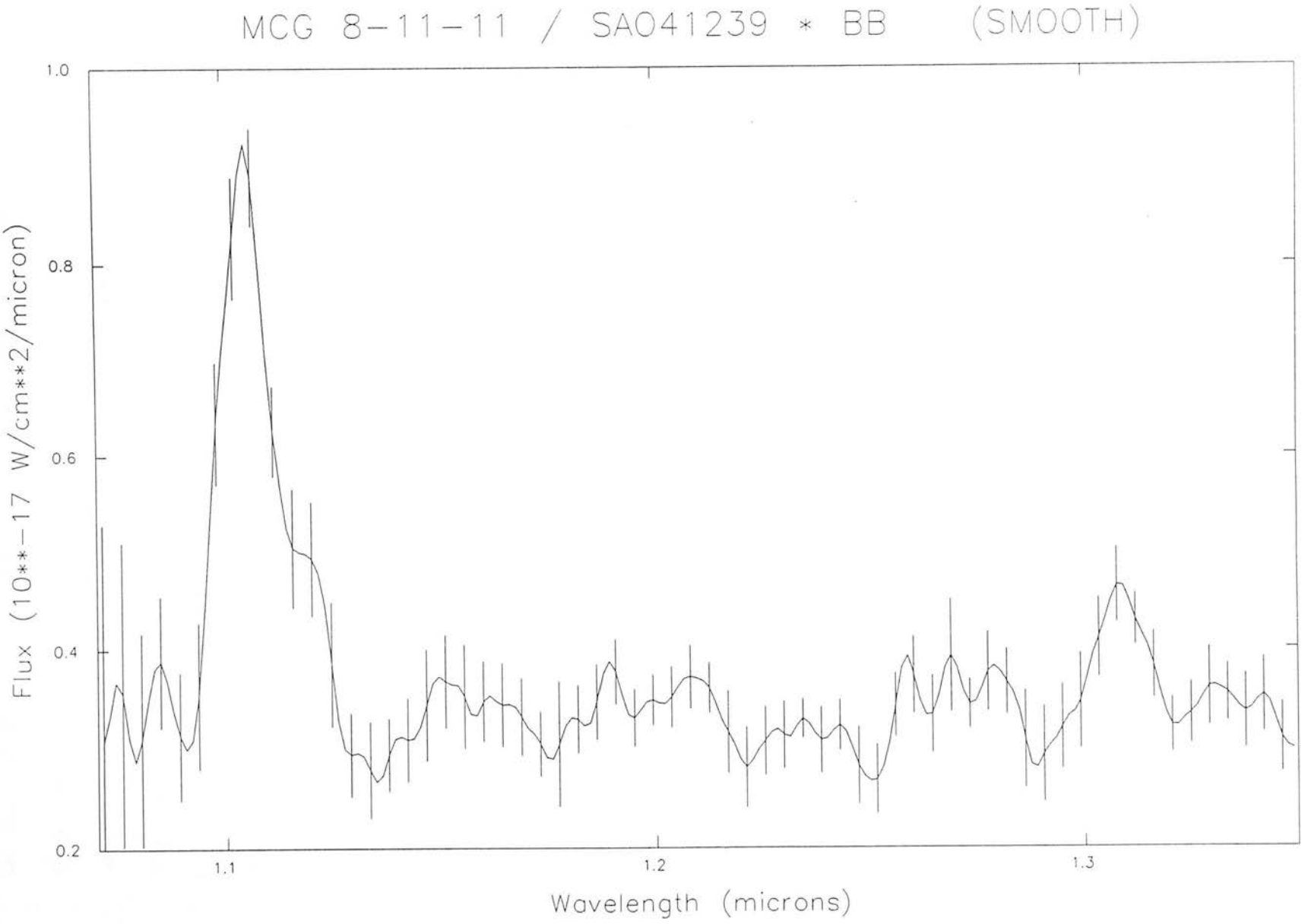
MCG 8-11-11 / SA041239 * BB (SMOOTH)
Flux (10**-17 W/cm**2/micron)
1.0
0.8
0.6
0.4
0.2
1.1
1.2
1.3
Wavelength (microns)

atmosphere of white dwarf stars. H and K-band spectra were to be obtained in order to accurately define the continuum. CGAS was chosen because of its high sensitivity and moderate resolving power, which enables the whole K window to be recorded in one go, without the need to move the grating. Consequently the spectrum is under-sampled but this is offset by the advantage of wavelength stability.

The 1-5μm spectrometer provides a range of resolutions (R=100-1800), depending on the grating installed. Detection is performed with an identical array to the one investigated in the bulk of this work, the CE 32 element InSb linear array, with similar signal processing electronics, apart from the use of a 16-bit A/D instead of 12. The FOV of each detector was fixed at 2.7", which can lead to 'light-loss' problems, unless the seeing is excellent.

The normal method of taking data involves an object integration (of up to 15 minutes), followed by an equal exposure on the sky, with sky sampled on opposite sides of the object to correct for background gradients. All the readouts can be recorded, and this allows monitoring of the electronic and sky stability.

This observing run provided an ideal oportunity to investigate the performance of an integrating array in a low background environment, and also to study ways of reducing the data. The results of this study are summarised below;

(i) Dark current. The array dark current was investigated using similar methods to those discussed in section 5.5. Typical saturation times with the array blanked off were 15 minutes. Figure 7.5 shows the variation of initial discharge rate across the array. Pixel #13 has a similar behaviour to #27 of the ROE array and was excluded from the data reduction. The gradual increase seen towards pixel #32 could be due to; (a) a temperature gradient, (b) a capacitance gradient, or (c) a source of illumination, giving a $1/r^2$ intensity fall-off, possibly the output JFET

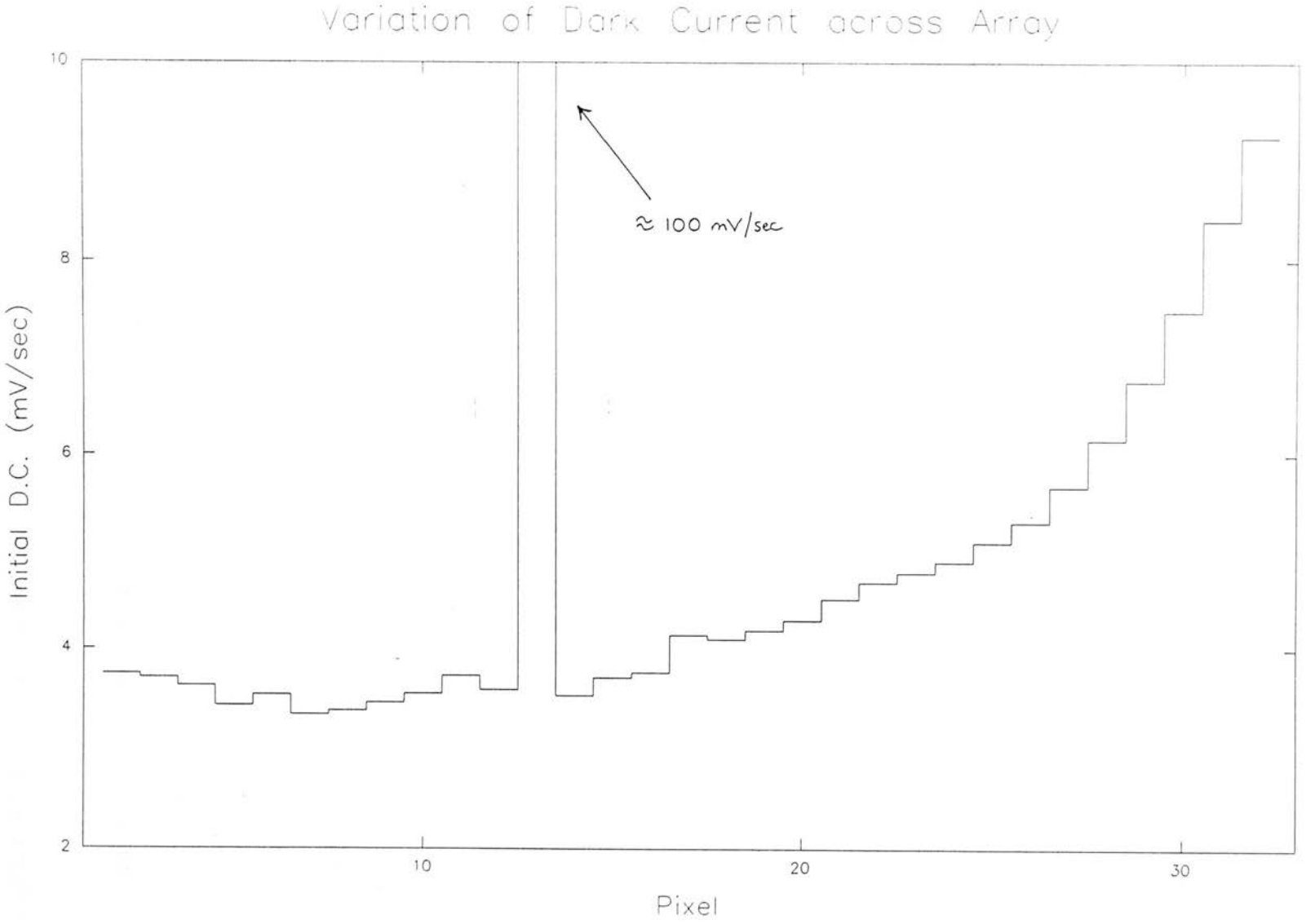

Figure 7.5
Initial 'dark' current discharge across CGAS array (referred to A/D input)

which lies near to this end of the array, and may be slightly warmer due to self-heating.

After studying a selection of pixel I-V responses, it was found that, if the initial discharge above $3.5mVs^{-1}$ (where this figure refers to the A/D input) was attributed to linear photocurrent, then the resultant, dark I-V profiles were very similar in appearance, as would be expected from uniformity considerations (section 5.1.4). Consequently the most likely explanation is illumination.

The initial dark current at the operating bias (-60mV, or a capacity of $5x10^6$ electrons), by comparison with values from the ROE array, was found to be $\approx$1.1fA ($7000els^{-1}$), corresponding to an array temperature, assuming g-r current, of 46+/-2K.

(ii) The readout noise was measured to be around 2500 electrons rms, and as far as could be ascertained, was independent of discharge and integration time. The instrument is therefore presently read-noise limited over the entire dynamic range.

(iii) The photo-response in the absence of dark curent was, as expected, found to be highly linear.

(iv) In the light of the results of section 6.3 concerning the effective detector gain, g′, the H and K sky spectra were studied in order to derive the values of Φ/I_{d0} and discharge, x, leading to an estimate of the spectrum of g′. The white dwarfs observed were faint (K$\approx$12.5-13.5mag.), and therefore gave a raw spectrum very similar to that of the sky. The standard stars were all bright, so that no problem was anticipated with their reduction. The following assumptions were made, in order to derive g′ for the two integration times used;

(a) The I-V response of pixel #15 was taken to be representative of the whole array.

(b) The initial dark discharge rate was assumed to be uniform at $3.5mVs^{-1}$.

(c) The flux, Φ, was obtained using a simple (equal integration time) dark current subtraction from the signal. This is a first order approximation to the true case, but the error in Φ/I_{d0} (estimated to be $\lesssim$25%) is not critical. This is because the aim is to observe the general scale of the g′ variation, and not precisely measure its absolute value.

g′ was calculated at a given x and Φ/I_{d0} by numerical integration of equation 6.5, and the results are shown in figure 7.6.

The derived spectra demonstrate that the gain variation is only significant for the 200 second exposures, and was not as large as initially expected. The reason for this is the presence of the JFET illumination, OH emission at short wavelengths in the H spectrum, and telescope thermal emission at long wavelengths in K, all of which assist in increasing the value of Φ/I_{d0}.

From these results it seems unlikely, under present operating conditions, that the gain variation will pose a serious problem (and will be less so at longer wavelengths for the same resolution), since a large x is associated with a large Φ/I_{d0}, and small x with small Φ/I_{d0}. Large values of g′ (and therefore large variations) are discriminated against (see figure 6.6).

This conclusion, however, is heavily influenced by the assumption of uniform dark current. If this was not the case, it is possible to envisage a situation where large x-small Φ/I_{d0}, and large Φ/I_{d0} values could appear in a spectrum simultaneously, giving a large variation in g′.

(v) From the above results, the data reduction is fairly standard. Adjacent object-sky readouts were differenced (which effectively removes dark current, and electronic offsets), spikes were removed, spectra were normalized (to correct for the fact that the dc level of the spectrum can change due to light-loss fluctuations at the entrance aperture) and coadded, and normal ratioing with 'flat' standards was performed.

The reduced H and K spectra are shown (figure 7.7) for the white

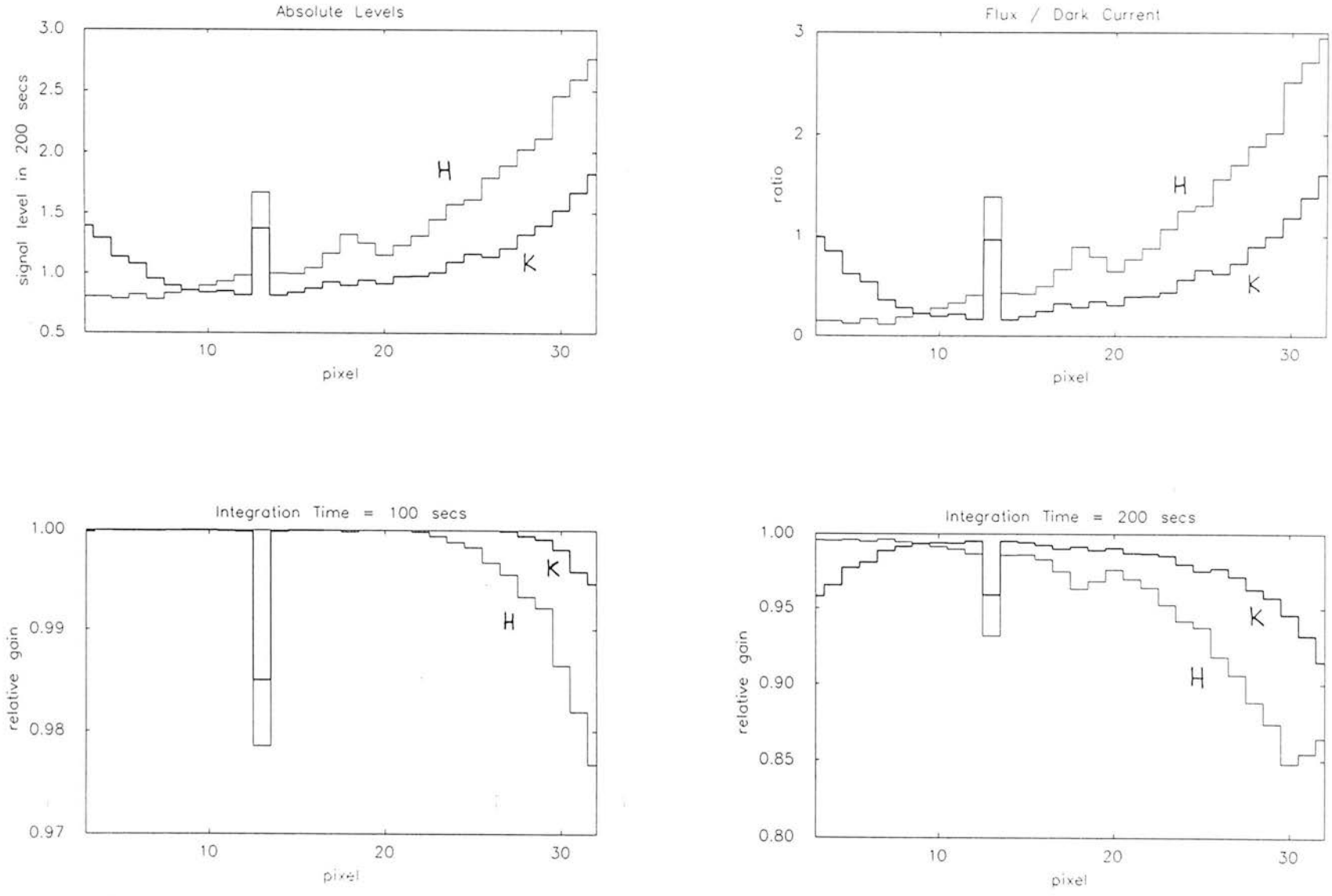

Figure 7.6
Derivation of the effective gain 'spectra' for the 100 and 200 second integrations. Wavelength increases towards pixel #1. The results for pixel #13 are unreliable and should be ignored.

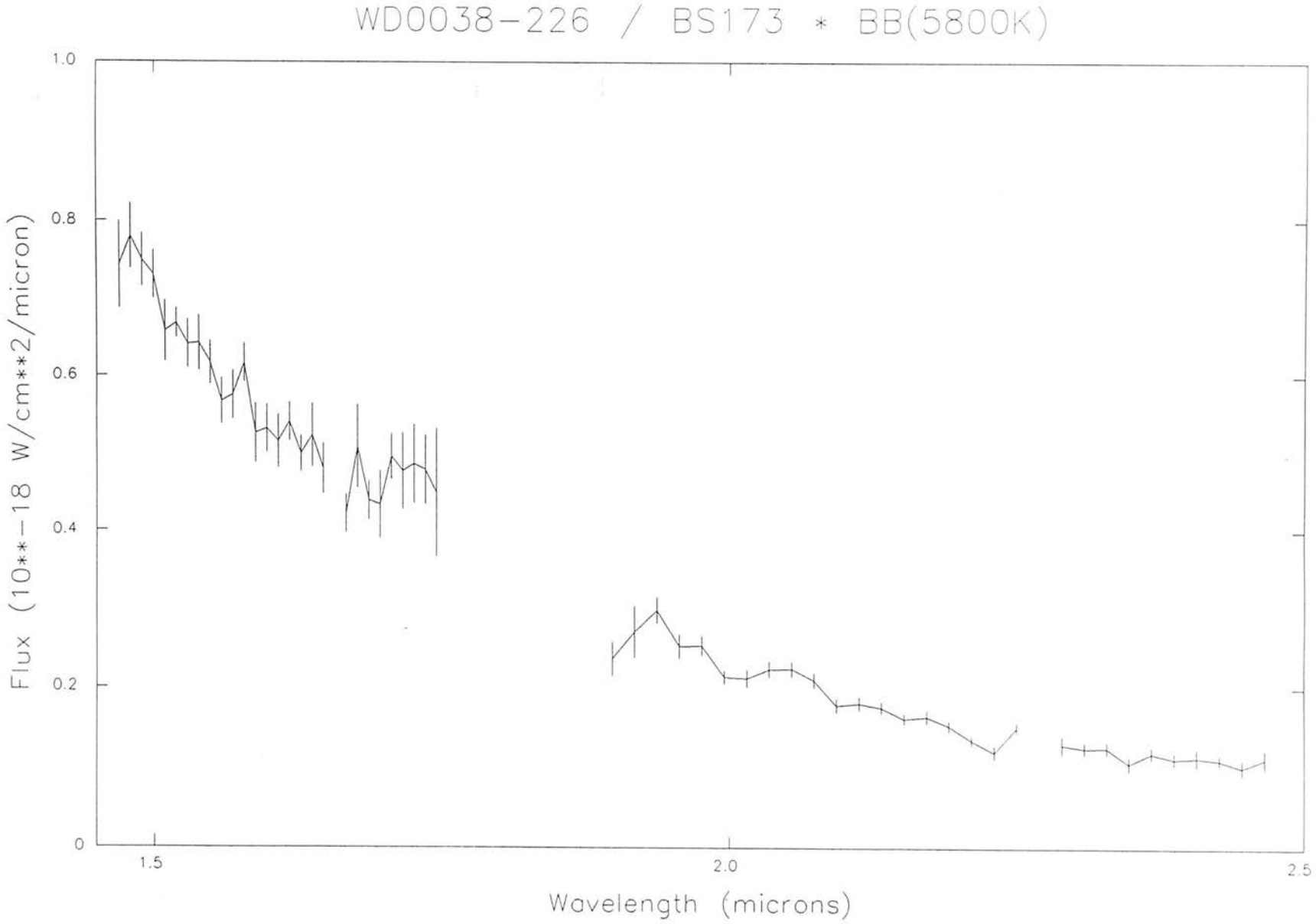
WD0038−226 / BS173 * BB(5800K)
Flux (10**−18 W/cm**2/micron)
1.0
0.8
0.6
0.4
0.2
0
1.5
2.0
2.5
Wavelength (microns)

Figure 7.7

dwarf WD0038-226. The total integration time per point was 80 minutes (derived from 24 object-sky readout pairs per spectrum, and an on-chip integration time of 100 seconds). The S/N ratio of the H spectrum is poorer than that at K, for two reasons; Firstly, $\Delta\lambda$ per pixel is smaller due to higher resolution (2^{nd} order, compared to 1^{st} order at K), and secondly, the grating efficiency for this order and wavelength is lower.

References

Allen, D.A., Jones, T.J. and Hyland, A.R., 1985. Ap.J. 291, 280 'The near-infrared spectrum of Eta Carinae'

Bailey, G.C., 1982. Proc. S.P.I.E. 345, 23 'An integrating 128 element InSb array: recent results'

Bailey, G.C., Niblack, C.A. and Wimmers, J.T., 1986. Proc. S.P.I.E. 686, 76, 'Recent developments on a 128x128 InSb/FET switched hybrid imager for low background applications'

Becklin, E.E. and Neugebauer, G., 1975. Ap.J.Lett. 200, L71, 'High resolution maps of the Galactic Center at 2.2 and 10 microns'

Becklin, E.E., Gatley, I. and Werner, M.W., 1982. Ap.J. 258, 135, 'Far-infrared observations of Sagittarius A. The luminosity and dust density in the central parsec of the Galaxy'

Beckwith, S., Evans II, N.J., Gatley, I., Gull, G. and Russell, R.W., 1983. Ap.J. 264, 152, 'Observations of the extinction and excitation of the molecular hydrogen emission in Orion'

Beynon, J.D.E. and Lamb, D.R., 1980. CCDs and their applications, McGraw-Hill

Blessinger, M.A. and Herring, M., 1984. Proc. S.P.I.E 501, 136 'Results of testing short wavelength HgCdTe hybrid focal plane arrays for Earth remote sensing applications'

Boyd, R.W., 1983. Radiometry and the Detection of Optical Radiation, Wiley-Interscience

Brand, P.W.J.L., Burton, M.G., Geballe, T.R., Moorhouse, A., Bird, M. C. and Wade, R., 1988. submitted to Ap.J.Lett., 'Ratios of molecular hydrogen line intensities in shocked gas: Evidence for cooling flows'

Brown, R.L. and Liszt, H.S., 1984. Ann. Rev. Astron. Astrophys. 22, 223, 'Sagittarius A and its environment'

Connor, F.R., 1973. Noise, Arnold

Davidson, K. and Netzer, H., 1979. Rev. Mod. Phys. 51, 715 'The emission lines of quasars and similar objects'

Davis, R.M. and Niblack, C.A., 1986. Proc. S.P.I.E. 627, 438 'Performance predictions of InSb switched FET hybrid arrays'

Finger, G., Meyer, M. and Moorwood, A.F.M., 1987. Proc. S.P.I.E. 782-18 (in prep.), 'Noise analysis and performance of a self-scanned linear InSb detector array'

Forrest, W.J., Moneti, A., Woodward, C.E., Pipher, J.L. and Hoffman, A., 1985. P.A.S.P. 97, 183, 'The new near infrared array camera at the university of Rochester'

Fowler, A.M. and Britt, J.P., 1982. Proc. S.P.I.E 331, 18 'InSb CID array performance'

Gatley, I., Jones, T.J., Hyland, A.R., Wade, R., Geballe, T.R. and Krisciunas, K., 1986. M.N.R.A.S. 222, 299, 'The spatial distribution and velocity field of the molecular hydrogen line emission from the centre of the Galaxy'

Geballe, T.R., Wade, R., Krisciunas, K., Gatley, I. and Bird, M.C., 1987. Ap.J. 320, 562, 'The broad-line region at the center of the Galaxy'

Genzel, R. and Townes, C.H., 1987. Ann. Rev. Astron. Astrophys. 25, 377, 'Physical conditions, dynamics and mass distribution in the center of the Galaxy'

Goebel, J.H., McKelvey, M.E., McCreight, C.R. and Anderson, G.M., 1986a. Proc. S.P.I.E 627, 418, 'Low background direct readout array performance'

Goebel, J.H. and McCreight, C.R., 1986b. In: The Optimization of the use of CCD Detectors in Astronomy, ESO-OHP Workshop, p261, 'Integrated infrared array technology'

Hoffman, A.W., 1985. SBRC Internal Memorandum, 'Radiometric calibration of SFD circuits'

Hoffman, A.W., 1987. In: Workshop on ground-based Astronomical Observations with Infrared Array Detectors, Hilo, Hawaii, p29, 'Operation and calibration of self-integrating multiplexed arrays'

Hopkins, F.K. and Boyd, J.T., 1984. IR Physics 24, 391 'Dark current analysis of InSb photodiodes'

Hudson, L.R., Tseng, H-F., Wang, W-L. and Weckler, G.P., 1987. Optical Engineering 26, 216, 'Schottky-barrier infrared focal plane arrays for spectroscopic applications'

The Infrared Handbook, eds. Wolf, W.L. and Zissis, G.J., 1978., Office of Naval Research, Department of the Navy

Janesick, J.R., Elliot, T., Collins, S. and Marsh, H., 1984. Proc. S.P.I.E. 501, 2, 'The future scientific CCD'

Joyce, R.R. and Fowler, A.M., 1984. Proc. S.P.I.E. 501, 331 'Further tests of the GE 1x32 InSb CID array at KPNO'

Kopeika, N.S., Hirsh, I. and Hazout, E., 1983. Proc S.P.I.E 430, 183 'Photodiode quantum efficiency improvement through vacuum surface effects'

Kosonocky, W.F. and Elabd, H., 1983. Proc. S.P.I.E. 443, 167 'Schottky-barrier IRCCD focal plane arrays'

Kruse, P.W., 1981. In: Semiconductors and Semimetals; HgCdTe, 18 Chapter 1: 'The emergence of HgCdTe as a modern infrared sensitive material'

Lebofsky, M.J., Montgomery, E.F. and Kailey, W.F., 1985. Proc. 2nd Infrared Detector Technology Workshop (NASA, TM88213), 17-1, 'Evaluation of Rockwell HgCdTe arrays for astronomical use'

McCaughrean, M.J., 1987. PhD Thesis, Edinburgh University, 'The astronomical application of infrared array detectors'

McLean, I.S., Chuter, T.C., McCaughrean, M.J. and Rayner, J.T., 1986. Proc. S.P.I.E. 627, 430, 'System design of a 1-5 micron infrared camera for astronomy'

Mackay, C.D., 1982. Proc. S.P.I.E. 331, 146, 'Drift scan observations with a CCD'

Mackay, C.D., 1986. Ann. Rev. Astron. Astrophys. 24, 255 'CCDs in Astronomy'

Millman, J., 1979. Microelectronics: Digital and Analog Circuits and Systems, McGraw-Hill

Moorwood, A.F.M., 1987. In: Workshop on ground-based Astronomical Observations with Infrared Array Detectors, Hilo, Hawaii, p379, 'IRSPEC: Design, performance and first scientific results'

Orias, G., Hoffman, A.W. and Casselman, M.F., 1986. Proc. S.P.I.E. 627, 408, '58x62 InSb focal plane array for infrared astronomy'

Rieke, G.H. and Lebofsky, M.J., 1985. Ap.J. 288, 618 'The interstellar extinction law from 1 to 13 microns'

Rieke, M.J., Rieke, G.H. and Montgomery, E.F., 1987. In: Workshop on ground based astronomical observations with infrared array detectors, Hilo, Hawaii, p213, 'Rockwell HgCdTe arrays as imagers'

Rouan, D., Lacombe, F., Tiphene, D., Stefanovitch, D., Phan Van, D., Combes, M., Lena, P., Chatard, J.P. and Lussereau, A., 1985. Proc. S.P.I.E. 590, 348, 'Astronomical imaging with a low temperature InSb CID'

Schoolar, R. and Tenescu, E., 1986. Proc. S.P.I.E. 686, 2 'Analysis of InSb photodiode low temperature characteristics'

Sclar, N., 1983. Proc. S.P.I.E 409, 53 'Development status of silicon infrared detectors'

Serabyn, E. and Lacy, J.H., 1985. Ap.J. 293, 445, '[NeII] observations of the Galactic Center: Evidence for a massive Black Hole ?'

Stetson, S.B., Reynolds, D.B., Stapelbroek, M.G. and Stermer, R.L., 1986. Proc. S.P.I.E. 686, 48, 'Design and performance of BIB detector focal plane arrays'

Sze, S.M., 1981. Physics of Semiconductor Devices 2nd ed., Wiley

Tokunaga, A.T., Smith, R.G. and Irwin, E., 1987. In: Workshop on ground based astronomical observations with infrared array detectors, Hilo, Hawaii, p367, 'Use of a 32 element Reticon array for 1-5 micrometer spectroscopy'

Tollestrup, E. and Capps, R.W., 1985. In: Proc. 2nd Infrared Detector Technology Workshop (NASA, TM88213), 21-1, 'A study of Si:In hybrid surface channel IRCCD devices'

Tyson, J.A., 1986. J. Opt. Soc. Am. A. 3, 2131, 'Low light level CCD imaging in astronomy'

Vural, K., Blackwell, J.D., Marin, E.C., Edwall, D.D. and Rode, J.P., 1983. Proc. S.P.I.E. 409, 107, 'Short wavelength infrared hybrid focal plane arrays'

Wade, R., 1983. Proc. S.P.I.E. 445, 47, 'A 1-5 micron cooled grating array spectrometer and Fabry-Perot system for UKIRT'

Wade, R., Geballe, T.R., Kriscuinas, K., Gatley, I. and Bird, M.C., 1987. Ap.J. 320, 570, 'The ionization state in, and reddening to, the center of the Galaxy'

Weedman, D.W., 1977. Ann. Rev. Astron. Astrophys. 15, 69 'Seyfert galaxies'

White, M.H., Lampe, D.R., Blaha, F.C. and Mack, I.A., 1974. I.E.E.E. Journal of solid-state circuits SC-9, 1, 'Characterization of surface channel CCD image arrays at low light levels'

Wimmers, J.T. and Smith, D.S., 1982. Proc. S.P.I.E. 364, 123 'Characteristics of InSb photovoltaic detectors at 77K and below'

Wolf, J. and Lemke, D., 1985. IR Physics 25, 327 'Status of doped infrared detectors for low background astronomical applications'

Yang, E.S., 1978. Fundamentals of Semiconductor Devices, McGraw-Hill

Abbreviations

A/D	Analog-to-Digital
BB	Black Body
BLIP	Background Limited Infrared Performance
C_e	Conversion Factor (electrons per data number)
CCD	Charge-Coupled Device
CDS	Correlated Double Sampling
CE	Cincinnati Electronics Corporation
CGAS	Cooled Grating Array Spectrometer
CGS2,CGS4	Cooled Grating Spectrometer (Nos. 2 and 4)
CTE	Charge Transfer Efficiency
dc	Dark Current (when used as a subscript)
DMA	Direct Memory Access
dn	Data Number
DRO	Direct Read-Out
EOS	End of Scan
FOV	Field of View
H	High (gain)
IRSPEC	Infrared Spectrometer
JFET	Junction Field-Effect Transistor
L	Low (gain)
LHe	Liquid Helium
LN_2	Liquid Nitrogen
NEP	Noise Equivalent Power
PV	Photovoltaic
qe	Quantum Efficiency
R	Wavelength Resolution ($\lambda/d\lambda$)
ROE	Royal Observatory, Edinburgh
S/N	Signal-to-Noise (ratio)
SBRC	Santa Barbara Research Corporation
SFD	Source-Follower per Detector
t_i	Integration Time
UKIRT	United Kingdom Infrared Telescope
VL	Very Low (gain)
VTE	Voltage Transfer Efficiency
Φ/I_{d0}	Ratio of Photocurrent to Dark Current